139
97

STUDIES ON SECONDARY INSTABILITIES

by

German R. Santos

Dissertation submitted to the Faculty of the

Virginia Polytechnic Institute and State University

in partial fulfillment of the requirements for the degree of

Doctor of Philosophy

in

Engineering Mechanics

APPROVED:

Th. Herbert, Chairman

D.T. Mook

D.P. Telionis

S.A. Ragab

M. Renardy

November, 1987

Blacksburg, Virginia

STUDIES ON SECONDARY INSTABILITIES

by

German R. Santos

Committee Chairman: Thorwald Herbert

Engineering Science and Mechanics

(ABSTRACT)

Significant advances in understanding early stages of transitional flows have been achieved by studying secondary instabilities in selected prototype flows. These secondary instabilities can be modeled as parametric instabilities of the nearly periodic flow that consists of the prototype velocity profile and a superposed finite-amplitude TS-wave (wavelength λ). The generally three-dimensional secondary instabilities are governed by a linearized system of partial differential equations with periodic coefficients which are reduced to an algebraic eigenvalue problem through the application of a spectral collocation method.

Following Floquet theory, previous analysis looked for subharmonic (wavelength 2λ) and fundamental (wavelength λ) types of solutions. We extend the Floquet theory to solutions having arbitrary wavelengths, hence including the previous solutions as special cases. Modes with wavelength in between the subharmonic and fundamental values are called detuned modes. Detuned modes lead to combination resonance which has been observed in controlled transition experiments. Knowledge of the bandwidth of amplified detuned or (combination) modes is very important for clarification of the selectivity of the early stages of transition with respect to initial disturbances.

We have selected two flows: the Blasius boundary layer flow and the hyperbolic-tangent free-shear flow as prototypes of wall bounded flows and unbounded flows, respectively. In the Blasius flow we have concentrated on studying detuned modes. We found the growth rates of modes slightly detuned from the subharmonic wavelength to be almost as large as the growth rate of the subharmonic itself. This result is consistent with both the broad-band spectra centered at subharmonic frequency observed in the "biased" experiment of Kachanov & Levchenko, wherein only the TS frequency was introduced, and with the large band-width of resonance in the "controlled" experiments, wherein a TS wave and the detuned modes were introduced simultaneously.

In the free-shear flow, our goals were three-fold. The first was to investigate whether the Floquet analysis based on the shape assumption for TS waves would provide results consistent with results for the stability of Stuart vortices. Second, we aimed at revealing the effect of viscosity on these results. Finally, we wanted to evaluate a group of spectral methods for the numerical treatment of the flow in an unbounded domain. We have made a detailed analysis of subharmonic, fundamental, and detuned modes. Results display the basically inviscid, convective character of the secondary instabilities, and their broadband nature in the streamwise and spanwise directions. In the inviscid limit, and for neutral TS waves, a detailed comparison is made with the closely related study on stability of Stuart vortices by Pierrehumbert & Widnall. Good quantitative agreement is obtained. For a wide range of Reynolds numbers and amplitudes of the 2-D primary wave, results reveal that the most unstable subharmonic modes are two-dimensional (vortex pairing). On the other hand, the most unstable fundamental modes are three-dimensional,

with short spanwise wavelengths. Detuned modes have characteristics in between, being most unstable in the two-dimensional or three-dimensional form depending on the detuning value.

Comparisons of our results for a superposed TS wave of constant amplitude with results obtained by numerical simulations suggested that the growth of the TS wave may have a significant effect on the secondary disturbance growth. To check this hypothesis, we have developed a numerical method that accounts for small variations in the TS amplitude. However, the results indicate that the discrepancies are due to other yet concealed effects.

ACKNOWLEDGMENTS

The first acknowledgment must go to my adviser Dr. Th. Herbert for his invaluable guidance, assistance and support in my research throughout the years. I would also like to acknowledge Dr. D.T Mook for his friendship and advice. I am indebted to him and the other members of my committee, Dr. Telionis, Dr. Ragab and Dr. Renardy for their availability and helpful comments.

A special note of thanks is due to Dr. C. Thompson who assisted me with computers and to Dr. W. Saric who introduced me to experimental transition research. I would also like to thank C. Hawley for her assistance in computers and my writing and style.

I benefited enormously from many enlightening discussions with fellow researchers Dr. R. Li, F. Bertolotti, and J. Crouch. I am particularly indebted to the people of the Escuela Colombiana de Ingenieria for their continuous support.

I enjoyed the friendship of the Latin American community in Blacksburg. The infinite patience and encouragement of my fiancee Consuelo and my parents are most deeply appreciated.

This work was supported by the National Science Foundation under Contract MEA-8120935, the Office of Naval Research under Contract N00014-84-K-0093, and by the Air Force Office of Scientific Research under Contracts F49620-84-K-0002 and F49620-87-K-0005.

TABLE OF CONTENTS

1. INTRODUCTION

A good mathematical description of turbulence has been searched without success for a long time and would be a fundamental breakthrough. Its inherent nonlinear characteristics have impeded us from gaining key insight into the onset of turbulence. However, the recent massive interest in nonlinear phenomena shared by many disciplines has provided both new insights and new tools in the study of flow transition to turbulence. Such is the case, for example, with the recently discovered "universal" features of some elementary chaotic phenomena. In addition, extraordinary advances in computers and computational methods have created a new branch of mathematics that allows to obtain quickly a rich variety of results and to investigate new phenomena.

According to the current concepts of bifurcation theory, a hierarchy of qualitatively different elementary fluid motions exists. Furthermore, one elementary motion can give rise to another elementary motion due to instabilities with respect to some class of disturbances. The cycle could be repeated, forming a cascade of instabilities. Typically, the initial flow is selected from the archive of known solutions of the equations of motion. Instabilities with respect to small disturbances of this basic flow (primary instability) can be analyzed by the classical linear stability theory arriving, for example, at the Orr-Sommerfeld equation for parallel flows. A nonlinear evolution process then creates new kinds of motions. The evolution is usually modeled by some form of the Landau equation (Stuart 1960, Watson 1960). Eventually, this new elementary flow experiences new (secondary) instabilities. This solution is generally characterized by a different length (or time) scale. This cycle is repeated until the flow eventually becomes fully turbulent. This process will lead to a chaotic type of behavior (turbulence ?) after a relatively few cycles

(Ruelle & Takens 1971), infinitely many period-doubling bifurcations (Feigenbaum 1980), or intermittently (Manneville & Pomeau 1980). The route selected depends on the specific features of the flow.

To test the mentioned hypothesis, experimental and analytical analyses are usually done on very simplified flows. It is assumed that these flows. although simple, contain the rather complex features of transition in real flows. In this paper, we consider the prototypes of boundary layers and parallel mixing layers described by the Blasius and the hyperbolic-tangent velocity profiles, respectively. The hyperbolic tangent profile is particularly attractive because it closely resembles the shear layer that forms in separated flows. The hyperbolic-tangent profile is also a model frequently used in studies of combustors, chemical processes, and jet noise.

Laboratory experiments and direct numerical simulations indicate that once transition begins boundary and mixing layers become quickly turbulent. This is a characteristic of flows following a route to transition which leads to turbulence through only a few bifurcations. Therefore, the essential features of the transition process for these types of flows are probably contained in their early stages: linear primary instability, nonlinear evolution, and linear secondary instability. Our present goal is to analyze the secondary instabilities. Hopefully, with this study, we will gain further insight into the mechanisms of the transition process.

The approach followed here is based on the Floquet analysis of the periodic basic flow consisting of the mean flow and a finite amplitude instability wave. The theory was developed by Herbert (1981 - 1987) and has been remarkably successful in calculating secondary instabilities in channel flows and boundary-layer flows. The theory is based on experimental and

computational evidence for the existence of an almost equilibrium finite-amplitude wave. The periodic modulation of the steady laminar shear flow which is produced leads to a parametric excitation of new classes of disturbances that are in general three-dimensional for boundary layers and two-dimensional for mixing layers. The resultant modes of instability, as in the primary case, can grow in space and time. Furthermore, the modes can be classified as fundamental, subharmonic, or combination resonance modes, according to the ratio of their streamwise wavelength to the TS wavelength. Fundamental (peak-valley splitting) and subharmonic modes have been widely studied (Herbert 1982, Bertolotti 1985). We have extended the analysis to include the more general class of combination-resonance modes.

Floquet analysis of secondary instabilities has already been applied by Kelly (1967) to mixing layers. He was able to explain the parametric nature of the subharmonic paring mode experimentally discovered by Sato (1956). More recently, Pierrehumbert & Widnall (1982) performed a linear stability analysis of Stuart's vortices with respect to three-dimensional disturbances. Stuart vortices are an exact solution of the two-dimensional Euler equations (Stuart 1967). Pierrehumbert & Widnall confirmed that the most unstable subharmonic mode is two-dimensional (vortex-pairing) and found that the fundamental mode is inherently three-dimensional (translative instability).

Stuart's vortices can be approximated accurately by the superposition of the hyperbolic-tangent profile and a neutral eigenfunction of the Rayleigh equation, the inviscid counterpart of the Orr-Sommerfeld equation. TS waves are actually a first-order approximation to the solution of Euler's equations of motion. Therefore, we relate the Stuart vortices to the flow produced by nonlinear equilibrium of the primary instabilities of the $\tanh y$ profile.

Accordingly, Pierrehumbert & Widnall's results correspond to the secondary instability stage in the cascade of instabilities. Because their analysis is closely related to ours, we dedicate much of our efforts to detailed comparisons. In addition, we extend the analysis to modes of combination resonance that arise as the most general class of solutions in the Floquet analysis. Moreover, we study the effect of the viscosity on the growth rates and investigate the accuracy of results obtained with different numerical methods.

2. GOVERNING EQUATIONS

2.1 Basic Equations

The flow is assumed to be incompressible and viscous, and is governed by the Navier-Stokes equations

$$\nabla \cdot \mathbf{v} = 0 \tag{2-1}$$

$$\frac{\partial \mathbf{v}}{\partial t} + (\mathbf{v} \cdot \nabla)\mathbf{v} = -\nabla p + \frac{1}{Re}\nabla^2 \mathbf{v}. \tag{2-2}$$

The velocity $\mathbf{v}(x',y,z,t) = (u,v,w)$ and the presure $p(x',y,z,t)$ have been non-dimensionalized in terms of a typical velocity of the free stream U_0 and a typical length scale L. Re is the Reynolds number based on the above velocity and length scales and on the kinematic viscosity ν. The variables x',y and z are the non-dimensional coordinates in the streamwise, normal, and spanwise directions, respectively, and t is the dimensionless time.

The boundary conditions require that all velocity components vanish at solid boundaries or match free stream velocities. The specific details depend on the flow analyzed, like channel flow, boundary layers, or mixing layers.

To eliminate the pressure, we write equations (2-1) and (2-2) in form of the vorticity transport equation

$$\frac{1}{Re}\nabla^2 \omega - \frac{\partial \omega}{\partial t} - (\mathbf{v} \cdot \nabla)\omega + (\omega \cdot \nabla)\mathbf{v} = 0, \tag{2-3}$$

where the components of the vorticity $\omega = \nabla \times \mathbf{v}$ are $\omega = (\xi,\eta,\varsigma)$.

It is convenient to express the basic equations in coordinates moving in the direction x' with the velocity c_r (Galilean frame).

$$x = x' - c_r t. \tag{2-4}$$

In Cartesian coordinates x, y, z, the continuity equation is

$$\frac{\partial u}{\partial x} + \frac{\partial v}{\partial y} + \frac{\partial w}{\partial z} = 0. \tag{2-5}$$

Using continuity and applying $\frac{\partial}{\partial z}$ to the η-vorticity equation, we obtain

$$(\frac{1}{Re}\nabla^2 - \frac{\partial}{\partial t} - c_r \frac{\partial}{\partial x})\frac{\partial \eta}{\partial z} - \frac{\partial}{\partial z}(\mathbf{v}\cdot\nabla)\eta + \frac{\partial}{\partial z}(\omega\cdot\nabla)v = 0. \tag{2-6}$$

Similarly, applying $\frac{\partial}{\partial x}$ to the ς-vorticity equation, and subtracting $\frac{\partial}{\partial x}$ of the ξ-vorticity equation, we obtain

$$(\frac{1}{Re}\nabla^2 - \frac{\partial}{\partial t} - c_r \frac{\partial}{\partial x})\nabla^2 v - \frac{\partial}{\partial x}(\mathbf{v}\cdot\nabla)\varsigma + \frac{\partial}{\partial x}(\omega\cdot\nabla)w$$

$$+ \frac{\partial}{\partial z}(\mathbf{v}\cdot\nabla)\xi - \frac{\partial}{\partial z}(\omega\cdot\nabla)u = 0. \tag{2-7}$$

Equations (2-6) and (2-7) are closely related to Squire's equation and Orr-Sommerfeld equation, respectively, which can be easily obtained by substituting normal modes.

2.2 Decomposition of the Velocity Field

We consider a parallel shear flow $\mathbf{V}, P$, and study its stability by superposing disturbances $\hat{\mathbf{v}}, \hat{p}$. The total velocity and pressure fields are separated by writing

$$\mathbf{v} = \mathbf{V} + \hat{\mathbf{v}}, \quad p = P + \hat{p}. \tag{2-8}$$

$\mathbf{V}(y) = (U, 0, 0)$, $P(x, y)$ is a steady solution of the Navier-Stokes equations, like the Plane Poiseuille flow or the hyperbolic tangent velocity profile. The former is a well known exact solution, while for finite Re, the latter is only an approximation. However, in the presence of an artificial body force counteracting the viscous effects, the $\tanh(y)$ profile is also an exact solution

of the Navier-Stokes equations (Huerre 1980).

Introducing the operator

$$L = \frac{1}{Re}\left(\frac{\partial^2}{\partial y^2} + \frac{\partial^2}{\partial x^2} + \frac{\partial^2}{\partial z^2}\right) - \frac{\partial}{\partial t} - (U - c)\frac{\partial}{\partial x}, \tag{2-9}$$

and substituting (2-9) into equations (2-6), (2-7), leads to

$$\frac{\partial \hat{u}}{\partial x} + \frac{\partial \hat{v}}{\partial y} + \frac{\partial \hat{w}}{\partial z} = 0, \tag{2-10}$$

$$L\hat{u} - U'\hat{v} - \frac{\partial \hat{p}}{\partial x} - (\hat{\mathbf{v}}\cdot\nabla)\hat{u} = 0, \tag{2-11}$$

$$L\frac{\partial \hat{\eta}}{\partial z} - U'\frac{\partial^2 \hat{v}}{\partial z^2} - \frac{\partial}{\partial z}(\hat{\mathbf{v}}\cdot\nabla)\hat{\eta} + \frac{\partial}{\partial z}(\hat{\omega}\cdot\nabla)\hat{v} = 0, \tag{2-12}$$

$$L\nabla^2\hat{v} + U''\frac{\partial \hat{v}}{\partial x} - \frac{\partial}{\partial x}(\hat{\mathbf{v}}\cdot\nabla)\hat{\zeta} + \frac{\partial}{\partial x}(\hat{\omega}\cdot\nabla)\hat{w} \tag{2-13}$$

$$+ \frac{\partial}{\partial z}(\hat{\mathbf{v}}\cdot\nabla)\hat{\xi} - \frac{\partial}{\partial z}(\hat{\omega}\cdot\nabla)\hat{u} = 0.$$

Equations (2-10) - (2-13) are equivalent to the Navier-Stokes equations for describing finite-amplitude deviations from the steady laminar flow.

2.3 First Stage: Primary Instability

In the first stage of the cascade of instabilities, the steady parallel flow that constitutes the elementary motion undergoes the first structural change. Infinitesimal disturbances destabilize the parallel flow, creating a new motion that can be analyzed by classic linear instability analysis. We will discuss briefly this analysis.

The most amplified infinitesimal disturbances are two dimensional (Squires theorem). Accordingly, we will consider small two-dimensional

perturbations $\mathbf{v}_1$ which is equivalent to assuming disturbances $\hat{\mathbf{v}}$ of the form

$$\hat{\mathbf{v}}(x,y,z,t) = A\,\mathbf{v}_1(x,y,t), \tag{2-14}$$

where the small parameter A represents the rms amplitude measured in experiments

For convenience we introduce the streamfunction ψ_1, that is related to the velocity $\mathbf{v}_1 = (u_1, v_1, 0)$ and vorticity $(0, 0, \varsigma_1)$ by

$$u_1 = \frac{\partial \psi_1}{\partial y}, \quad v_1 = -\frac{\partial \psi_1}{\partial x}, \quad \varsigma_1 = -\nabla^2 \psi. \tag{2-15}$$

The streamfunction is also separated in mean and fluctuating parts by writing

$$\psi(x,y,t) = \psi_0(y) + A\,\psi_1(x,y,t). \tag{2-16}$$

Substitution of (2-14) into the vorticity equation (2-3) leads to the nonlinear partial differential equation

$$\frac{1}{Re}\nabla^2(\nabla^2\psi_1) - \frac{\partial}{\partial t}\nabla^2\psi_1 - U\frac{\partial}{\partial x}\nabla^2\psi_1 + \frac{d^2U}{dy^2}\frac{\partial \psi_1}{\partial x}$$

$$= A\left\{\frac{\partial \psi_1}{\partial y}\frac{\partial}{\partial x} - \frac{\partial \psi_1}{\partial x}\frac{\partial}{\partial y}\right\}\nabla^2\psi_1. \tag{2-17}$$

In the classical approach, the equation (2-17) is then linearized. The normal mode concept can be applied, and we can seek solutions of the form $\psi_1(x,y,t) = \phi(y)e^{i\alpha(x-ct)}$ where c and α are in general complex. By substituting for ϕ , we obtain the Orr-Sommerfeld stability equation

$$\left\{\frac{1}{Re}D^2 - i\alpha[(U - c)D^2 - U'']\right\}\phi = 0, \tag{2-18}$$

where

$$D^2 = \frac{d^2}{dy^2} - \alpha^2, \quad U'' = \frac{d^2U}{dy^2}. \tag{2-19}$$

If homogeneous boundary conditions are considered, equation (2-18) leads to an eigenvalue problem of the form $F\ (\alpha, c, Re\ ) = 0$. At this point, there are two ways to proceed. In the temporal stability problem, one considers disturbances that grow in time and solves for the complex eigenvalue c . The parameters α and Re are real. Alternatively, in the spatial stability problem, one considers growth in space and solves for complex α. Further discussion of the two concepts is found in section (2.5.3).

The spectrum of eigenvalues for bounded flow, like Poiseuille flow, is purely discrete (Lin 1961). For unbounded flows such as boundary layers, the spectrum consists of a finite number of discrete eigenvalues and a continuous spectrum. The stability characteristics are given mainly by the most unstable (principal) eigenvalue. However, the interaction among the various modes (both discrete and continuous) is also of considerable importance from the physical and numerical points of view.

2.4 Nonlinear Evolution : Formation of the Periodic Flow

The two-dimensional flow described in the preceding section does not grow indefinitely in the exponential way assumed by the linear theory. Nonlinear mechanisms affect fundamentally this linear behavior. Experimental and numerical evidences indicate that the nonlinear evolution of unstable primary disturbances create a two-dimensional nearly periodic flow. For the plane channel flow, it is known that strictly periodic stable or unstable equilibrium motions exist. These equilibrium states of constant amplitude allow a mathematically clean formulation of the secondary instability theory.

The disturbance is considered in the form of a wave periodic in t and x' with wavelength $\lambda_x = 2\pi/\alpha$ and phase velocity c_r. The disturbance velocity $\mathbf{v}_1$ is steady and streamwise periodic in the Galilean frame,

$$\mathbf{v}_1(x',y,t) = \mathbf{v}_1(x,y) = \mathbf{v}_1(x+\lambda_x,y). \tag{2-20}$$

The nonlinear partial differential equation (2-17) reduces in the Galilean frame to

$$\left[\frac{1}{Re}\nabla^2 - (U - c_r)\frac{\partial}{\partial x}\right]\nabla^2\psi_1 - U''\frac{\partial\psi_1}{\partial x}$$

$$= A\left\{\frac{\partial\psi_1}{\partial y}\frac{\partial}{\partial x} - \frac{\partial\psi_1}{\partial x}\frac{\partial}{\partial y}\right\}\nabla^2\psi_1. \tag{2-21}$$

The periodicity of the streamfunction allows us to expand the solution of (2-21) in the Fourier series

$$\psi_1(x,y) = \sum_{l=-\infty}^{\infty} \phi_l(y)\, e^{il\alpha x}, \tag{2-22}$$

where $\phi_{-l} = \phi_l^{\dagger}$ is necessary for a real solution and $\dagger$ denotes the complex conjugate. Substitution of the series (2-22) into (2-21) yields the infinite system of coupled ordinary differential equations

$$\left\{\frac{1}{Re}D_l^2 - il\alpha(U - c_r)D_l - U''\right]\phi_l$$

$$= \sum_{m=0}^{l} P_{m,l-m} + \sum_{m=1}^{\infty}(P_{-m,l+m} + P_{l+m,-m}), \tag{2-23}$$

where

$$P_{l,m} = -i\alpha\{\phi_m' l D_l\phi_l - m\phi_m D_l\phi_l'\} \tag{2-24}$$

and $D_l = d^2/dy^2 - l^2\alpha^2$ and the prime denotes d/dy.

Accurate approximation to the equilibrium solutions can be obtained numerically by solving a truncated finite system. At the present time, solutions of equation (2-23) have been found only for certain elementary flows like Poiseuille flow. For flows like the Blasius flow, equilibrium states have not been found.

Herbert (1982) has developed an alternative way to construct the periodic basic flow based on the classical shape and parallel flow assumptions. With the shape assumption, the nonlinear disturbance is assumed to have the same spatial structure as the linear one. The shape assumption is equivalent to neglecting higher harmonics and the mean flow distortion and to considering the amplitude of the TS wave A as a parameter. Hama (personal communication) has found that this nonlinear distortion in boundary layers is weak even for u' amplitudes as high as 10%. Consequently, the nonliner terms of (2-23) are discarded. This assumption is also justified by "observations that the secondary instability occurs at small amplitudes and originates from the redistribution of vorticity, not from the amplitude-sensitive Reynolds stresses." (Herbert 1984). Accordingly, the streamfunction is given by

$$\psi(x,y) = \phi_1(y)e^{i\alpha x} + \phi_1^{\dagger}(y)e^{-i\alpha x} \qquad (2\text{-}25)$$

where ϕ_1 is the principal mode of the Orr-Sommerfeld equation.

The generalized parallel flow approximation includes the assumptions of the locally parallel flow $\mathbf{v}_0$ and the locally constant amplitude A. The first assumption is well established in the primary instability theory. The second one is equivalent to assuming slower streamwise variation of the amplitude A in comparison with the secondary instability amplitudes B. This assumption is, therefore, justified for sufficiently large growth rates of the secondary

instability disturbances.

2.5 Second Stage: Secondary Instability

2.5.1 Formulation

In the next stage in the analysis of the cascade of instabilities, we consider the stability characteristics of the almost periodic flow with respect to three-dimensional disturbances.

In other words, we consider disturbances $\hat{\mathbf{v}}$ of the form:

$$\hat{\mathbf{v}} = \mathbf{v}_2(x,y,t) + B\ \mathbf{v}_3(x,y,z,t), \tag{2-26}$$

$$\hat{p} = p_2(x,y,t) + B\ p_3(x,y,z,t), \tag{2-27}$$

where $\mathbf{v}_2$ and p_2 represent the two dimensional periodic flow discussed in the preceding section. Again, $\hat{\mathbf{v}}$ satisfies the vorticity equations (2-10) to (2-13).

In standard fashion, we substitute (2-26) and (2-27) into the vorticity equations, neglect terms of $O(B^2)$, and use the continuity equation to eliminate the spanwise disturbance w_3 to obtain

$$\begin{aligned}
&[\frac{1}{Re}\nabla^2 - (U - c_r)\frac{\partial}{\partial x} - \frac{\partial}{\partial t}]\frac{\partial \eta_3}{\partial z} - U'\frac{\partial^2 v_3}{\partial z^2} \\
&+ A\{(-\frac{\partial \psi}{\partial y}\frac{\partial}{\partial x} + \frac{\partial \psi}{\partial x}\frac{\partial}{\partial y} - \frac{\partial^2 \psi}{\partial x\,\partial y})\frac{\partial \eta_3}{\partial z} \\
&+ \frac{\partial^2 \psi}{\partial x^2}(\frac{\partial^2 u_3}{\partial x\,\partial y} + \frac{\partial^2 v_3}{\partial y^2}) - \frac{\partial^2 \psi}{\partial y^2}\frac{\partial^2 v_3}{\partial z^2}\} = 0,
\end{aligned} \tag{2-28}$$

$$\begin{aligned}
&[\frac{1}{Re}\nabla^2 - (U - c_r)\frac{\partial}{\partial x} - \frac{\partial}{\partial t}]\nabla^2 v_3 - U''\frac{\partial v_3}{\partial x} \\
&+ A\{(-\frac{\partial \psi}{\partial y}\frac{\partial}{\partial x} + \frac{\partial \psi_1}{\partial x}\frac{\partial}{\partial y})\nabla^2 v_3
\end{aligned}$$

$$+\frac{\partial^2\psi_1}{\partial x^2}\left(\frac{\partial\varsigma_3}{\partial y}+\frac{\partial\eta_3}{\partial z}\right)-\frac{\partial^2\psi_1}{\partial x\,\partial y}\left(\frac{\partial\varsigma_3}{\partial x}+\frac{\partial\xi_3}{\partial z}\right)-\frac{\partial\varsigma_1}{\partial x}\left(2\frac{\partial u_3}{\partial x}+\frac{\partial v_3}{\partial y}\right)$$

$$-\frac{\partial\varsigma_1}{\partial y}\frac{\partial v_3}{\partial x}$$

$$-\left(u_3\frac{\partial}{\partial x}+v_3\frac{\partial}{\partial y}\right)\frac{\partial\varsigma_1}{\partial x}\Big\}=0, \tag{2-29}$$

where the vorticity components η_3 and ξ_3 can be expressed in terms of u_3 and v_3.

The resulting system of equations is linear in u_3 and v_3 with coefficients independent of z and t. Therefore, we can use normal modes in the spanwise variable and in time. In addition, the system is periodic in the streamwise variable so that we can base the x-dependence on the Floquet theory for periodic ordinary differential equations. Consequently, we seek solutions of the form

$$\mathbf{v}_3(x,y,z,t)=e^{\sigma t}e^{i\beta z}e^{\gamma x}\tilde{\mathbf{V}}(x,y). \tag{2-30}$$

The normal mode concept provides the exponential dependence in the spanwise direction (wavenumber $\beta=2\pi/\lambda_z$) and in time ($\sigma=(\sigma_r,\sigma_i)$). Floquet theory suggests the exponential function with characteristic exponent $\gamma=(\gamma_r,\gamma_i)$ and the x-periodic function $\tilde{\mathbf{V}}$ with wavelength λ_x.

The x-periodic function $\tilde{\mathbf{V}}$ can be further expanded in terms of a Fourier series. Hence, we can write the velocity field of the disturbances $\mathbf{v}_3$ in the form

$$\mathbf{v}_3(x,y,z,t)=e^{\sigma t}e^{i\beta z}e^{\gamma x}\sum_{n=-\infty}^{\infty}\hat{\mathbf{v}}_n(y)e^{in\alpha x}. \tag{2-31}$$

Without loss of generality and to clarify some properties of the system, let

$$\gamma_i = \epsilon\,\hat{\alpha}, \quad \hat{\alpha} = \alpha / 2. \tag{2-32}$$

Then, (2-31) can be written as

$$v_3(x,y,z,t) = e^{\sigma t}\, e^{i\beta z}\, e^{\gamma_r z}\, e^{i\epsilon\hat{\alpha}x} \sum_{n=-\infty}^{\infty} \hat{v}_n(y)\, e^{2in\hat{\alpha}x}. \tag{2-33}$$

Note that it is sufficient to consider $-1<\epsilon<1$. Forms of the solution (2-33) using ϵ outside [-1,1] can be expressed alternatively inside [-1,1] by renumbering the Fourier series.

The form of solution presented above includes all the routes to transition observed experimentally as we will discuss shortly. The peak-valley splitting, the staggered pattern, and the combination resonance are all described by equation (2-33) . The imaginary part of γ interacts with the periodic velocity field $\tilde{V}$ producing a variety of responses in the boundary layer.

Substitution of (2-33) into (2-29) yields the following infinite system of ordinary differential equations that govern the Fourier functions $\hat{v}_n(y)$

$$L_n(u_n) + M_n(v_n) + A \sum_{l=-\infty}^{\infty} [N_{l,n-l}(u_n) + P_{l,n-l}(v_n)] = 0, \tag{2-34}$$

$$Q_n(v_n) + A \sum_{l=-\infty}^{\infty} [R_{l,n-l}(u_n) + S_{l,n-l}(v_n)] = 0; \tag{2-35}$$

where the w_n component is given by :

$$w_n = \frac{i}{\beta}[(v_n)' + (\gamma_r + i(2n+\epsilon)\hat{\alpha})u_n], \tag{2-36}$$

and the operators L_n , M_n , $N_{l,m}$, P_n , Q_n , $R_{l,m}$, $S_{l,m}$ are defined as follows

$$L_n = [\frac{1}{Re}D_n - (\gamma_r + i(2n+\epsilon)\hat{\alpha})(U - c_r) - \sigma\ ]\ k_n, \tag{2-37}$$

$$M_n = -\left[\frac{1}{Re}D_n - (\gamma_r + i(2n+\epsilon)\hat{\alpha})(U - c_r) - \sigma\right]$$

$$(\gamma_r + i(2n+\epsilon)\hat{\alpha})\frac{d}{dy} - \beta^2 U', \tag{2-38}$$

$$N_{l,m} = -\phi_l'[k_m(\gamma_r + i(2n+\epsilon)\hat{\alpha})]$$

$$+ \phi_l\, l\alpha(\beta^2 + (2m+\epsilon)\hat{\alpha} - i\gamma_r(\gamma_r + i(2n+\epsilon)\hat{\alpha}))\frac{d}{dy}, \tag{2-39}$$

$$P_{l,m} = -\phi_l''\beta^2 + \phi_l'(2m+\epsilon)\hat{\alpha} - i\gamma_r(\gamma_r + i(2n+\epsilon)\hat{\alpha})\frac{d}{dy}$$

$$- \phi_l[l\alpha(\gamma_r + i(2n+\epsilon)\hat{\alpha})]\frac{d^2}{dy^2}, \tag{2-40}$$

$$Q_n = [\frac{1}{Re}D_n - (\gamma_r + i(2n+\epsilon)\hat{\alpha})(U - c_r) - \sigma\ ]D_n$$

$$+ U''(\gamma_r + i(2n+\epsilon)\hat{\alpha}), \tag{2-41}$$

$$R_{n,m} = \phi_l\, l^2\alpha^2 k_m + \phi_l''[-l\alpha(l\alpha + 2(2m+\epsilon)\hat{\alpha} - i\gamma_r)]$$

$$- \phi_l'[2l\alpha(2m+\epsilon)\hat{\alpha} - i\gamma_r]\frac{d}{dy} + \phi_l(l\alpha)^2\frac{d^2}{dy^2}, \tag{2-42}$$

$$S_{n,m} = \phi_l'[i(2m+\epsilon)\hat{\alpha} - i\gamma_r - il\alpha]k_m + \phi_l'''(\gamma_r + i(2n+\epsilon)\hat{\alpha})$$

$$- \phi_l[il\alpha k_m]\frac{d}{dy} + \phi_l''(il\alpha)\frac{d}{dy}$$

$$+ \phi_l'[i(l\alpha - (2m+\epsilon)\hat{\alpha} - i\gamma_r)]\frac{d^2}{dy^2} + \phi_l(il\alpha)\frac{d^3}{dy^3}, \tag{2-43}$$

where

$$k_n = \beta^2 - (\gamma_r + i(2n+\epsilon)\hat{\alpha})^2, \tag{2-44}$$

and

$$D_n = \frac{d^2}{dy^2} - K_n. \tag{2-45}$$

The secondary instability eigenvalue problem is completed by introducing the homogeneous boundary conditions and leads to a characteristic equation of the form

$$F(\alpha,\beta,\sigma,\gamma,Re,A) = 0. \tag{2-46}$$

2.5.2 Classification of Modes

The abundance of parameters in the secondary instability problem allows a rich number of physically interesting phenomena. Perhaps the most visible evidence of the richness of secondary instabilities is the multiplicity of possible streamwise structures.

The streamwise structure is represented by the parameter ϵ that controls the streamwise periodicity of the disturbed flow. According to the value of ϵ, the secondary instability modes can be classified as follows:

- fundamental modes for $\epsilon = 0$
- detuned modes for $-1 < \epsilon < 1$
- subharmonic modes for $\epsilon = 1$

Using this classification, the solution (2-33) can be, alternatively rewritten as follows:

for fundamental modes,

$$\mathbf{v}_f = e^{\sigma t} e^{i\beta z} e^{\gamma_r x} \sum_{m \ even} \hat{\mathbf{v}}_m(y) e^{im\hat{\alpha}x}, \tag{2-47}$$

for subharmonic modes,

$$\mathbf{v}_s = e^{\sigma t} e^{i\beta z} e^{\gamma_r x} \sum_{m \ odd} \hat{\mathbf{v}}_m(y) e^{im\hat{\alpha}x}, \tag{2-48}$$

and for detuned modes,

$$\mathbf{v}_d = e^{\sigma t} e^{i\beta z} e^{\gamma_r x} \sum_{m \ even} \hat{\mathbf{v}}_m(y) e^{i(m+\epsilon)\hat{\alpha}x}, \tag{2-49}$$

or

$$\mathbf{v}_d = e^{\sigma t} e^{i\beta z} e^{\gamma_r x} \sum_{m \ odd} \hat{\mathbf{v}}_m(y) e^{i(m+\hat{\epsilon})\hat{\alpha}x}, \tag{2-50}$$

where

$$\hat{\epsilon} = \epsilon + 1. \tag{2-51}$$

Fundamental and subharmonic modes are associated with primary resonance and principal parametric resonance in the Floquet system, respectively. They have been studied previously using expressions (2-47) and (2-48). Detuned modes are related to combination resonance. We analyze detuned modes for the first time here using expressions (2-49) or (2-50). As we will discuss further in section (2.5.4), a physical solution requires two complex conjugate detuned modes with opposite detuning ϵ. We denote the real disturbance consisting of the detuned modes with both detunings by $+\epsilon$ and $-\epsilon$ as *combination mode* .

Although the odd and even solutions may give the appearance of representing two distinct classes of solutions, they are equivalent. Because no assumption is made of the size of ϵ in equation (2-33), ϵ can be set equal to 1. Renumbering the Fourier series (2-49) and (2-50) then turns the even series into odd ones and vice versa. Therefore, fundamental modes are either even solutions with $\epsilon = 0$, that gives expression (2-47) or odd solutions with $\hat{\epsilon} = 1$. Similarly, we can consider subharmonic modes using even series and $\epsilon = 1$ or using odd series and $\hat{\epsilon} = 0$ as in (2-48). Moreover, since ϵ is a continuous

variable, a smooth path is established between odd and even series by varying ϵ. Therefore, although odd and even solutions are decoupled, they are analytically connected by detuned or combination modes.

The discussion in the previous paragraph also reveals that detuned modes provide the analytical connection between the fundamental and subharmonic modes. The existence of the continuous class of modes connecting the more widely studied subharmonic and fundamental modes implies that the spectrum of the secondary instability is continuous in the streamwise direction.

2.5.3 Growth Concepts

Secondary disturbances, like their classical counterparts, can growth in space or time. The physical relevance of either grow concept depends on the particular problem. For further discussion, the reader should consult the book of Drazin & Reid (1981).

For simplicity, the secondary instability theory has been formulated in the Galilean frame moving with the TS wave. However, for comparison with experiments and to clarify growth concepts, the solution in should be rewritten in the laboratory frame. Accordingly, the secondary instability velocity profile is given by

$$\mathbf{v}_3 = e^{[(\sigma_r - \gamma_r c) + i(\sigma_i - \epsilon\hat{\alpha} c)]t}\, e^{[(\gamma_r - \epsilon\hat{\alpha} i)]x'} \sum \hat{\mathbf{v}}_n(y)\, e^{2in\hat{\alpha}(x' - ct)}. \quad (2\text{-}52)$$

In expression (2-52), we can identify

- the frequency detuning : $\sigma_i - \epsilon c\,\hat{\alpha}$,
- the streamwise detuning : $\epsilon\hat{\alpha}$,

- the temporal growth : $\sigma_r - \gamma_r c$,
- and the spatial growth : γ_r .

Expression (2-52) allows a clear disclosure of the growth characteristics of the secondary instability modes. Consequently, we can distinguish temporally and spatially growing modes.

Temporally growing modes are modes in which $\gamma_r = 0$ while σ is regarded as the eigenvalue of the problem. The temporal growth rate is given by σ_r, and σ_i can be interpreted as frequency shift with respect to the TS frequency. Modes with $\sigma_i = 0$ travel synchronously with the TS wave.

Similarly, for pure *spatially growing modes,* the temporal growth should not exist. Since the equations have been developed in a moving frame, we choose $\sigma_r = \gamma_r c_r$ to suppress temporal growth effects. In this way, we can obtain the spatial growth as measured in the laboratory. The real and imaginary parts of the eigenvalue γ represent the spatial growth rate and the streamwise wavenumber shift, respectively.

In addition to pure temporal or spatial growth, it is possible to analyze waves growing both temporally and spatially by specifying appropriate values of ϵ and σ_i.

The temporal stability analysis is computationally simpler because the eigenvalue σ appears linearly. The standard tools of linear algebra are available in this approach to find the solution. The whole spectrum of eigenvalues can be easily calculated. On the other hand, in the spatial stability analysis the eigenvalue appears nonlinearly. Therefore, the computational work is more involved. Bertolotti (1985) has extended Gaster's work and developed approximate analytical expressions that relate the temporal and spatial growth

rates for modes of secondary instability. Bertolotti has shown that the transformation

$$\gamma_r \approx \sigma_r / c_r \tag{2-53}$$

used by Herbert (1984) represents the leading term of the temporal-spatial transformation and is sufficiently accurate for practical purpose. The corrections to this leading term due to dispersive effects are negligible. Relation (2-53) is quite different from Gaster's transformation for primary modes which is strongly affected by dispersion. The simple relation (2-53) also *helps to understand the success of temporal computer simulations in reproducing the characteristics of spatially developing transition* (Herbert 1987).

2.5.4 Properties of the System.

A careful examination of the system of partial differential equations (2-34), (2-35), and (2-36) reveals interesting properties useful in interpreting results and in saving computational resources.

The system of partial differential equations (2-34), (2-35) and (2-36) is a linearized version of the secondary instability equations. Therefore, any solution can be expressed as a linear combination of solutions of the form of (2-30). For simplicity, the system is written using complex variables. However, the physical solution must be in the *real* space. Only the real subset of linear combinations has physical meaning and is experimentally observable.

The general real solution can be expressed in terms of complex forms of the solution (2-30) ($\mathbf{v}_3(\sigma,\beta,\Theta)$) as follows

$$\mathbf{v}_3(\sigma,\beta,\Theta) + \mathbf{v}_3(\sigma^\dagger,\beta,\Theta) +$$

$$\mathbf{v}_3(\sigma,-\beta,\Theta) + \mathbf{v}_3(\sigma^\dagger,-\beta,\Theta) +$$

$$\mathbf{v}_3(\sigma,\beta,-\Theta) + \mathbf{v}_3(\sigma^\dagger,\beta,-\Theta) +$$

$$\mathbf{v}_3(\sigma,-\beta,-\Theta) + \mathbf{v}_3(\sigma^\dagger,-\beta,-\Theta). \tag{2-54}$$

This solution accounts for all the complex conjugates. It is not necessary, however, to explicitly calculate all the solutions considered in (2-48) . A close examination of the system reveals symmetries that reduce greatly the actual number of computations performed.

The spanwise wavenumber β appears only in quadratic form in equations (2-34) and (2-35). Therefore, the velocity components u_3 and v_3 of a solution for a given spanwise wavenumber β are identical to the velocity components of the solution for $-\beta$. In other words, the system exhibits the symmetry

$$u_3(\sigma,\beta,\Theta) = u_3(\sigma,-\beta,\Theta). \tag{2-55}$$

$$v_3(\sigma,\beta,\Theta) = v_3(\sigma,-\beta,\Theta). \tag{2-56}$$

On the other hand, the presence of the first power of β in the continuity equation (2-36) indicates that the w_3 velocity component has the symmetry

$$w_3(\sigma,\beta,\Theta) = w_3^\dagger(\sigma,-\beta,\Theta). \tag{2-57}$$

Physically, the symmetries (2-55), (2-56), and (2-57) reflect the existence of two symmetric oblique waves.

As expression (2-54) shows, the real solution includes the complex solution with detuning Θ , and the solution with detuning $-\Theta$ to account for the complex conjugate pair required. This pair of detuned modes constitutes the ***combination resonance mode.*** From the mathematical point of view, the simultaneous appearance of waves corresponding to Θ and $-\Theta$ observed in the experiments of Kachanov & Levchenko arises from the *reality* condition of the

linear system, not from a non-linear mechanism.

Simplification of the solution procedure can be achieved by observing that the streamwise and normal Fourier components of the detuned modes have the symmetry

$$u_n(\sigma,\beta,\Theta) = u^{\dagger}_{-n}(\sigma,\beta,-\Theta) \tag{2-58}$$

$$v_n(\sigma,\beta,\Theta) = v^{\dagger}_{-n}(\sigma,\beta,-\Theta) \tag{2-59}$$

and that the continuity equation gives the symmetry for the spanwise Fourier component

$$w_n(\sigma,\beta,\Theta) = w^{\dagger}_{-n}(\sigma,\beta,-\Theta). \tag{2-60}$$

2.5.5 Properties of the Modes

Independent of the basic flow, there are certain intrinsic properties of the secondary instability modes. Fundamental modes are doubly periodic with wavelengths λ_x and λ_z. Flow visualizations of passive particles show aligned pattern of Λ-shaped structures like in the experiments of Saric & Thomas (1984). An associated longitudinal vortex system and a mean flow distortion (u_0) are produced due to the aperiodic term $\mathbf{v}_0$ in (2-47). This result is consistent with observations of Klebanoff et al (1962).

Subharmonic modes are doubly periodic with wavelengths $2\lambda_x$ and λ_z. Flow visualizations show a staggered pattern of Λ-shaped structures. Due to the absence of aperiodic components in the Fourier series (2-48), subharmonics modes are not associated with longitudinal vortex systems or mean flow

distortions. Moreover, the frequency spectra of (linear) subharmonic modes consists only of odd multiples of the subharmonic frequency.

As mentioned before, we have extended the parametric model, and we have shown that fundamental and subharmonic are special cases of a more general class of solutions. These solutions include combination modes and both temporal and spatial growth concepts.

Most experimental and theoretical efforts have been directed toward understanding subharmonic and fundamental modes. Here, we will try to discuss the importance of the less studied combination resonance modes in the transition process. Although most of our work uses the temporal stability analysis, the existence of temporal-spatial transformations guarantee the generality of our findings.

Studying combination modes can be motivated on mathematical and physical grounds. In a mathematical sense, it is valuable to investigate the behavior of modes in the neighborhood of subharmonic and fundamental modes. In a physical sense, the interest lies in the variation on the growth rate of these modes and in the bandwidth of the boundary layer response. Very limited evidence for the occurrence of combination modes can be extracted from natural and controlled transition experiments. This study will attempt to explain the scarce observations. It is likely though that combination resonance has prevailed in many other hot-wire experiments and flow visualizations without being clearly discerned.

Results of our linear secondary instability theory reveal that combination modes can be regarded as the most general parametric instability excited by a single TS wave. In the almost uniform low-turbulence background of realistic

flight conditions, a wide range of detuned modes is likely to be excited and will produce a broadband response in the frequency spectrum. Two factors will contribute to the broadness of the band: the multiplicity of TS waves that can be excited and the multiplicity of secondary waves that can be excited by the individual TS waves. Only the second factor will be addressed because it is probably more important in understanding the transition process.

For all kinds of modes, the three-dimensional disturbances behave as a whole. In the linear range, all Fourier components must be considered simultaneously. Therefore, the phase speed is unique and identical for all components.

2.6 Numerical Aspects

2.6.1 Spectral Methods

The numerical solution of the system of differential equations (2-34), (2-35) and (2-36) discussed in the preceding chapter is obtained by a spectral-collocation method. Spectral methods are one of the most powerful techniques presently available for large-scale computational fluid dynamics. Although the fundamental ideas have been widely used since the mid-nineteenth century, the effectiveness of spectral methods has been enhanced by developments in computers and algorithms during the 1970's. Details and further discussion of these methods can be found in the review of Hussaini & Zang (1987) and in the monographs of Gottlieb & Orszag (1977) and Canuto, Hussaini, Quarteroni & Zang (1987). Essentially, the solution, $u(y)$, is expressed in terms of an infinite series of a complete set of orthogonal functions $u(y) = \sum a_k T_k(y)$. The coefficients a_k are the unknowns of the problem. For better

approximation, the expansion functions T_k are usually selected so that the coefficient a_k decays faster than any power of k (spectral accuracy). The widely used Fourier series are examples of spectrally accurate expansions of periodic smooth functions. More generally, spectrally accurate expansions of *any* smooth function are obtained when eigenfunctions of a singular Sturm-Liouville problem are employed. In particular, expansions based on Chebyshev polynomials are of common use in hydrodynamic problems.

In addition to selecting the expansion functions, spectral methods require an efficient way of projecting the infinite-dimensional solution onto a finite subspace. Here, we use a collocation method, sometimes called pseudospectral approximation. The projection P_N is made such that $P_N u = u$ for a selected set of *collocation points* y_j. In our case, those selected points coincide with the nodes of a Gauss-type quadrature assuring a very good approximation.

Derivatives of the function $u(y)$ are approximated by analytical derivatives of the expansion functions $T_k(y)$. Usually, the derivatives of the expansion functions can be easily expressed in terms of the expansion functions themselves. Therefore the original differential equation as a whole can be rewritten in terms of the known set of functions $T_k(y)$. The differential equation is then transformed into an algebraic problem for the coefficients a_k. This problem can be easily solved by traditional methods of linear algebra. For example, the eigenvalue problem is usually solved globally by the QR algorithm and locally by the inverse power method or Wielandt's iteration method.

Since the domain of the solution is unbounded for both boundary layer and free shear layer, it seems natural to choose Laguerre or Hermite polynomials that span the whole unbounded domain. However, these expansion function have relatively poor resolution properties (Gottlieb & Orszag 1977). A better approach is to solve the differential equation in a transformed bounded domain. In the bounded domain, a set of expansion functions with better convergence properties such as Fourier series or Chebyshev polynomials is then employed.

We follow this latter approach and restrict the computational domain to the interval [0,1] or [-1,1]. For boundary layers, the semi-infinite physical domain is mapped onto [0,1] by using an algebraic or an exponential transformation. For the shear layer, the infinite domain is mapped onto [-1,1] by an algebraic, an exponential, or a trigonometric transformation.

Another important aspect in the formulation of the spectral method is the treatment of the boundary conditions. In the approach chosen here, the boundary conditions are enforced at the appropriate collocation points. This is achieved either by chosing approximating functions that satisfy the boundary conditions or by explicitly enforcing them. The latter alternative will result in an augmented algebraic system, i.e. in a number of coefficients larger than the number of collocation points..

The derivatives in the original (physical) domain can be expressed in the bounded (computational) domain using the chain rule. Let $\hat{y}$ and y be the independent variables in the physical and computational domain, respectively. The derivatives of a function F with respect to $\hat{y}$ can then be written in terms of derivatives with respect to y as follows:

$$F(\hat{y}) = F(y(\hat{y})) \tag{2-61}$$

$$\frac{dF}{d\hat{y}} = \frac{dF}{dy}\frac{dy}{d\hat{y}} \tag{2-62}$$

$$\frac{d^2F}{d\hat{y}^2} = \frac{d^2F}{dy^2}\frac{dy^2}{d\hat{y}} + \frac{dF}{d\hat{y}}\frac{d^2y}{d\hat{y}^2} \tag{2-63}$$

$$\frac{d^3F}{d\hat{y}^3} = \frac{d^3F}{dy^3}\frac{dy^3}{d\hat{y}} + 3\frac{d^2F}{dy^2}\frac{dy}{d\hat{y}}\frac{d^2y}{d\hat{y}^2} + \frac{dF}{d\hat{y}}\frac{d^3y}{d\hat{y}^3} \tag{2-64}$$

$$\frac{d^4F}{d\hat{y}^4} = \frac{d^4F}{dy^4}\frac{dy^4}{d\hat{y}} + 6\frac{d^3F}{dy^3}\frac{dy^2}{d\hat{y}}\frac{d^2y}{d\hat{y}^2} + 3\frac{d^2F}{dy^2}\frac{d^2y^2}{d\hat{y}^2} + 4\frac{d^2F}{dy^2}\frac{dy}{d\hat{y}}\frac{d^3y}{d\hat{y}^3} + \frac{dF}{d\hat{y}}\frac{d^4y}{d\hat{y}^4} \tag{2-65}$$

2.6.2 Choice of Approximating Functions

Selection of the set of approximating functions is an essential aspect of spectral methods. Generally speaking, the best results are obtained when these approximating functions are chosen among eigenfunctions of a Sturm-Liouville problem. Among those, Fourier and in Chebyshev series are very popular selections because of their excellent accuracy in a wide range of problems. In addition, fast Fourier transforms (FFT) can be used to reduce the computational time. The FFT can also be used with Chebyshev polynomials, since their expansions reduce to cosine series. The existence of FFTs make Fourier and Chebyshev series particularly attractive in solving nonlinear and multi-dimensional problems. Fourier series are advantageous when the boundary conditions are periodic but may suffer from poor convergence (Gibbs' phenomenon) in aperiodic domains. Chebyshev expansions are superior in the case of aperiodic boundary conditions.

2.6.2.1 Trigonometric polynomials (Fourier series) We used Fourier series in the interval [-1,1] to solve the secondary instability problem in the free-shear layer case. In this interval, Fourier series can be written as a regular Sturm-Liouville problem as follows

$$u'' + \lambda u = 0, \tag{2-66}$$

with the homogeneous boundary conditions

$$u(-1) = u(1) = 0. \tag{2-67}$$

The eigenvalue of this problem λ_k is $\frac{\pi k}{2}$. As expected, we choose the expansion functions as the eigenfunctions of (2-66) that are given by

$$T_k(y) = \cos k\pi y/2, \quad for \ k \quad odd \tag{2-68}$$

$$T_k(y) = \sin k\pi y/2, \quad for \ k \quad even \tag{2-69}$$

When Fourier series are used, the appropriate collocation points are equally spaced. In the interval [-1,1], they are given by:

$$y_j = 2\frac{j-1}{JJ-1} - 1, \quad with \quad 1 < j \leq JJ \tag{2-70}$$

where JJ is the total number of collocation points.

2.6.2.2 Chebyshev polynomials We use Chebyshev polynomials in both the boundary layer and the free-shear layer case. The computational domains chosen are the intervals [0,1] and [-1,1], respectively. Chebyshev polynomials can be regarded as the eigenfunctions of the singular Sturm-Liouville problem

$$[-(1-y^2)^{\frac{1}{2}}u']' = (1-y^2)^{-\frac{1}{2}}\lambda u. \tag{2-71}$$

with homogeneous boundary conditions at -1 and 1. The eigenvalues of (2-71)

are $\lambda_k = k^2$.

As usual, the expansion functions T_k correspond to the eigenfunctions of (2-71) and are given by

$$T_k(x) = \cos k \tag{2-72}$$

with homogeneous boundary conditions at -1 and 1. The eigenvalues of (2-71) are $\lambda_k = k^2$.

As usual, the expansions functions T_k correspond to the eigenfunctions of (2-71) and are given by

$$T_k(x) = \cos k\theta\ , \qquad \theta = \arccos x. \tag{2-72}$$

Several choices of the collocation points are available. Here, we follow Lanczos' (1957) choice that has given excellent results. He recommends to select the positions of the extreme values of the last polynomial retained. For the free-shear layer case, the collocation points are

$$y_j = \cos\left(\frac{j\pi}{JJ - 1}\right). \tag{2-73}$$

where $j = 1, 2, \ldots, JJ$

In the boundary layer case, it is advantageous to map $\hat{y} = \infty, 0$ into the half interval $y = 0,1$, respectively, and use only odd polynomials. This choice satisfies automatically the boundary conditions at infinity. The collocation points in the interval [0,1] are given by

$$y_j = \cos\left(\frac{j\pi}{2JJ - 1}\right). \tag{2-74}$$

2.6.3 Choice of Mappings

The domain of solution for the free-shear layer and the boundary layer is unbounded. As discussed earlier, the best results are obtained when the unbounded domain is mapped into a bounded one and then spectral methods are applied.

For boundary layers, only the half interval is used. The other half is reflected about $y = 0$ by choosing odd Chebyshev polynomials. The transformation of the semi-infinite domain [0, ∞) into [1,0] can be achieved by an exponential or an algebraic mapping. Using these mappings the boundary conditions at infinite are automatically satisfied.

The exponential mapping is given by

$$y = \exp\left(-\frac{\hat{y}}{\eta_0}\right), \tag{2-75}$$

This mapping (2-75) has been used by Kleiser et al. (1985) and Spalart et al. (1986) in numerical simulations. The algebraic transformation is given by

$$y = \frac{\eta_0}{\hat{y}} - \eta_0. \tag{2-76}$$

In our study we prefer this mapping that has been used extensively by Herbert. We found that the algebraic mapping performs slightly better.

For shear flows, three transformations were used : the algebraic

$$y = \frac{\hat{y}}{\sqrt{\hat{y}^2 + \eta_0^2}}, \tag{2-77}$$

the hyperbolic

$$y = \tanh\frac{\hat{y}}{\eta_0}, \tag{2-78}$$

and the trigonometric

$$y = \text{arccot}\frac{\hat{y}}{\eta_0}. \tag{2-79}$$

Again, the boundary conditions at both ends (infinite) are automatically satisfied. The algebraic and the hyperbolic transformations have been used by Metcalfe et al. (1987). The trigonometric transformation has been used by Cain et al. (1981). As we will discuss in chapter 4, we compare results using different combination of mappings and approximation functions. Looking rates of convergence to the principal eigenvalue, the number of polynomials necessary to achieve a predetermined accuracy and the independence of the results to the mapping parameter, we found that the method based on the algebraic mapping and Chebyshev polynomials has the best properties. In fact, all mappings perform acceptably with Chebyshev polynomials. However, only the trigonometric mapping is advisable when Fourier series are used.

3. BOUNDARY LAYERS

3.1 General Comments

Carefully controlled experiments in the Blasius boundary layer reveal that transition to turbulent flow follows a cascade of weak (viscous) and strong (vortical) instabilities. Each new stage brings about characteristic qualitative changes in the structure of the flow. In boundary layers, three stages have been clearly recognized.

The first stage or primary instability occurs with respect to two-dimensional TS waves. Considerable understanding of the transition process was gained after Schubauer & Skramstad (1948) confirmed experimentally the predictions of the classical stability theory developed by Tollmien (1929) and Schlichting (1933). This classical theory is linear and predicts whether these TS waves grow or decay according to the Reynolds number, the streamwise wavelength $\lambda_x = 2\pi/\alpha$, and the frequency ω. In the absence of further perturbations, these waves take on a finite amplitude and then decay.

The second stage or secondary instability occurs with respect to three-dimensional disturbances. The new characteristic length is represented by the spanwise wavelength λ_z that has been observed to be comparable to λ_x. Secondary instabilities originate from parametric instabilities of the almost periodic flow formed at the first stage. The pattern of secondary instabilities is easily recognized by the occurrence of Λ-shaped smoke accumulations in smoke-flow visualizations.

The third stage or tertiary instability is characterized by small-scale high-frequency disturbances (spikes). This stage was originally misinterperted

as a secondary instability. Currently, this third stage is viewed as a vortical instability of the highly inflectional instantaneous velocity profile resultant from the second stage.

Our study will focus mainly on the second stage of the cascade of instabilities discussed above. The importance of this stage in the transition process is made apparent by comparing the streamwise distance overwhich it occurs. Typically, the secondary instability region embraces five TS waves, and the tertiary instability leads to breakdown within one TS wave. Therefore, an accurate understanding of secondary instability is essential for transition prediction and control.

3.1.1 Experimental Aspects

One of the first and most influential observations of the three dimensionality of secondary instabilities was made by Klebanoff & Tidstrom (1959) and is now known as the K-type of breakdown. The careful gathering, appropriate selection, and wide extension of their detailed hot-wire measurements have been extremely valuable in transition research. The K-type of breakdown is characterized by alternating regions of enhanced and reduced wave amplitude, and a longitudinal vortex system. The phenomenon is often referred to as peak-valley splitting and appears as an aligned system of Λ-shaped vortices in flow visualizations, for example, in early work of Hama et al (1957) and Knapp & Roache (1968). These aligned structures are doubly-periodic in the spanwise and streamwise directions. Since the streamwise wavelength is the same as the TS wavelength, peak-valley splitting is also referred to as the fundamental type of secondary instability. Similar structures have been observed in subsequent experiments by Wortmann (1977),

Anders & Blackwelder (1980), Saric (1980), and more recently by Cornelius (1985).

However, experimental results show that the K-type is not a unique route to transition. Another three-dimensional type of secondary instability has been recognized recently by Kachanov & Levchenko (1982), and Thomas & Saric (1981). This second route is characterized by a staggered pattern of Λ vortices with streamwise wavelength twice that of the TS wave. A hot wire aligned along a peak of the Λ shaped structure will measure peaks in velocity at one-half the TS frequency. This route is, therefore, usually referred to as the subharmonic type of secondary instability. Careful reexamination of experiments of Knapp & Roache (1968) shows that they had also observed similar patterns, although the qualitative differences from the K-type were not recognized. Recently, experiments with controlled spanwise wavelength have been performed by Corke at al. (1987).

3.1.2 Theoretical Aspects

Early theoretical work of the secondary instability rested on weakly nonlinear models based on the interaction of some *relevant* primary instability modes. Some of the models regard the spanwise wavelength as a parameter. Such is the case of the Benney-Lin model (1960) that explained the streamwise vortices observed by Klebanoff considering a triad of modes of the Orr-Sommerfeld equation: the TS wave $(\alpha,0)$ and two oblique modes $(\alpha,\pm\beta)$. A more refined model was proposed by Herbert (1980) which included longitudinal vortices of the Orr-Sommerfeld equation $(0,\pm\beta)$ to model the spanwise structure. Another family of models rest on the resonant wave interaction at specific spanwise wavelength. One of the most relevant of these models was

proposed by Craik (1971) (C-type). Craik's model involves the interaction of the TS wave and a pair of symmetric oblique waves at the subharmonic frequency $(\alpha/2,\pm\beta)$. The spanwise wavenumber β corresponds to the oblique mode with the same phase speed as the TS wave. Under certain conditions, Craik's model correctly predicts the spanwise wavelength of the subharmonic mode. Along similar lines, Nayfeh & Bozatli (1979) proposed a four-wave resonant model to explain the secondary instability. After the importance of Squires modes in the transition process was revealed by Herbert's work, a new models has been proposed by Nayfeh (1986). The major drawback of these weakly nonlinear models is the ambiguity in choosing the relevant physical modes. Therefore, the models are often incomplete and unable to reproduce the experimental results.

With the increasing speed of computers and improved computational methods, another possible approach is now available: direct numerical simulation of the transition process. Recently, Spalart & Yang (1986) introduced random three-dimensional disturbances to predict the spanwise structure. Kleiser & Laurien (1986) have also modeled successfully the subharmonic and fundamental types of instabilities. These numerical simulations confirm many experimental observations and theoretical predictions. However, the simulations are time consuming, and the analysis of the results is an intricate task.

In another approach, the secondary instability modes are considered to arise from a parametric instability of the streamwise periodic flow created by finite amplitude TS waves. This interpretation was suggested by Herbert & Morkovin (1980) and Blackwelder (1979) and observed by Orszag & Patera (1983) in computer simulations of plane channel flow. They attributed the fast exponential growth of the three-dimensional disturbances to a new linear

stability mechanism. Because the resulting equations have periodic coefficients, Floquet analysis is usually employed in the solution. Analysis of the limiting case in which the TS amplitude $A \rightarrow 0$ reveals the most relevant modes of primary instability necessary for a successful weakly nonlinear model. Herbert (1983,1984) employed this parametric approach to explain subharmonic and fundamental modes of transition. The quantitative agreement with experiments of Klebanoff and Cornelius on peak-valley splitting and of Kachanov & Levchenko on staggered peak-valley is striking. Moreover, Herbert revealed the importance of the Squires modes and found broadband spanwise subharmonic structures (H-type) distinct from the Craik resonant triad.

Here, we are most interested in the detuned modes that are also parametrically excited. Because detuned modes provide an analytical link between the subharmonic, their excitation is likely to be the mechanism behind the spectral broadening that characterizes turbulence. Because the TS wave excites almost equally a wide range of modes, the continuous spectrum characteristic of the fully turbulent flow start to appear at this stage of the cascade of instabilities.

These detuned modes may also be related to some basic concepts of bifurcation theory. The second frequency that appears as a consequence of the secondary instability together with the primary TS frequency may form the *torus* that occurs in bifurcations of simpler dynamical models.

In the remainder of this chapter, we briefly discuss experimental observations and then present results to show properties of the combination modes. In particular, the broadband response of the secondary instabilities with respect to the streamwise wavenumbers is explained. Also, an exclusive visualization of the spanwise and streamwise structure of a combination mode is

presented.

3.2 Discussion of Experimental Observations

In this section we will discuss experimental observations of transition. According to the control exerted by the experimentalists, we have classified the observations as natural, biased, and controlled transition.

3.2.1 Natural Transition

In the uncontrolled case or "natural" transition experiment the boundary layer is not artificially excited at any frequency. Therefore, the flow will respond to the particular spectrum of background disturbances present in the experiment. Although a "natural" experiment would more accurately mimic realistic flight conditions, the intricate interactions among modes make it desirable to introduce some control to better understand the phenomena. Moreover, such "natural" experiment would be difficult to carry out, since the disturbance spectrum of wind and water tunnels is not uniform but has concealed preferences for certain spectral components.

3.2.2 Biased Transition

In the so-called "biased" transition experiment, the boundary layer is excited at a single frequency. This excitation is done typically by introducing forced oscillations with a loud speaker, a vibrating ribbon, or an array of heating elements.

Figure 3.1, taken from the vibrating ribbon experiments of Kachanov & Levchenko, shows a typical evolution of the amplitude spectra in the streamwise direction. In the initial stages, the boundary layer responds only at the

exciting frequency $f = 114.4$ Hz, in the form of two-dimensional TS waves. Downstream, at $Re \approx 600$, a lower frequency broadband spectrum with two maxima slowly starts to develop. This broadband wave packet is centered at the subharmonic frequency and has very rapid growth rates. Consequently, further downstream, the wave packet quickly reaches the amplitude level of the TS wave. Moreover, the subharmonic frequency emerges as the most amplified disturbance. More detailed measurements reveal that the subharmonic secondary instability is associated with three-dimensionality. Because the low-frequency waves have very large growth rates, experiments have to be conducted in environments with very low turbulence levels. Otherwise, their basic structure could be hidden by strong nonlinear effects and more complicated interactions. Although the most amplified modes correspond to the subharmonic mode, neighboring modes have almost the same amplitude. In natural transition then, quoting Kachanov & Levchenko, *"the parametric resonance leads to the amplification not of a narrow spectral harmonic $f_{1/2}$, but of a rather broad packet of low-frequency fluctuations."* Smoke wire visualizations of the process described above show the initial two-dimensional wave followed by rapidly forming spanwise variations characteristic of the three-dimensional Λ-shaped structures.

3.2.3 Controlled Transition

After the discovery of the importance of the subharmonic mode in the transition process, experiments with controlled two-dimensional subharmonic disturbances were performed by exciting the ribbon simultaneously at the fundamental and at the subharmonic frequency. Consequently, the spectrum shown in Figure 3.2, taken from Kachanov & Levchenko's experiments,

consists of a single narrow peak at the subharmonic frequency and its harmonics. The smoke-wire picture would show a clear staggered Λ-shaped structure as observed by Saric & Thomas (1984).

Some information on controlled detuned modes is also available. To investigate the spectral width of the subharmonic response, Kachanov & Levchenko introduced the second frequency with some detuning Δf with respect to the subharmonic $f_{1/2}$. Interestingly, they observed that when a disturbance with positive detuning was excited, the boundary layer response consisted not only of the mode at the exciting frequency, but also of the mode with opposite detuning. Similar observations were made using negative detunings. That is, detuned modes occur in pairs. Figure 3.2, taken from experiments near branch II (where the TS wave starts decaying), shows the validity of these observations for a wide range and for large magnitudes of detunings.

A close examination of these figures reveals more qualitative information on the physics of the detuned modes. The spectrum shows peaks close to the frequencies $f_{3/2} + \Delta f$ and $f_{3/2} - \Delta f$. The presence of these peaks discloses the *parametric* nature of these instabilities. Moreover, they expose the dominance of *parametric* interactions over *nonlinear* interactions that would produce peaks at $f_{3/2} \pm 2\Delta f$.

Since the observation of the three-dimensional fundamental structures by Klebanoff, many experiments on peak-valley splitting have been made. Smoke-wire visualizations show the aligned Λ vortices or peak-valley structure. Notoriously, the fundamental mode has been invariably associated with the presence of a strong streamwise system of vortices. In experiments conducted by Klebanoff as well as Cornelius, the spanwise control of the structure was

made by spacing cellophane tape under the vibrating ribbon located in the unstable region. This set-up will produce a spanwise modulation of the mean flow and differential amplification of TS waves in the spanwise direction that will form a strong system of longitudinal vortices that preferentially excites the fundamental mode.

3.3 Discussion of Theoretical Results

3.3.1 Truncation of the Series

One of the first objectives of this study was to investigate the numerical accuracy of the solution method for the secondary instability problem developed by Herbert. His studies have already shown that 20 collocation points are adequate in the normal direction. However, the streamwise Fourier series was truncated to two and three components for the subharmonic and fundamental modes, respectively. Therefore, we concentrate on the effects of truncating the streamwise Fourier series. We pay special attention to the results of "asymmetric" truncations, e.g. of using three components for subharmonic modes.

In addition, the accuracy of the fundamental treated as a detuned subharmonic could be investigated. The accuracy of the solution using only two Fourier components obviously deteriorates for modes close to the fundamental as can be seen in figure 3.3. As previously assumed, we determined that two components are appropriate to solve for the subharmonic mode, but at least three Fourier components are necessary for an accurate representation of the fundamental and its neighboring modes. Most of our study therefore, was made using four Fourier modes.

More details on the convergence of the temporal eigenvalue can be seen in the numerical results presented in Table 3.1 for the subharmonic ($\hat{\epsilon} = 0.0$), the detuned ($\hat{\epsilon} = 0.5$), and fundamental ($\hat{\epsilon} = 1.0$) modes. The results are from solutions using Chebyshev polynomials with 20 and 30 collocation points. The rapid convergence of the streamwise Fourier series is obvious. The approximations using only three or four components agree with results using more Fourier modes within 1% over the full range of wavenumbers. The asymmetry of the model representing subharmonic modes with an odd number and fundamental modes with an even number of Fourier components introduces only a small error as can be seen more clearly on the small imaginary part of the tuned modes.

3.3.2 Variation of Growth Rates with Detuning

Figure 3.4 and Table 1 show the influence of the detuning parameter ϵ on the temporal eigenvalue σ. The parameters used correspond to one set of parameters in the experiments of Kachanov & Levchenko. The non-dimensional frequency, spanwise, and streamwise wavenumbers are $F = 124$, $\alpha = 0.2033$, and $\beta = 0.2$, respectively. The station coincides with branch II ($Re = 606$), and the amplitude of the TS wave is 1%.

Although our results are for the temporal instability case, the availability of a transformation of the temporal growth rates to the spatial case allows us to discuss important aspects of the secondary instability problem. We recall that the frequency of the first Fourier component is given by $c\,\epsilon\hat{\alpha} - \sigma_i$. Then, because σ_i is relatively small, the behavior of the frequency spectra is given mainly by $c\,\epsilon\hat{\alpha}$. We observed that the maximum growth rates correspond to the subharmonic ($\epsilon = 1.0$), but the broadband nature of the

secondary instability can be easily recognized.

We also recall that the temporal eigenvalue is real only for the subharmonic and fundamental modes. Therefore, the combination modes do not travel synchronously with the TS wave.

3.3.3 Variation of Growth Rates with TS Amplitude

Similar results using four Fourier components to represent the subharmonic symmetrically are shown in figure 3.5 for several amplitude levels of the TS wave. At small amplitudes around 0.2%, only the subharmonic and its neighbors are unstable while the fundamental instability is suppressed. Growth rates for all modes increase with the TS amplitude. At a slightly higher amplitude, approximately 0.5%, all modes become unstable. However, the growth rates of the subharmonic and a wide range of detuned modes are still much larger than the fundamental mode. For larger amplitudes ($\approx 3\%$), all modes tend to be equally unstable and likely to be observed if they are present in the background. These large amplitudes, however, are not characteristic of boundary layers with zero pressure gradient.

A careful analysis of the limit $A \rightarrow 0$ has shown that the spanwise wavenumber of the most unstable subharmonic mode at small amplitudes corresponds to Craik's resonant triad. Because the results in figure 3.5 use the observed spanwise wavenumber at low TS amplitudes, these results are not representative for the Craik mechanism.

The temporal eigenvalue is real for the subharmonic and some intermediate combination modes as can be seen in figure 3.5. On the other hand, the small imaginary part of the fundamental mode is due to the low truncation of

the Fourier series that produces an asymmetric representation. More accurate results show that the fundamental temporal eigenvalue is indeed real.

The stronger subharmonic growth for low and medium amplitudes seems to be a generic result for a wide range of parameters. For large amplitudes, the selectivity is so weak that observed modes depend almost exclusively on the spectral content of the background. Moreover, a mixed pattern is well possible as Spalart & Yang's numerical simulations and Saric's et al. (1984) experiments seem to indicate. At large amplitudes, the instability is not necessarily of fundamental type as is often believed. Strong longitudinal vortices are also necessary to preferentially excite the fundamental.

3.3.4 Variation of Growth Rates with the Spanwise Wavenumber

Figure 3.8 shows variation of the growth rate σ_r with the spanwise wavenumber β for various modes at the fixed amplitude $A = 1\%$. This amplitude is slightly higher than the threshold value for all modes. The broadband spectrum and long wavelengths in the spanwise direction are characteristics shared by all modes of secondary instability. Therefore, it is possible to excite a wide range of spanwise wavenumbers and to observe them experimentally. The theoretical selected mode that corresponds to the maximum amplification rate remains in the neighborhood of $\beta = 0.2$ for all modes. The sharp cutoff at low wavenumbers indicates that the two-dimensional secondary instability (vortex pairing) mode is suppressed by the presence of the wall.

3.3.5 Evolution of the Secondary Instability Modes

The amplitude evolution of the instability modes with the streamwise position can be seen in figure 3.9. Again the nondimensional frequency is $F = 124$ and the non-dimensional wavenumbers are $a \approx 0.335$, $b = 0.33$. We obtained this evolution curve by integration of the spatial growth rates as follows:

$$\ln(\frac{B}{B_0}) = -2\int_{Re_0}^{Re} \gamma dRe. \tag{3-1}$$

Spatial growth rates can be expressed in terms of temporal rates by the transformation:

$$\gamma = -\frac{\sigma}{c_r}. \tag{3-2}$$

This transformation first employed by Herbert (1983) has been proved accurate within 2% for subharmonic modes by Herbert & Bertolotti (1985) who solved the spatial instability problem directly. The initial amplitudes of the subharmonic mode B_0 , following Herbert, is chosen so that the theoretical amplitudes coincide with the experimental values that are also shown in figure 3.9. The amplitude growth curve of the subharmonic mode is in very good agreement with the experimental observations of Kachanov (Herbert 1983). Because of the scarce documentation available on other modes, we assume uniform disturbance background so that the initial amplitudes for all modes are assumed to have the same level as the subharmonic (B_0).

According to the classical stability theory, as figure 3.9 shows, the TS wave starts growing at branch I and decays after branch II. Due to the small growth rates of the viscous TS instability, the amplitude of the TS wave

remains at the same order of magnitude throughout the unstable region. On the other hand, the secondary instability modes evolve in a convective time scale. Although initially small, the amplitudes rapidly increase gaining several orders of magnitude. As a consequence, secondary instability dominates the TS instability and emerge as the principal mechanism of transition.

Although the subharmonic mode is most amplified, spectrally similar modes undergo similar development and reach comparably high amplitudes. On the other hand, the maximum amplitudes reached by modes in the neighborhood of the fundamental are almost two order of magnitude lower and are less likely to occur under these conditions.

Secondary instability waves grow so fast that some modes can reach unrealistically high amplitudes (almost 100%). Of course, these amplitudes can not be considered sufficiently small for our linear model to be valid. In addition, after branch II, the decay of the TS wave produces an attenuation of the parametric oscillator that turns off the secondary instability. Therefore, the mutual interaction between the TS and the secondary intability waves must be considered to realistically model the self-sustaining mechanism that ultimately leads to breakdown. Work on this subject is in progress by Crouch & Herbert (1986).

On the other hand, for smaller amplitudes of the TS wave, (0.5% and 0.2% at branch II) as seen in figures 3.10 and 3.11, the amplitude of secondary instabilities may still be considered small. Non-linear interactions can be neglected, and the decay of the secondary instability wave is indeed possible.

3.3.6 Evolution of the Spectra

The integration of growth rates allows us to model the streamwise evolution of spectra as in the natural transition experiment. We obtain these spectra by superposing discrete frequency responses of selected secondary instability modes. Figures 3.13 and 3.14 show the evolution of the spectra for frequencies ranging from 0 to the fundamental frequency. The frequency detuning, as discussed in chapter 2, is given by $\sigma_i - \epsilon c\,\hat{\alpha}$. The value of σ_i is usually small and has been neglected as in figure 3.13. Correct values of frequences are used in figure 3.14.

For a given combination mode, two components of the streamwise Fourier series have frequencies inside the interval $(0, 2\hat{\alpha}c)$. The component with $n = 0$ and positive detuning ϵ is associated with a frequency of $c\,\hat{\alpha}\epsilon - \sigma_i$. Similarly, the Fourier component with $n = 1$ and negative detuning $-\epsilon$, has a frequency of $c\,\hat{\alpha}(2 - \epsilon) + \sigma_i$. We recall that this mode is equivalent to the mode with positive detuning and $n = -1$ and frequency $c\,\hat{\alpha}(2 + \epsilon) - \sigma_i$. The value of σ_i for the mode with negative detuning has been changed to the corresponding σ_i with positive detuning.

It is implicitly assumed that the disturbance background is uniform and that all interactions among secondary instability modes are negligible. The evolution shows qualitative agreement with the experiments. As expected, the broadband nature of the frequency response is apparent. The frequency response to the white noise is initially almost uniform and evolves slowly as can be seen in figures 3.13 and 3.14 just downstream branch I ($Re \approx 500$). However, further downstream at $Re \approx 550$, the amplitudes in a certain range of frequencies start growing quickly. Eventually, near branch II, a broadband

packet centered at the subharmonic frequency reaches appreciable amplitudes and starts to emerge as the dominant form of instability.

In figures 3.13 and 3.14, the amplitude of the primary instability mode is represented by small symbols at the fundamental frequency. In our theoretical analysis, separating the three-dimensional (secondary) responses from the two-dimensional (primary) is trivial. However, in the experiments, the response at the fundamental frequency will include primary as well as secondary modes.

It is interesting to note the slow appearance of a small peak at very low frequencies. This small peak represents a low-frequency modulation and is associated with near fundamental modes. Saric & Reynolds (1980) have experimentally reported this phenomena. This modulation is thought to play an important role at latter stages of the cascade of instabilities, where higher order interactions lead to the broadening of the spectrum and consequently to chaotic behavior.

Figures 3.13 and 3.14 also help us to interpret spectra of experiments with controlled discrete frequencies. If the vibrating ribbon is simultaneously excited subharmonic and at the fundamental frequencies, we obtain a response with maximum amplitude at the subharmonic frequency. If a frequency with some detuning Δf (from the subharmonic) is introduced, as discussed in previous chapters, the frequency response consists not only of the mode with detuning Δf but also of the mode with detuning $-\Delta f$. Both modes are necessary for a real solution and constitute the combination resonance in boundary layers. If we assume that all other modes start with smaller initial amplitudes, they can be neglected. The magnitudes of the amplitudes at several streamwise locations for the combination modes are given by the corresponding values in the figure.

3.3.7 Velocity Profiles

The rms velocity profiles of the streamwise disturbances for $\epsilon = 0$, 0.5 and 1.0 are shown in figures 3.15, 3.16, and 3.17, respectively. Because these components are difficult to measure, distributions of higher harmonic are also included. For the subharmonic mode, Figures 3.18 and 3.19 also include the available experimental distributions. As previously reported, the agreement of subharmonic mode with experiments is excellent. Quantitative agreement is also obtained for higher modes when each mode is normalized with respect to its maximum as shown in figure 3.19. The similarity of the overall shape shape of the profiles and the location of the various maxima and minima is surprising. The ratios of the maximum amplitudes for the Fourier modes are a result of our theoretical model because we solve a coupled system for the Fourier coefficients. We found, however, a major disagreement of these ratios with the experimental data. When normalizing with respect to the maximum of the subharmonic, we obtain maximum amplitudes of 3.7% and 0.2% for the $3\hat{\alpha}$ and $5\hat{\alpha}$ modes respectively, while the corresponding experimental values are 2.5% and 0.4%. Disagreements in the amplitude levels as well as differences in shape of the profiles near the wall can be attributed to experimental errors in measuring values at small magnitudes and the difficulties measuring in the proximity of the wall.

The small amplitude of the higher harmonics in the figures 3.15, 3.16 and 3.17 confirm the high accuracy of low-order Fourier approximations. In fact, there are only two significant component for the subharmonic ($-\hat{\alpha}$ and $\hat{\alpha}$), three for the fundamental ($-2\hat{\alpha}$, 0 and $2\hat{\alpha}$) and four for the combination mode presented ($\pm\,\hat{\alpha}/2$ and $\pm\,3\hat{\alpha}/2$).

The zero wavenumber component of the fundamental mode causes different mean velocity profiles at the peak and valley and generates the longitudinal vortex system. Similarly, the fluctuating component causes different rms distributions at peak and valley as shown in figure 3.20.

The intriguing little bump near the wall shown for the fundamental and the combination mode also appears for other combination modes. However, it decreases as ϵ increases and eventually vanishes for the subharmonic mode. The proximity of this bump to the wall is probably the reason it has not been observed in experiments.

3.3.8 Visualization of the Spanwise Structures

Figures 3.21, 3.22, and 3.23 taken from a computer animation, (Bertolotti, Santos Herbert & (1986) and Bertolotti & Herbert (1987)) show the streaklines of passive particles released at the critical layer. The characteristic staggered pattern of the subharmonic mode is presented in figure 3.21 and the classical aligned pattern of peaks and valleys of the fundamental mode is shown in figure 3.22. The subharmonic mode has a streamwise wavelength twice that of the TS wave. In the former case, the streamwise wavelength of the Λ-vortex array is double the wavelength of the two-dimensional finite amplitude TS wave. In the latter case, the streamwise wavelength of the pattern corresponds to the TS wavelength. These computer-generated visualizations can be compared with the experimental "smoke-wire" photographs of Saric et al (1984).

The pattern for the combination mode with detuning $\hat{\epsilon} = 0.4$ is presented in figure 3.23 and is the first visualization of such a structure. The streamwise wavelength of the pattern is determined by the ratios of the

wavelength of both detuned modes ($\alpha + \epsilon$), ($\alpha - \epsilon$), and the TS wavelength. For this value of detuning, a mixture of staggered and aligned patterns can be clearly appreciated. However, for modes in the neighborhood of the subharmonic (or fundamental) these streamwise changes in the arrangement require larger distances and may be hard to recognize in the small number of clear Λ-shaped structures. In addition, the arrangement of Λ vortices varies with time.

The stretching of the particles due to secondary instabilities is so large that details of the Λ-shaped structure could be lost, thus producing an almost uniform pattern towards the end of the plate. This almost uniform pattern could be misinterpreted as turbulence. However, the structure is indeed still of a regular nature. The extent of the secondary instability region, therefore, may be considerably larger than indicated by smoke-wire visualizations.

4. THE FREE-SHEAR LAYER

4.1 General Comments

Continuing the program to identify the basic mechanisms of the transition process, we focus our attention on the free-shear layer. This flow occurs, for example, when two streams merge. As mentioned in the introduction, free-shear layers are particularly attractive from the physical and theoretical points of view. For one part, the intense mixing that occurs at the interface is of interest to understand phenomena e.g. in combustors, lasers, and chemical reactions. For the other part, the free-shear layer is an example of inviscidly unstable flows. For simplicity, we consider the hyperbolic-tangent velocity profile as the prototype of free-shear layer flows.

As for the boundary layer, the initial development of the disturbances in the free-shear layer is described satisfactorily by the classical linear stability theory for viscous and inviscid flows. Squire's theorem correctly explains the two-dimensionality of the most unstable primary wave and in the inviscid limit, Rayleigh's theorem predicts large growth rates because of the inflectional character of the velocity profile.

There exists the usual ambiguity in the theory with regard to the temporal or spatial development of the disturbances. The spatial analysis (Michalke 1965, Monkewitz & Huerre 1982) has more physical meaning and is closer related to the experimental observations by Sato (1956), Freymuth (1966), Miksad (1972), and Fiedler et al. (1981). Temporal analysis, on the other hand, is mathematically simpler, because it results in a standard eigenvalue problem. The growth rates of the two concepts are related by Gaster's transformation (Gaster 1962).

One key assumption of the classical analysis is that the basic flow is locally parallel. Unfortunately, this assumption is not well satisfied by the observed mixing layers. Consequently, the linear stability theory has been extended to slowly divergent flows by Crighton & Gaster (1976), Plaschko (1979), and Gaster et al. (1985) for mixing layers. A complex amplitude accounts for the nonparallel effects. Crighton & Gaster (1976) found that the corrections of the amplification rates due to non-parallel effects in an axisymmetric jet were more important than for boundary layers and must be accounted for to achieve agreement with observations. Similar results were obtained by Ragab & Wu (1987) in supersonic mixing layers.

In addition, the experimentally measured velocity profiles deviate slightly from the assumed hyperbolic-tangent shape. In fact, the latter profile is not a solution of the full Navier-Stokes equations, except in the inviscid limit. An artificial forcing term could be introduced to account for the viscous effects. To obtain better agreement with experiments, several polynomial fits based on the tanh$y$ profile have been suggested and used to reduce the discrepancies (e.g. Gaster et al. 1985). Monkewitz & Huerre (1982) employed the more appealing Blasius shear layer as basic flow. In both approaches, significant variations of both eigenvalues and eigenfunctions were found.

Instead of improvements in the theoretical-experimental agreement, we are interested in more fundamental aspects of the transition process, such as the emergence of subharmonic pairing and the appearance of three-dimensional structures. These observed phenomena are evidence of secondary instabilities. Because we ignore much of the complicating effects discussed above, some details are expected to be lost and our results probably compare unsatisfactorily with experiments. However, our model provides a good description of

the overall transition process and is open to future improvements.

4.1.1 Experimental Aspects

Since the early experiments of Sato (1956), the importance of secondary instabilities, in particular of the subharmonic vortex pairing, has been clearly recognized. Winant & Browand (1974) performed careful and detailed experiments on vortex pairing. The observation of three-dimensional structures (braids) by Breidenthal (1981) and Browand & Troutt (1980) had major impact on the common view of a quasi-two-dimensional paths to turbulence. Recent experiments by Bernal & Roshko (1986), Lasheras, Cho & Maxworthy (1986) and Ho & Hang (1982) contributed to a new picture of the three-dimensionality of the transition process.

4.1.2 Theoretical Aspects

From the theoretical point of view, the first attempts to treat the secondary instability problem in mixing layers was made by Kelly (1967). Using a mixture of weakly nonlinear models and Floquet analysis, Kelly was able to reveal the parametric nature of the subharmonic pairing modes for the hyperbolic-tangent velocity profile.

The Floquet analysis was extended by Pierrehumbert & Widnall (1982) to include three-dimensional modes in the stability analysis of a mixing layer modeled by an array of Stuart vortices (Stuart 1967). Pierrehumbert & Widnall's study will be referenced hereafter as P&W's study. P&W found that the two-dimensional subharmonic modes (vortex pairing) are in fact the most unstable modes of secondary instability, but besides these, there is a wide range of unstable three-dimensional subharmonic modes (helical pairing). The

helical pairing may appear in a broad band of spanwise wavenumbers with growth rates almost as large as those of the two-dimensional mode.

Pierrehumbert & Widnall were the first to identify theoretically the fundamental (translative) instability in the free-shear layer. These modes are necessarily three-dimensional. The growth rates assume a maximum at some spanwise wavenumber and decrease only slightly if the wavenumber is further increased.

The results of P&W agree qualitatively with the numerical simulations of the evolution of fundamental modes by Corcos et al. (1984), and Metcalfe et al. (1987).

P&W consider the primary instability of Stuart vortices. However, the transition process in mixing layers can also be viewed as a sequence of instabilities associated with the formation of new flows. Following this latter view, we treat the onset of transition in mixing layers as a secondary instability in a way similar to Herbert's (1984) analysis of channel flow and boundary-layer flows. We consider the change-over from two-dimensional to the three-dimensional stage as a parametric instability of the periodic flow produced by a primary instability wave. We aim at showing the applicability of this model and at testing the validity of the inherent assumptions.

Numerical simulations and stability studies have applied a variety of methods to cope with the infinite extent of the flow domain and the difficulties inherent in the stability problem. While in some cases the problem of the infinite domain has been avoided by truncation at some finite distance from the inflection point or by a periodic arrangement of shear layers in the y direction, the effect of these measures is not clearly documented. Even when

the full domain has been retained, a variety of methods, in particular spectral methods, has been used but the preferences are not based on a thorough comparison. Therefore, we discuss in section 4.2 some aspects of numerical methods used for solving the primary instability problem. The stiffness of the Orr-Sommerfeld equation and the presence of a continuous spectrum of eigensolutions make it necessary to investigate more carefully the numerical method of solution. This study of the primary instability provides the basis to attack the secondary instability problem because the basic equations and numerical problems are in many respects similar.

Certain parts of our study are directly comparable to Pierrehumbert & Widnall's work on the stability of Stuart vortices. Section 4.3 will give a brief account of the main properties of this flow and their resemblance with the properties of our basic flow which is constructed by superposition of TS waves.

In the last section, we discuss results and compare with previous work. We present results for modes of combination resonance, and on the effect of the Reynolds number on the growth rate of primary and secondary instability.

4.2 Numerical Solution for Primary Instability

We have dedicated a great deal of effort to developing an accurate and reliable numerical method of solution. As mentioned in Chapter 2, two spectral collocation methods were used. One is based on Chebyshev polynomials, while the other is based on trigonometric functions. The infinite domain of the flow field is mapped onto the interval [-1,1] by hyperbolic, algebraic, or trigonometric transformation functions. The methods of solution are tested by solving the Orr-Sommerfeld problem.

4.2.1 Principal Eigenvalue

In Table 4.1 we show the convergence characteristics of the imaginary part of the principal temporal eigenvalue c for all combinations of approximating functions and mappings. The results are given for Reynolds number Re =100 and three streamwise wavenumbers, α = 0.25, 0.5, and 0.75. For both types of approximating functions, the mapping parameter varies from 0.5 to 4.0. These parameters coincide with a similar study made by Metcalfe et al. (1987) who also used Chebyshev polynomials and the algebraic and hyperbolic mappings.

We seek the best compromise between two conflicting goals when choosing the approximating functions and the mappings. First, we aim at accurate solutions employing a relatively small number of approximating functions. Second, we seek solutions that depend only weakly on the mapping parameter η_0. Although ideally the results should be independent of η_0, some dependence is unavoidable. The best we can require is that η_0 does not need to be fine tuned to the parameter range and that we can rely on the solution for a wide range of Reynolds numbers and wavenumbers. We found that the overall best results are obtained with Chebyshev polynomials in combination with the algebraic mapping. This conclusion is shared by Metcalfe et al. (1987). The two other mappings considered have acceptable numerical characteristics when used with Chebyshev polynomials. On the other hand, only the trigonometric mapping is worth considering when Fourier series are used. With only a small number of expansion functions, Fourier series generally are more accurate and converge faster to the correct eigenvalue than Chebyshev series with the same number of polynomials. However, with large numbers of functions, the Fourier series converge considerably slower. This result can be

explained by the deteriorating condition of the algebraic system for the Fourier coefficients. Consequently, most of our solutions were obtained using Chebyshev polynomials and the algebraic mapping with $\eta_0 = 1.0$ and 2.0. Many results were cross-checked with solutions employing Fourier series and the trigonometric mapping with $\eta_0 = 2.0$.

The convergence characteristics should be maintained for a wide range of wavenumbers. Figures 4.1 and 4.2 show the variation of the temporal eigenvalue with the spanwise wavenumber β obtained by using Chebyshev polynomials and the algebraic mapping for $Re = 200$ and the streamwise wavenumber $\alpha = 0.5$. Accurate solutions are obtained with $\eta_0 = 1$ and 2, and 17 collocation points. Solutions with $\eta_0 = 4.0$ are very poor for all values of β. Moreover, while solutions with $\eta_0 = 0.5$ are acceptable for intermediate values, they are deficient in the neighborhood of $\beta = 0$ and 0.8. If we increase the number of polynomials, the agreement between solutions improves for all values of η_0, as can be seen in Figure 4.2 for 32 collocation points. This solution, of course, coincides with that previously obtained with $\eta_0 = 1.0$ or 2.0 and 17 collocation points.

As we increase Re to approach the inviscid limit, the Orr-Sommerfeld equation becomes stiffer and more difficult to solve. In fact, solutions using 17 polynomials become unreliable, especially in the neighborhood of the neutral value (zero growth rate), as shown in figure 4.3. Moreover, solutions with as many as 32 polynomials may not be accurate enough for some values of η_0, as can be seen in figure 4.4. Further increasing the number of polynomials as in figure 4.5 with 64 improves the convergence of the solution.

Figure 4.6 shows the principal temporal eigenvalue as a function of the spanwise wavenumber an compares various of our solutions with results of previous work by Michalke (1965). We obtained solutions by directly solving the three-dimensional primary instability problem, by reducing to an equivalent two-dimensional case using the Squire's transformation, and by solving the secondary instability problem in the limit $A \rightarrow 0$. Solutions for the first three cases coincide for all wavenumbers. However, near marginal stability, solutions using the secondary instability equations in the limit of vanishing amplitude are inaccurate due to the singular behavior of solutions to the Rayleigh equation. If viscosity is introduced, the secondary instability limit will reproduce exactly the primary instability solution, and all curves collapse as in figure 4.7. Similar results can be obtained using trigonometric functions.

For the Rayleigh equation (in our notation), the maximum amplification rate $\sigma_i = 0.1896$ corresponds to the wavenumber $k = k_m = 0.4446$ where $k^2 = \alpha^2 + \beta^2$. Marginal stability is obtained for $k = 1.0$. The wavenumber $\alpha = k = 0.5$ of the TS wave in our basic flow is slightly larger than k_m. In the figures for the three-dimensional primary waves with $\alpha = 0.5$ and $\beta > 0$, instability occurs for values of β which lead to $0.5 < k < 1$. Neutral stability, $k = 1.0$, corresponds to $\beta = \frac{\sqrt{3}}{2}$ in agreement with the results shown.

When making comparisons with other researchers like Michalke and P&W, who use a slightly different form of the basic flow, some basic relations are useful. The eigenvalue c corresponding to a basic flow $U = U(y)$ for a wavenumber α and Reynolds number Re, is the same as the eigenvalue of $U = U(bz)$ for wave number $\hat{\alpha} = b\,\alpha$ and Reynolds number $\overline{Re} = Re\ b$. Similarly, if one considers the basic flow of the form $U(y) = b\,(U(z) + a)$,

the eigenvalue $\hat{c}$ is related to the original by $\hat{c} = (a + c)b$.

4.2.2 Numerical Spectrum

One of the advantages of spectral methods is the relative easy of obtaining and investigating the behavior of eigenvalues different from the principal one. In this way, the spectral method can provide more physical insight into the problem. Figures 4.8 to 4.18 show a complex plane with the real and imaginary parts of the temporal eigenvalues σ which we obtain from the discretized version of the primary instability problem (Rayleigh equation). In some figures, parts of the left plane have been omitted because of the symmetry of the spectrum about the imaginary axis. In the inviscid case, there exists for each eigenvalue (σ_r, σ_i) a corresponding eigenvalue $(-\sigma_r, \sigma_i)$.

Close examination of the spectrum of the Rayleigh equation as shown in figure 4.8 reveals that the most unstable (principal) eigenvalue is real. Moreover, there is a corresponding damped eigenvalue. In addition, all the remaining eigenvalues are purely imaginary (neutrally stable). This family of eigenvalue constitutes the discrete representation of the continuous spectrum of eigenvalues that characterizes unbounded flows. Our results are consistent with some well known properties of the Rayleigh equation (Lin 1955). If σ is an eigenvalue, then its complex conjugate is also an eigenvalue. Therefore, as we have formulated the problem here, only unstable and neutral solutions are possible. For each damped solution, we will always obtained a corresponding growing solution. This paradox can be removed by including viscosity or by allowing discontinuous solutions (Lin 1955). Here, we are interested in unstable solutions, and this point will not be discussed further.

In the analysis of the inviscid limit of the Orr-Sommerfeld equation, certain aspects deserve attention. First of all, the spectrum of eigenvalues coincides exactly with the result of the Rayleigh equation, as can be deduced from figures 4.8 and 4.9. The tendency of the eigenvalues of the Orr-Sommerfeld equation for large Re towards the eigenvalues of the Rayleigh equation is obvious. For $\alpha \leq 1$, we find one-to-one correspondence for the growing, the damped, and the "continuous" eigenvalues. For finite Re, the latter are located in the stable domain. For the other part, the Rayleigh equation is singular at $y = 0$. Consequently, the selection of $y = 0$ as a collocation point should be avoided. This requirement is violated when using an odd number of Chebyshev polynomials. The inappropriate selection of collocation points results in the occurrence of an eigenvalue close to the origin as shown in figure 4.10 for 33 collocation points. The resultant algebraic system is ill-conditioned and numerically not well-behaved. Using a similar but even number of collocation points does not suffer from this eigenvalue as shown in figures 4.9 with 32 points.

Our numerical method replaces the differential equation by an algebraic system which provides a set of discrete eigenvalues. The number of eigenvalues is equal to the dimension of the algebraic system. After separating out the discrete eigenvalues of the differential problem, we are left with a finite set of eigenvalues which approximate the continuous spectrum of the differential equation. The properties of the continuous spectrum for the free-shear layer have virtually not yet been studied. The numerical results for the Rayleigh equation suggest that the continuous spectrum aligns along the imaginary axis with phase velocities $-1 \leq c_r \leq 1$, i. e. between minimum and maximum velocity of the mean flow. For the viscous problem, the phase velocity of the

continuous modes seems to be in the same range. The results suggest that for $\alpha = 0.5$ two branches start at $\sigma = \pm 0.5$ ($c_r = \pm 1$) toward some point on the negative real axis and asymptotically approach this axis, $c_r \rightarrow 0$. Such approach of the phase velocity of highly damped continuous modes to the mean velocity would be consistent with the results for the boundary-layer case.

Physically, the continuous spectrum lacks importance because the instability of the flow is governed by the discrete principal eigenvalue. However, the numerical approximation to the continuous spectrum can affect the accuracy of results especially near neutrally stable conditions due to the proximity to the principal eigenvalue as seen in figure 4.11. This influence is apparent in slow rates of convergence when iteratively solving the eigenvalue problem.

The distribution of the discrete eigenvalues associated with the continuous spectrum varies greatly with the mapping and expansion functions used. High values of η_0, as in figure 4.12, tend to accumulate these eigenvalues near $\sigma = (0.5,0)$ while low values of η_0 give a more uniform spacing along the imaginary axis, as in figure 4.13.

The stabilizing effect of viscosity in the mixing layer is beneficial to the numerical convergence. For finite Re, the marginally stable continuous spectrum moves to the left into the stable region and away from the origin. For the numerical analysis, this means that the resultant matrix is better conditioned. Odd numbers of polynomials can be used without loss of accuracy. Figures 4.9, 4.14 and 4.15 show how the discrete representation of the continuos spectrum moves deeper into the stable domain as Re decreases. The effect of the mapping parameter in the representation of the continuous spectrum is shown in figures 4.16 and 4.17

Although most of the discussion in the preceding paragraphs has been based on the spectral method based on Chebyshev polynomials and algebraic mapping, the conclusions for methods based on Fourier series and exponential and trigonometric methods are similar. Figures 4.18 and 4.19 are samples of spectra using Fourier series and trigonometric mappings for the solution of the Rayleigh equation and the Orr-Sommerfeld for $Re = 200$. The principal eigenvalue is accurately represented and the characteristics of the approximation to the continuous spectrum are similar to those discussed above.

4.3 The Stuart Vortices

Because we aim at a comparison with Pierrehumbert & Widnall's work for Stuart vortices as basic flow, it is necessary to review some basic properties of this flow. Most of this section is based on Stuart's original derivations (Stuart 1967).

4.3.1 Derivation

As shown previously in Chapter 2, the vorticity transport equation of a two-dimensional inviscid flow in terms of the streamfunction is given by

$$\frac{\partial}{\partial t}\nabla^2\psi + \frac{\partial\psi}{\partial y}\frac{\partial}{\partial x}\nabla^2\psi - \frac{\partial\psi}{\partial x}\frac{\partial}{\partial y}\nabla^2\psi = 0. \qquad (4\text{-}1)$$

If we consider two-dimensional motions in a Galilean frame moving with the velocity of the inflection point, the vorticity equation reduces to

$$\frac{\partial\psi}{\partial y}\frac{\partial}{\partial x}\nabla^2\psi - \frac{\partial\psi}{\partial x}\frac{\partial}{\partial y}\nabla^2\psi = 0. \qquad (4\text{-}2)$$

The general solution of equation (4-2) has the form

$$\nabla^2\psi = f(\psi) \qquad (4\text{-}3)$$

for any arbitrary function f. In particular, the streamfunction of the hyperbolic-tangent profile

$$\psi = \ln(\cosh y) \tag{4-4}$$

satisfies the Liouville equation

$$\nabla^2\psi = Be^{-2\psi}. \tag{4-5}$$

The general solution of equation (4-5) can be expressed in the form

$$\psi = C\ln(\cosh y - \rho\cos x) \tag{4-6}$$

where $B = 1 - \rho^2$. This form of the solution has been used by P&W and is equivalent to the original expression given by Stuart.

Without loss of generality, we choose $C = 1$ and discuss in the following some interesting properties of the flow with the streamfunction

$$\psi = \ln(\cosh y - \rho\cos x) \tag{4-7}$$

4.3.2 Relation with Other Flows

A close examination of the streamfunction reveals interesting connections with more classical flows. The limit $\rho \to 0$ reduces equation (4-7) to the hyperbolic-tangent profile streamfunction

$$\psi = \ln(\cosh y). \tag{4-8}$$

As the other extreme, the streamfunction in the limit $\rho \to 1$ is

$$\psi = \ln(\cosh y - \cos x), \tag{4-9}$$

which represents the flow produced by an infinite set of equally spaced point vortices (Lamb 1932).

The streamfunction can alternatively be written as:

$$\psi = \ln\cosh y + \ln\left[1 - \frac{\rho\cos x}{\cosh y}\right]. \tag{4-10}$$

The expression

$$\frac{\rho\cos x}{\cosh y} \tag{4-11}$$

is always less than one since

$$\rho < 1, \quad \cos x \leq 1 \quad \text{and} \quad \cosh y > 1. \tag{4-12}$$

Expanding in a Taylor series in terms of (4-11), we obtain

$$\psi = \ln\cosh y - \frac{\rho\cos x}{\cosh y} + O(\rho^2) \tag{4-13}$$

To within terms of $O(\rho^2)$, this streamfunction coincides with the neutral solution of the Rayleigh equation for the hyperbolic-tangent velocity profile. The corresponding neutral wavenumber is $\alpha = 1$ and the eigenfunction $\mathrm{sech} y$. The parameter ρ plays the role of an amplitude. This expansion is valid even for the relatively large values of ρ used by P&W.

The streamwise variable x is moving in a Galilean frame. The total streamwise velocity u can thus be expressed as:

$$u = \bar{u} + \tilde{u} \tag{4-14}$$

where the mean velocity $\bar{u}$ is given by

$$\bar{u} = \int_0^{2\pi} \frac{\sinh y\, dx}{\cosh y - \rho\cos x} \tag{4-15}$$

$$\bar{u} = \tanh y \left[\frac{\sinh y}{(\cosh y - \rho\cos x)^{\frac{1}{2}}}\right] \tag{4-16}$$

and the fluctuation velocity $\tilde{u}$ is

$$\tilde{u} = \tanh y \left[\frac{1}{1 - \hat{\delta}\cos x} \right] \tag{4-17}$$

where $\hat{\delta} = \dfrac{\rho}{\cosh y}$

Using this form we can calculate the rms of the disturbances according to

$$\text{rms}(u) = < \tilde{u}^2 > \tag{4-18}$$

where the symbol $< f >$ denotes the average value of f. Upon integration, (4-18) yields

$$\text{rms}(u) = \tanh \frac{y}{(1 - \hat{\delta}^2)^{\frac{3}{4}}} \left[1 - (1 - \hat{\delta}^2)^{1/2} \right]^{\frac{1}{2}} \tag{4-19}$$

The rms of the velocity fluctuation can be easily measured in experiments and is therefore a convenient representation of the disturbance velocity. Figure 4.20 shows the maximum rms value A and its y-location as a function of the amplitude parameter ρ. The location of the maximum is almost constant, and the rms varies almost linearly with ρ.

The rms-velocity distribution for Stuart vortices in the normal direction deviates insignificantly from the distribution of the neutral TS wave even for the relatively high values of $\rho = 0.25$. Since the most important quantities in the hydrodynamic stability analysis of shear flows are the vorticity gradients, we show in figures 4.21 and 4.22 contour lines of constant vorticity. The iso-vorticity contours in Figure 4.21 are for Stuart vortices with $\rho = 0.10$ and the corresponding plot for a neutral TS wave with A = 0.035 is shown in figure 4.22. The similarity between both figures is evident. However, the vorticity for Stuart vortices is slightly more concentrated than the distribution for the

neutral TS wave.

4.3.3 The Vorticity Field

The total vorticity ς can be expressed in terms of its mean $\bar{\varsigma}$ and fluctuating component $\tilde{\varsigma}$. The mean vorticity is given by

$$\bar{\varsigma} = \frac{\rho^2 - 1}{\cosh^2 y \ (1 - \hat{\delta}^2)^{\frac{3}{2}}} \tag{4-20}$$

and the rms of the vorticity by

$$\text{rms}(\varsigma) = \frac{\rho^2 - 1}{\cosh^2 y} \left\{ \frac{1}{8 \ (1 - \hat{\delta})^3 \ (1 - \hat{\delta}^2)^{\frac{1}{2}}} \right. \tag{4-21}$$

$$\left[\frac{5}{2} + \frac{3}{2} \left(\frac{1 - \hat{\delta}}{1 + \hat{\delta}} \right) + \frac{3}{2} \left(\frac{1 - \hat{\delta}}{1 + \hat{\delta}} \right)^2 + \frac{5}{2} \left(\frac{1 - \hat{\delta}}{1 + \hat{\delta}} \right)^3 \right]$$

$$\left. - \frac{1}{(1 - \hat{\delta}^2)^3} \right\}^{\frac{1}{2}}$$

This rms distribution of vorticity in the normal direction is shown in figure 4.23 for a value of ρ of 0.10.

4.4 Secondary Instability Modes

4.4.1 Numerical Spectrum

Typical numerical spectra of secondary instability modes are presented in figure 4.24, 4.25 and 4.26. The Reynolds number is $Re = 5000$ which is sufficiently large to approximate the inviscid solution. The rms velocity amplitude $A = 0.0355$ corresponds to the amplitude parameter $\rho = 0.10$. The streamwise wavenumber $\alpha = 1.0$ corresponds to the neutral TS wave. Results are shown using Chebyshev polynomials with the algebraic mapping and 32 collocation points. Figures 4.24 and 4.25 show the spectra for the two dimensional subharmonic mode and the fundamental mode with spanwise wavenumber $\beta = 2$, respectively. In both figures, we can appreciate the (insignificantly disturbed) symmetry with respect to the real axis since complex modes occurring the inviscid limit as conjugate pairs. Like in the primary instability problem, there exists a damped mode for each growing mode. This property also holds for detuned modes. The alignment of some eigenvalues suggests the existence of a continuous spectrum in the secondary instability problem.

Similar results for the Reynolds number $Re = 200$ are shown in figures 4.27, 4.28, and 4.29 for the subharmonic, the fundamental, and combination modes respectively. The damping effect of the viscosity affects all modes and the continuous spectrum moves toward the stable region, like in the case of primary instability.

4.4.2 Comparison with Pierrehumbert & Widnall

As we discussed in Section (4.3), our secondary instability analysis on neutral TS waves is similar to the stability analysis of Stuart's vortices by Pierrehumbert & Widnall's (1982). The main differences are the selection of the basic flow and the accuracy of the numerical method used.

Using results from Section (4.2), disagreements in the basic flow due to the use of a slightly different normalization of amplitudes have been removed. Correspondence between amplitude parameters has been achieved by matching the rms amplitudes of the neutral TS wave and the Stuart vortices. The values corresponding to the amplitude parameters $\rho = 0.10$ and $\rho = 0.25$ used by P&W are $A = 0.0355$ and $A = 0.0915$.

From the numerical point of view, there are differences in the selection of domain of the solution, in the mapping from the physical space to the solution space, and in the number of approximating polynomials used in the streamwise and normal directions.

Pierrehumbert & Widnall used 7 Chebyshev polynomials in the truncated finite domain $| y | \leq d$. This physical domain is transformed to $| Y | \leq 1$ by the mapping

$$y = d \frac{\tanh^{-1}(\lambda Y)}{\tanh^{-1}(\lambda)}.$$

They found that the best results were obtained when the mapping parameters d and λ were 1.5 and 0.95 respectively. In the streamwise direction, they expressed the solution by a five modes Fourier series.

On the other hand, we have worked in an infinite domain in y, using both Chebyshev and Fourier series. We have checked the accuracy of the

solution by using up to 65 modes and three different transformations as discussed previously. In the streamwise direction, we have also used five Fourier modes.

4.4.2.1 Subharmonic Modes As figure 4.30 shows, the most unstable subharmonic mode for all TS wave amplitudes is invariably two-dimensional ($\beta = 0$) and corresponds to vortex pairing. However, unstable modes also exists for $\beta > 0$. These modes are usually called helical pairing since pairings occur locally along the span. Chandrsuda (1978) and Browand & Troutt (1980) have confirmed the existence of these modes in experiments. Subharmonic instability is of broadband nature and shows weak spanwise selectivity. In addition, this subharmonic instability exist only for long spanwise waves since modes with $\beta > 2$ are stable for all TS amplitudes.

As ρ (or equivalently A) increases, the short-wave cutoff first increases and then decreases. This cutoff may be due to two effects as Pierrehumbert & Widnall explain: *Increasing ρ produces a thin flat vortex structure which acts somewhat like a thinner shear layer than the original one, and can support smaller scale instabilities. As ρ increases the vorticity is concentrated in a compact core, and the effects of selfinduced vortex tube rotation begin to become important.*

Our results basically confirm P&W's results. The small quantitative differences can be attributed to the use of a slightly different basic flow and to the low truncation. Their results may lack accuracy. One way to check truncation effects on the numerical accuracy of the results is to investigate the limit $\rho \rightarrow 0$. This limit reduces the secondary instability problem to the classical instability of the hyperbolic-tangent velocity profile with wavenumber

$\alpha = 0.5$. As discussed in a preceding section, our results agree with respect to the maximum growth rate $\sigma = 0.1896$ and the neutral instability at $\beta = \frac{\sqrt{3}}{2}$. As shown in figure 4.30, P&W's results for the growth rates at $\rho = 0$ are slightly below the correct values. and our secondary instability results. As can be seen in figure 4.30, this shift is also observed for nonzero values of ρ. This suggests a systematic "numerical stabilization" in their results.

Apart from these small numerical variations, we confirm the main results of P&W. Namely, the broadband nature of the subharmonic instability with respect to the spanwise wave number, the increase of the two-dimensional growth rates with increasing amplitude, and the decrease of the unstable region for amplitudes beyond some threshold value.

4.4.2.2 Fundamental Modes Fundamental modes are characterized by the presence of counterrotating streamwise vortices or "ribs" that develop into the braids between the two-dimensional vortex cores. These modes are responsible for the generation of the mushroom-shaped features seen in visualizations in the plane normal to the mean flow direction. These features have been studied experimentally by Breidenthal (1981) and Bernal (1981), and in numerical simulations by Metcalfe et al. (1987) and Corcos et al. (1984). Pierrehumbert & Widnall named these fundamental modes translative modes since they represent infinitesimal translations of a vortex row at a fixed spanwise position. This notation should not be understood as indicating a two-dimensional phenomenon.

Our results for fundamental modes are presented in figure 4.31. Unlike the subharmonic mode, the most unstable fundamental mode is three-

dimensional. Fundamental instability is characterized by maximum growth rates at relatively large spanwise wavenumbers. This property is in contrast with TS waves that are unstable only for $\alpha^2 + \beta^2 < 1$, as well as with subharmonic modes that also show a cut-off towards larger wavenumbers.

In the limit $A \rightarrow 0$, the fundamental modes are analytically connected with Rayleigh or Orr-Sommerfeld modes. For P&W's parameters, the limit $A \rightarrow 0$ reduces the secondary instability to the neutral point of primary instability at $k = 1$. Therefore, the growth rates for all spanwise wavenumbers are zero in the limit $A \rightarrow 0$. As A increases, unstable modes with convective growth rates appear. At larger amplitudes, the maximum growth rate is of the same order as that for the two-dimensional pairing and occurs at wavenumbers of $O(1)$.

Spanwise wavelengths of unstable fundamental modes are shorter than those of three-dimensional subharmonic modes. Moreover, the growth rates for a wide range of spanwise wavenumbers is almost constant and close to the maximum value. This variation of the growth rates with the spanwise wavenumber for short wavelengths implies that a large range of spatial scales can be simultaneously excited and the spanwise wavenumber selection is extremely weak.

From our comparison with Pierrehumbert & Widnall's results, we notice that their analysis underpredicts the growth rates, but in general, we share their conclusions.

4.4.3 Detuned Modes

In addition to fundamental and subharmonic modes of secondary instability, detuned modes can also be excited in free-shear layers. However, there is yet no direct experimental or theoretical evidence for these modes available. Much of what we discussed in boundary layers can also be said about shear layers. Combination modes can be easily excited and will be responsible for a broadband frequency response under "natural" conditions.

Figure 4.32 shows the variation of growth rates with the spanwise wavenumber β for neutral TS waves ($\alpha = 1$) and detunings $\epsilon = 1$ (subharmonic), 0.8, 0.5 and 0 (fundamental). The value of $Re = 5000$ is considered large enough to provide a good approximation to the inviscid solution. The rms amplitude $A = 0.091$ is relatively high but consistent with observations. When $\epsilon = 0.8$, the most amplified eigenvalue is two-dimensional like in the subharmonic case. However, when $\epsilon = 0.5$ the most unstable mode is three-dimensional with $\beta \approx 1$ like in the fundamental case. In addition, the detuned modes with $\epsilon = 0.8$ and 0.5 have a broad spanwise spectrum and are unstable for both long and short wavelengths.

The streamwise broadband nature of the secondary instability of mixing layers is evident in figure 4.33. where the variation of the temporal growth rate with the detuning is shown for the spanwise wavenumbers $\beta = 0.1$ and 1. The former wavenumber is close to the two-dimensional case. Modes in the proximity of the subharmonic are the most unstable. On the other hand, when $\beta = 1$, the most unstable modes are in the neighborhood of the fundamental.

4.4.4 Influence of Reynolds Number

Figures 4.34 and 4.35 show the variation of the growth rates with the spanwise wavenumber β for several Reynolds numbers. The rms-amplitude of the neutral TS waves is 0.0355. The stabilizing effect of viscosity can be seen as growth rates decrease with decreasing Reynolds number for all spanwise wavenumbers for both the subharmonic mode in figure 4.34 and the fundamental mode in figure 4.35.

Figures 4.34 and 4.35 show that as Re increases, the growth rate σ at fixed β approaches a finite limit. At finite Re, the general characteristics of the inviscid secondary instability are retained. The viscous effects are always stabilizing and do not change the preference for two-dimensional subharmonic instability.

Although at smaller amplitudes and spanwise wavenumbers, the inviscid limit seems to be reached for $Re = 5000$. small viscous effects are still present for this Reynolds number at large spanwise wavenumbers. From the numerical point of view it is desirable to maintain the viscosity since it improves the convergence and can lead to substantial savings in computational resources.

Although figures 4-34 and 4-35 are only for one rms-amplitude $A = 0.0355$, very similar conclusions are valid for all amplitude levels. For instance, results for the subharmonic mode shown in figure 4.36 for $Re = 200$ and several amplitude levels, can be directly compared with figure 4.30.

4.4.5 Influence of the TS Amplitude

Variation of growth rates of the subharmonic mode with the spanwise wavenumber as a parameter are plotted in figure 4.37. The limit of the amplitude $A \rightarrow 0$ reproduces the corresponding primary instability growth rates with half wavenumber ($\alpha = 0.5$). For the two-dimensional subharmonic mode ($\beta = 0$) in an inviscid flow, σ would approach the asymptotic value $\sigma_r = 0.25$ which corresponds to Lamb's instability of a row of point vortices. Here, this limit is not approached for large amplitudes, due to the small viscosity introduced. The long-wave characteristics of the subharmonic instability discussed before are also displayed here. For increasing wavenumbers growth rates reach the maximum at lower levels and the cut-off wave number is smaller. The drop in levels of growth rates for $\beta = 1$ is quite dramatic.

Similar results for the same parameters are shown in figure 4.38 for the fundamental mode. Fundamental modes are neutrally stable in the two-dimensional limit. Growth rates increase monotonically with the TS amplitude for all wavenumbers. Maximum values of growth rates are reached for β in the proximity of 1 and decrease slowly as β increases.

4.4.6 Comparison with Metcalfe

Numerical simulation of the temporal evolution of the hyperbolic-tangent velocity profile have been made by Metcalfe et al. (1987) and others. They studied mainly interactions among TS waves, two-dimensional subharmonic and three-dimensional fundamental modes. The wavenumber of the TS wave they choose is close to the most unstable wavenumber. Therefore, the TS wave exhibits strong growth while only moderate growth occurs at the subharmonic wavenumber.

Figure 4.39 compares the variation of the growth rates for the subharmonic mode over the spanwise wavenumber for a TS wave with $\alpha = 0.4$ and $A = 0.177$ (which corresponds to 0.25 in Metcalfe's notation). To show effects of viscosity, we present results for Reynolds numbers $Re = 200$, 400, 800 and 1600. There are no comparable values given by Metcalfe et al. Owing to the smaller α, the unstable range of spanwise wavenumbers increases in comparison with the case of a neutral TS wave. The curves for all Re are very similar that viscosity effects in this case are less significant. In the limit $A \rightarrow 0$, the growth rates of the subharmonic modes are connected to the Orr-Sommerfeld mode with half the streamwise wavenumber $\alpha = 0.2$.

Figure 4.40 shows growth rates of fundamental modes for the same values of Re and TS amplitude. These growth rates can be directly compared with Metcalfe et al. (1987). In general, our growth rates for all spanwise wavenumbers and all Re are smaller. Similarly, the cut-off wavenumber is always smaller. There are also qualitative inconsistences at small β, where their results show decreasing growth rates while ours show increasing values. For $\beta \rightarrow 0$ the growth rates are slightly higher than TS rates, revealing expected connections with Orr-Sommerfeld modes.

The differences between the growth rates of our calculations and the numerical simulations may suggest that the growth of the TS wave has a significant effect. In the secondary instability theory formulated in Chapter 2, such growth of the TS has been neglected and an equilibrium state has been assumed. To check this suggestion, we have developed a method to account for variations in the TS wave amplitude.

4.4.7 Account for Variation in TS amplitude

One of the approximations of our secondary instability theory is neglecting the growth of the TS wave. In Poiseuille and boundary-layer flow, this assumption is justified since the secondary instability growth rates are typically one order of magnitude higher than primary instability growth rates. However, in shear layers they may be of the same order of magnitude and may not be neglected. This fact is especially true for waves near the most amplified one ($\alpha = 0.4446$). We have developed a method to account for weak variations of the TS amplitude.

The secondary instability equations (2-34) and (2-35) can be written in the form:

$$\mathbf{L}(\mathbf{u}) + A\,\mathbf{M}(\mathbf{u}) = 0 \tag{4-22}$$

where

$$\mathbf{u} = \begin{bmatrix} u_n \\ v_n \end{bmatrix} \tag{4-23}$$

$$\mathbf{L} = \begin{bmatrix} L_n & M_n \\ 0 & Q_n \end{bmatrix} \tag{4-24}$$

and

$$\mathbf{M} = \begin{bmatrix} \sum_l N_{l,n-l} & \sum_l R_{l,n-l} \\ \sum_l P_{l,n-l} & \sum_l S_{l,n-l} \end{bmatrix}. \tag{4-25}$$

In previous analysis, the amplitude of the primary wave A has been taken as a parameter independent of time. Here, we will assume a weak time dependence and decompose the amplitude as follows:

$$A = A_0 + A_1, \tag{4-26}$$

where $A_1 \ll A_0$, and A_0 is assumed to be constant, and A_1 represents the weak variation in amplitude.

The operator **L** can be written as

$$\mathbf{L} = \mathbf{N} + \frac{\partial}{\partial t}\mathbf{P}. \tag{4-27}$$

In this way, the time variation is isolated to the second part of equation (4-27). The problem can then be written as

$$\mathbf{N(u)} + \mathbf{P}\frac{\partial}{\partial t}\mathbf{u} + A_0\mathbf{M(u)} + A_1\mathbf{M(u)} = 0 \tag{4-28}$$

To solve this problem, we use a semi-implicit finite-differences method similar to the one used by Li (1986) to attack nonlinear aspects of the Taylor problem. We use an implicit method to handle the operators

$$\mathbf{N(u)} \text{ and } A_0\,\mathbf{M(u)}, \tag{4-29}$$

and an explicit method for the variation in amplitude

$$A_1\,\mathbf{M(u)}. \tag{4-30}$$

The time discretization can be expressed as:

$$\mathbf{P}\frac{1}{\Delta t}[\mathbf{u}(t_i + \Delta t) - \mathbf{u}(t_i)] =$$

$$-\frac{1}{2}[\mathbf{N} + A_0\mathbf{M}][\mathbf{u}(t_i + \Delta t) + \mathbf{u}(t_i)] - A_1\mathbf{M}(\mathbf{u}(t_i)). \tag{4-31}$$

Rearranging terms, equation (4-31) can be written as

$$\mathbf{u}(t_i + \Delta T) = \tag{4-32}$$

$$(\mathbf{P} + \frac{\Delta t}{2}(\mathbf{N} + A_0\mathbf{M}))^{-1}(\mathbf{P} - \frac{\Delta t}{2}(\mathbf{N} + A_0\,\mathbf{M}))\mathbf{u}(t_i) - \Delta t A_1\,\mathbf{M}(t_i))$$

This formula is equivalent to the implicit trapezoidal method and is $O(\Delta t)^3$ accurate for all terms except the last one which represents the variation in TS wave amplitude. The numerical stability and accuracy characteristics of this method are excellent.

As a first approximation, we assume the variation on the TS wave amplitude to be given by the linear primary instability results, i.e, in the form

$$A = A_0 e^{\sigma_{p_r} t} \tag{4-33}$$

where σ_{p_r} is the linear growth rate of the TS wave. In our notation, A_1 is

$$A_1 = [e^{\sigma_{p_r} t} - 1] A_0. \tag{4-34}$$

This form is realistic for times such that $e^{\sigma_{p_r} t} << 1$. Therefore, it is useful for analyzing tendencies at short times. The unbounded characteristics of the form assumed for the variation in amplitude make it invalid for long times since experimental and theoretical results show the existence of equilibrium amplitudes. Therefore, considering nonlinear effects in the primary wave is necessary to realistically model the TS evolution. Moreover, nonlinear self-interactions of the secondary instability waves and nonlinear interactions between primary and secondary modes may be significant. We plan to study this effect in the future.

The disturbance velocity profiles at the initial time are found by ignoring the TS amplitude variation and by solving the secondary instability eigenvalue problem as before.

To check the accuracy of the method of solution we have solved equation (4-32) for subharmonic modes ignoring amplitude variations. i.e, $A_1 = 0$. Results are shown in Figure 4.41 for the streamwise wavenumber $\alpha = 0.4$, i.e.

near to the most amplified TS wave. Secondary instability growth rate of $\sigma_r = 0.157$ is in excellent agreement with the previous result obtained by solving the eigenvalue problem.

Figure 4.42 shows the time evolution of the amplitude of the subharmonic mode when the primary wave has a growth rate of $\sigma_{p_r} = 0.14$ The initial subharmonic growth rates are similar to that obtained by solving the eigenvalue problem. For longer times, growth rates are slightly lower, but the variation is not significant.

Figure 4.43 shows similar results for the fundamental with spanwise wavenumber of $\beta = 1.0$ for $Re = 1600$. Growth rates, although a little lager, stay at the levels of $\sigma_r = 0.1375$, that is obtained ignoring the amplitude growth.

According to our results, the discrepancies with Metcalfe's computation is not caused by neglecting the growth of the TS wave.

5. SUMMARY AND CONCLUSIONS

We have investigate some aspects of the secondary instability of wall-bounded and unbounded shear flows. We have extended the theory to analyze secondary instabilities proposed by Herbert in two aspects. We generalized the Floquet analysis to include detuned modes and we developed a method to account for non-constant amplitude TS waves. We also worked extensively in developing a reliable spectral method for unbounded domains.

Our main concern in wall bounded flows, represented by the Blasius boundary layer, was to study in detail detuned modes that manifest themselves as combination resonance in the experiments. Results reveal the weak selectivity of the secondary instability with respect to three-dimensional disturbances in the streamwise direction. Previous studies (Herbert, Spalart) had shown that the selectivity is also weak in the spanwise direction. Secondary instabilities and, in a broader sense, transition depend strongly on the spectral distribution of the background and the control exerted. Therefore, research on the spectral properties of the background noise in 'natural' environments and careful documentation of conditions in test facilities is of great importance. Receptivity studies should be given high priority in transition research.

In experimental facilities where some kind of control is present, a preferred route to transition can be observed clearly. Although these experiments may present a narrow picture of the transition process, they play an important role in identifying biases and nonlinear effects.

In the mixing-layer case we were interested in relating the secondary instability theory as formulated by Herbert and the studies of Pierrehumbert & Widnall (P&W) on instabilities of Stuart vortices. In this way, the instabilities

studied by them can be explained in the more general frame work of a cascade of instabilities leading towards turbulence. Equivalence of our studies and P&W's is achieved when we consider instabilities of neutral and inviscid TS waves. We obtained acceptable agreement with their results.

We extended the picture of transition presented by P&W by inclusion of detuned modes. These modes can be preferentially two-dimensional as in the subharmonic case of vortex pairing or three-dimensional as in the fundamental case, according to the detuning value.

All secondary instability modes may evolve with very strong growth rates. In fact, their growth rates are comparable to the maximum primary instability growth rates. This suggest that secondary instabilities in mixing layers are convective and of inviscid nature. We have analyzed the effect of finite Reynolds number on the secondary instability. It is not surprising to find that viscosity plays an always stabilizing role.

As in the boundary layer case, the observed path to turbulence is closely linked to the modal distribution of the external environment. The response will have broadband characteristics in both streamwise and spanwise directions under uniform initial conditions.

We have also investigated secondary instabilities for TS wavenumbers close to the most amplified by the primary instability mechanism. Our aim, in this case was to compare with numerical simulations of Metcalfe et al. The agreement is rather unsatisfactory, although the same general tendencies are displayed. We found that under these conditions the most unstable subharmonic mode is also two-dimensional and that the most unstable fundamental is three-dimensional.

In an attempt to obtain better agreement with Metcalfe et al., we extended the theory to account for weak variations of the TS amplitude. However, the discrepancy was not removed. The reasons must be sought elsewhere.

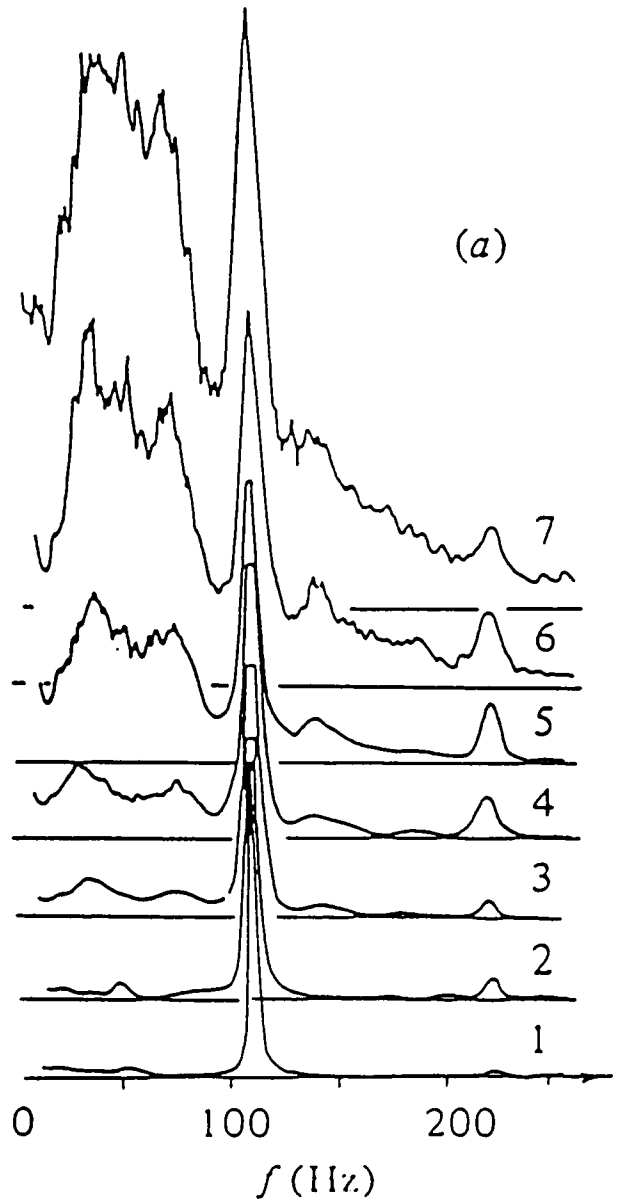

FIGURE 3.1 Streamwise evolution of spectra of fluctuations for x = 300 (1), 480 (2), 600 (3), 640 (4), 680 (5), 720 (6) and 760 mm (7). F=124. (Kachanov and Levchenko (1984)).

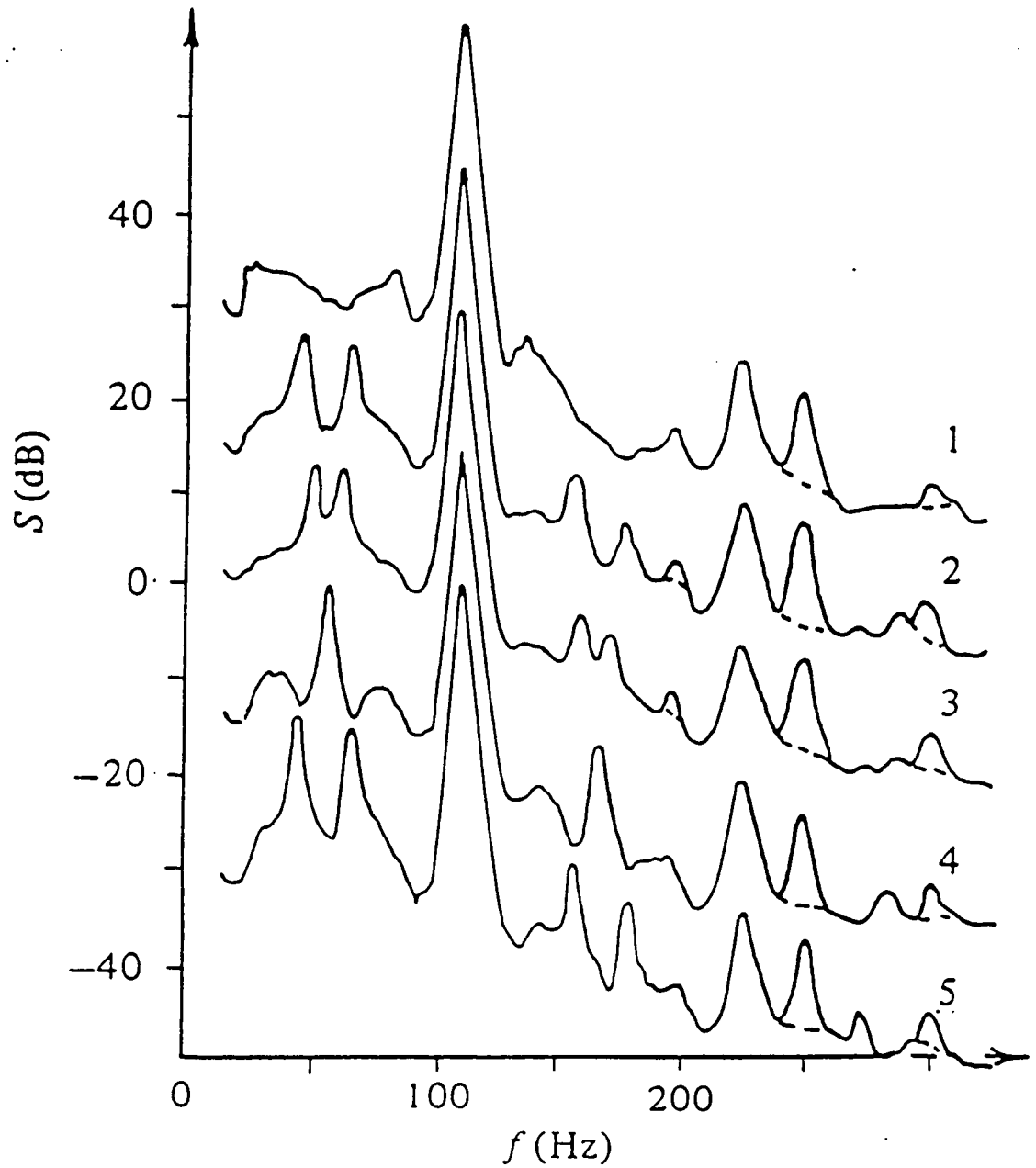

FIGURE 3.2 Spectra at frequency detunings (from the subh.) Δf of −30 Hz (1), −10 Hz (2), −5 Hz (3), 0 (4), +10 Hz (5). R = 633, F=124. (Kachanov and Levchenko (1984)).

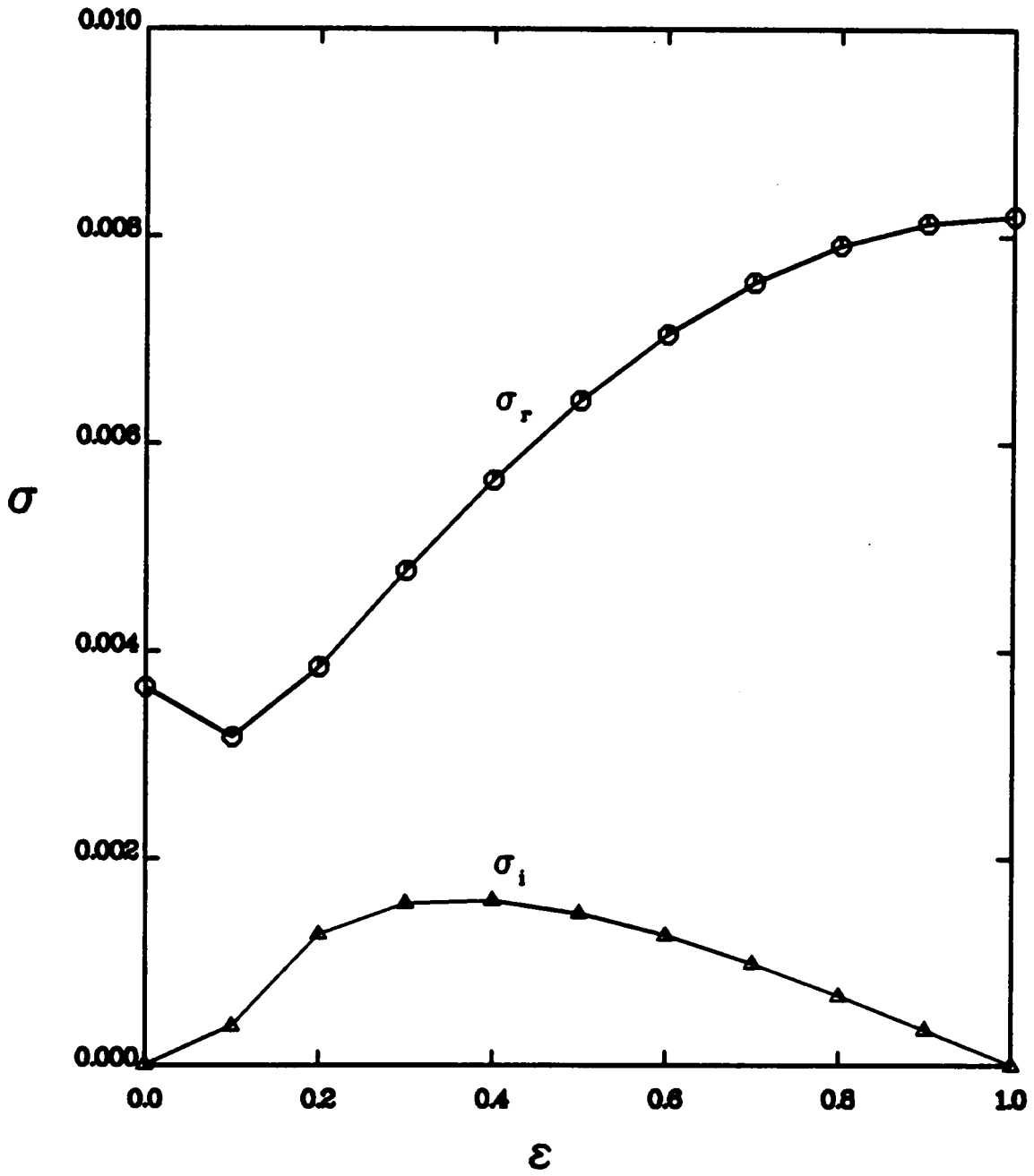

FIGURE 3.3 Growth rates and frequency shifts of detuned modes as a function of the detuning parameter ε for A = 1%, F = 124, Re = 606, α = 0.2033 and β = 0.2.

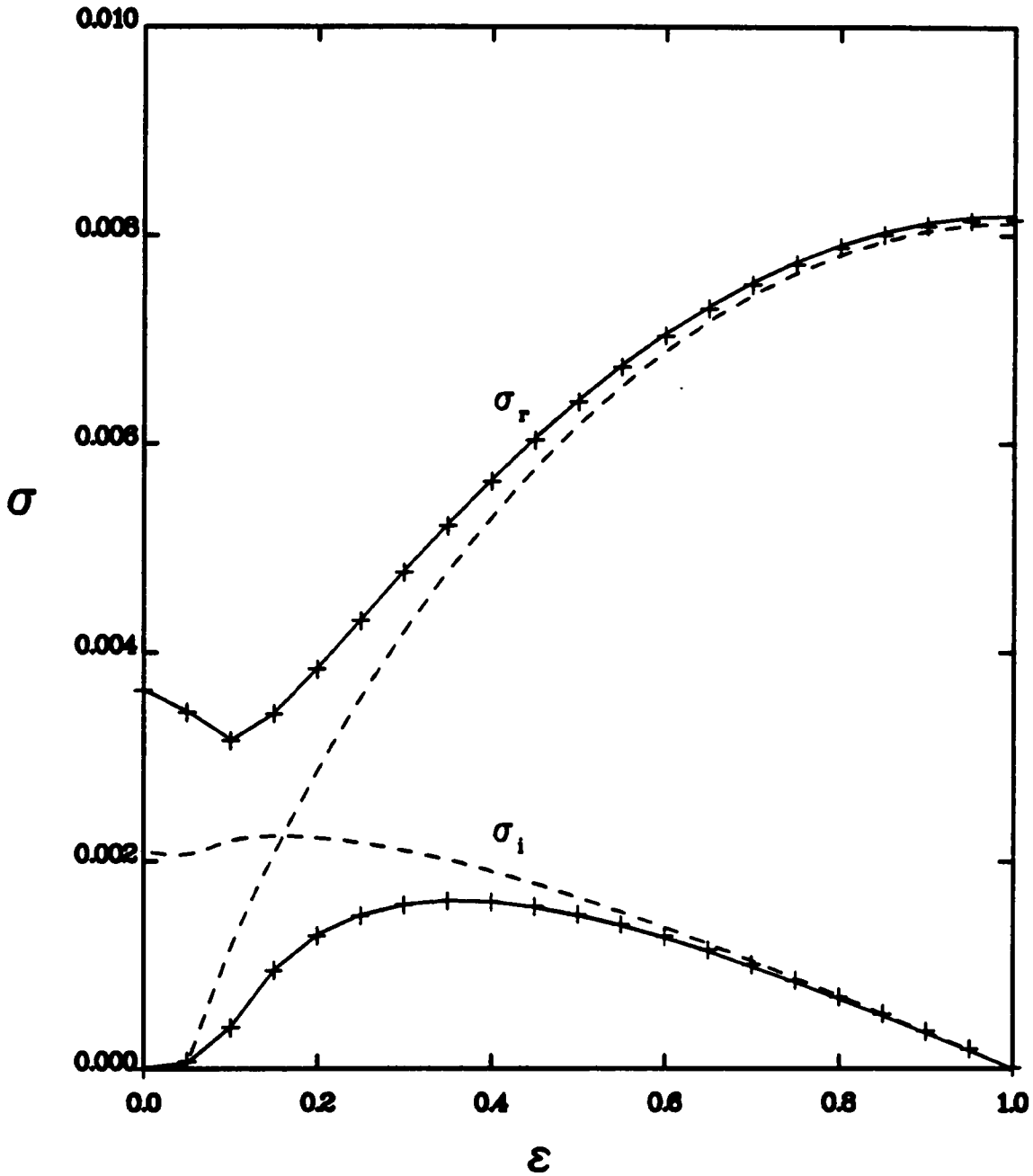

FIGURE 3.4 Growth rates and frequency shifts of detuned modes, obtained with 2 (– –), 3 (+) and 4 (–) Fourier modes. F = 124, Re = 606, α = 0.2033, β = 0.2 and A = 1%, JJ = 20.

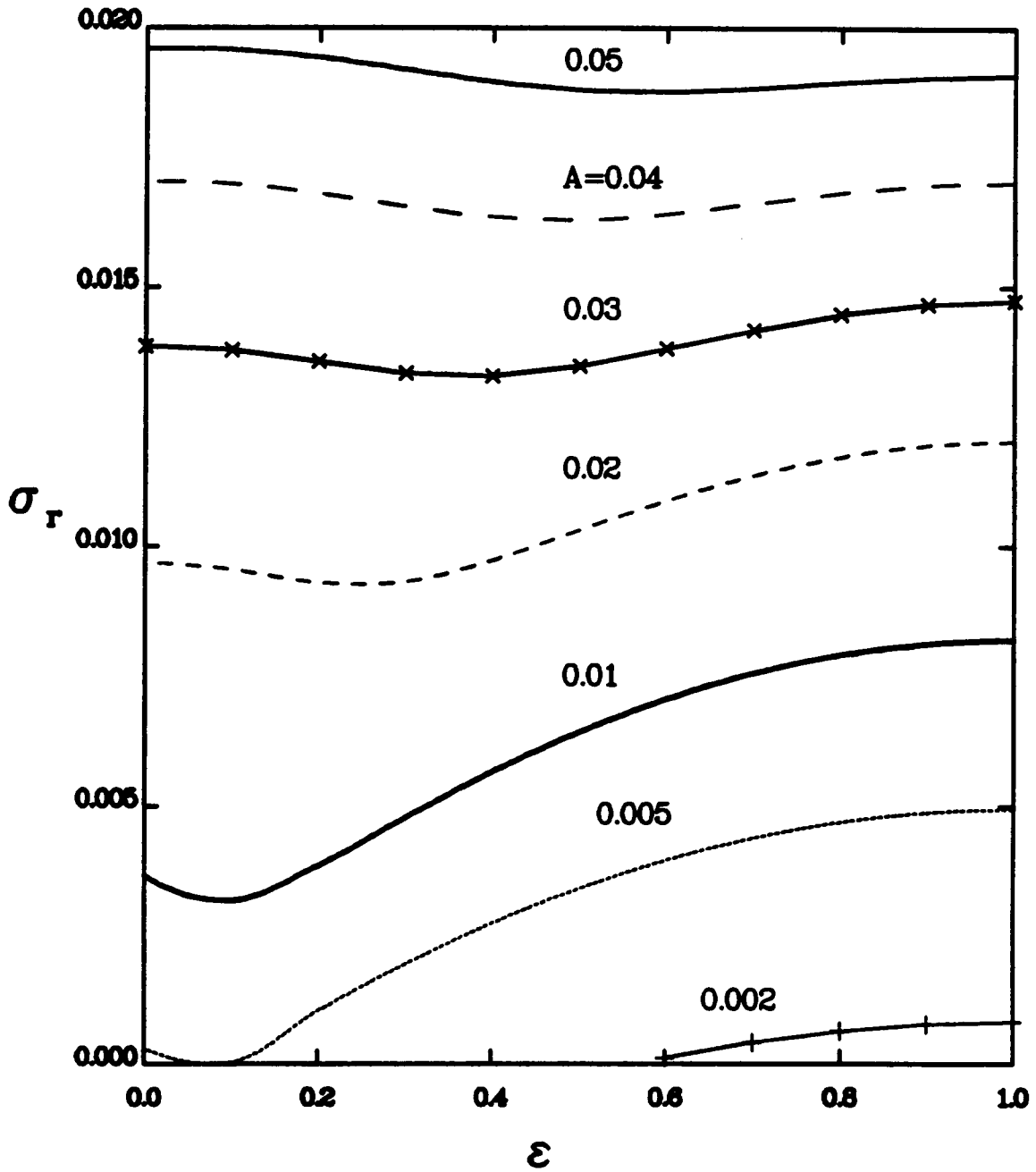

FIGURE 3.5 Growth rate of detuned modes as a function of the detuning parameter ε for various amplitudes of the TS wave. F = 124, R = 606, α= 0.2033, β = 0.2.

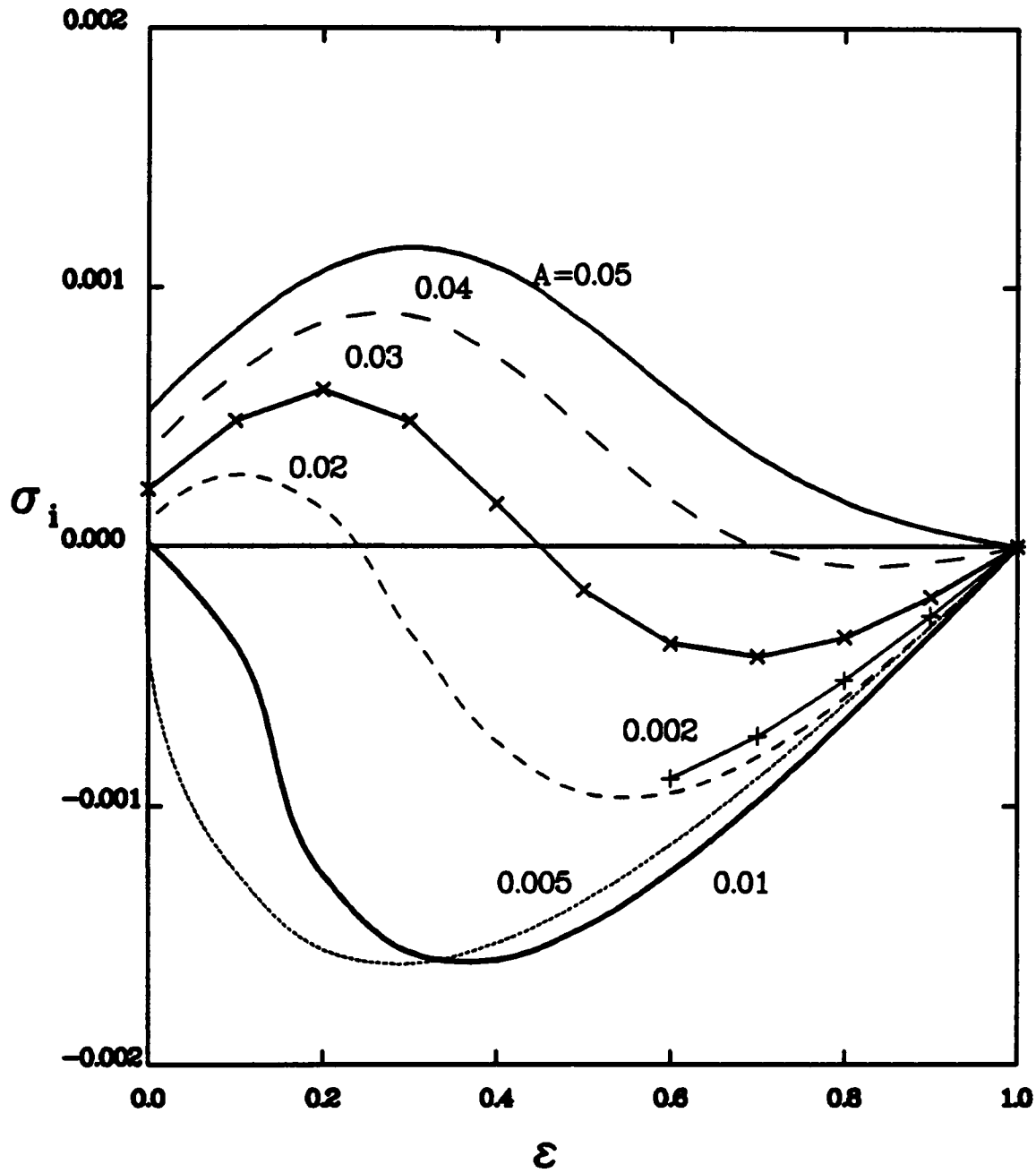

FIGURE 3.6 Frequency shifts of detuned modes as a function of the detuning parameter ε for various amplitudes of the TS wave. F = 124, R = 606, α= 0.2033, β = 0.2.

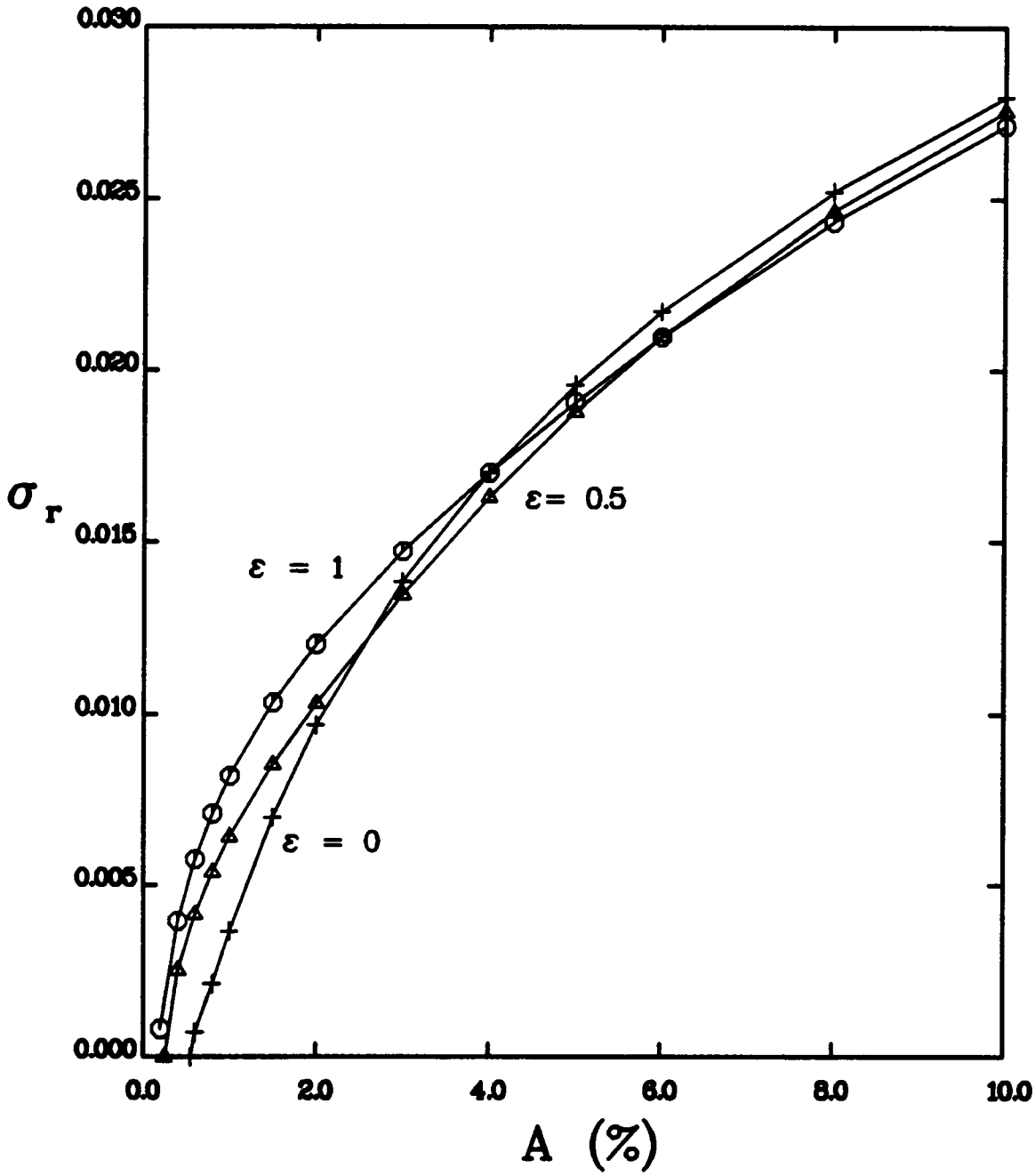

FIGURE 3.7 Growth rate of modes with ε = 0, 0.5 and 1.0 as a function of the TS amplitude. F = 124, R = 606, α = 0.2033, β = 0.2.

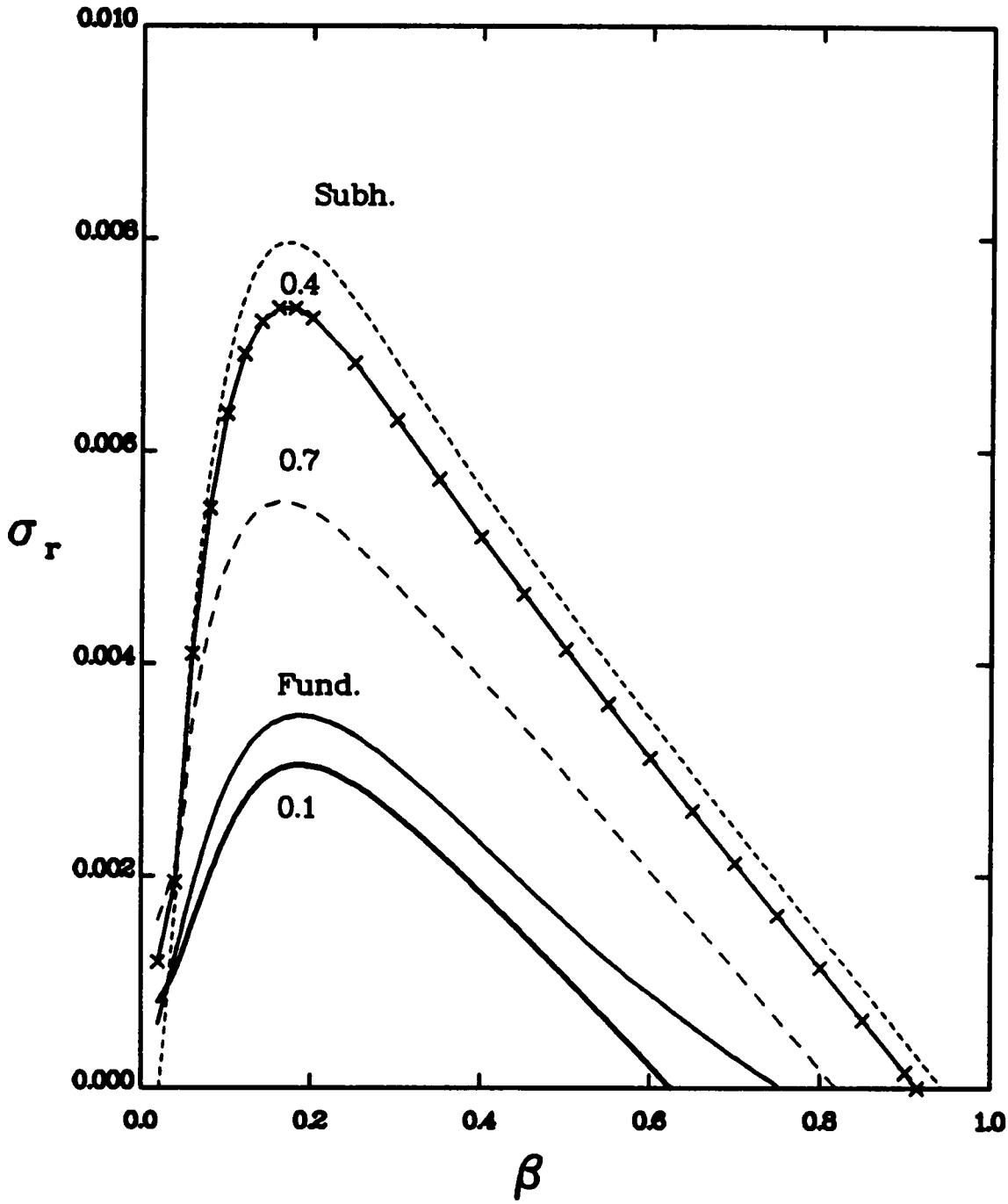

FIGURE 3.8. Growth rate of modes with $\varepsilon = 0$, 0.1, 0.4, 0.7 and 1.0 as a function of the spanwise wavenumber F = 124, R = 606, α = 0.2033, A = 0.01.

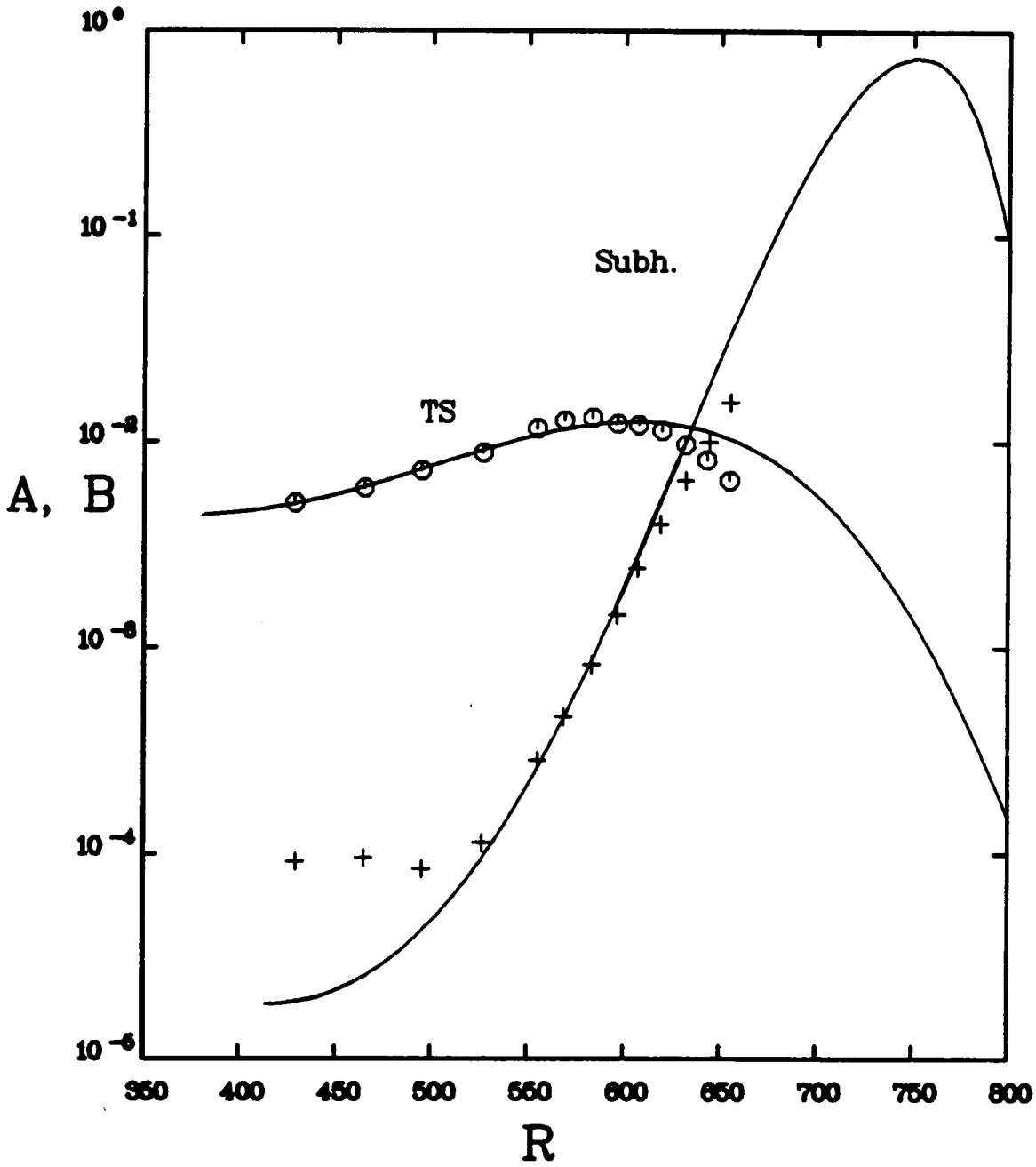

FIGURE 3.9 Streamwise variation of the amplitudes of the TS and of the subharmonic mode. Comparison between theory (–) and experiment (+,o). F=124, Ao=0.0044, Bo=0.0000186, b=0.33

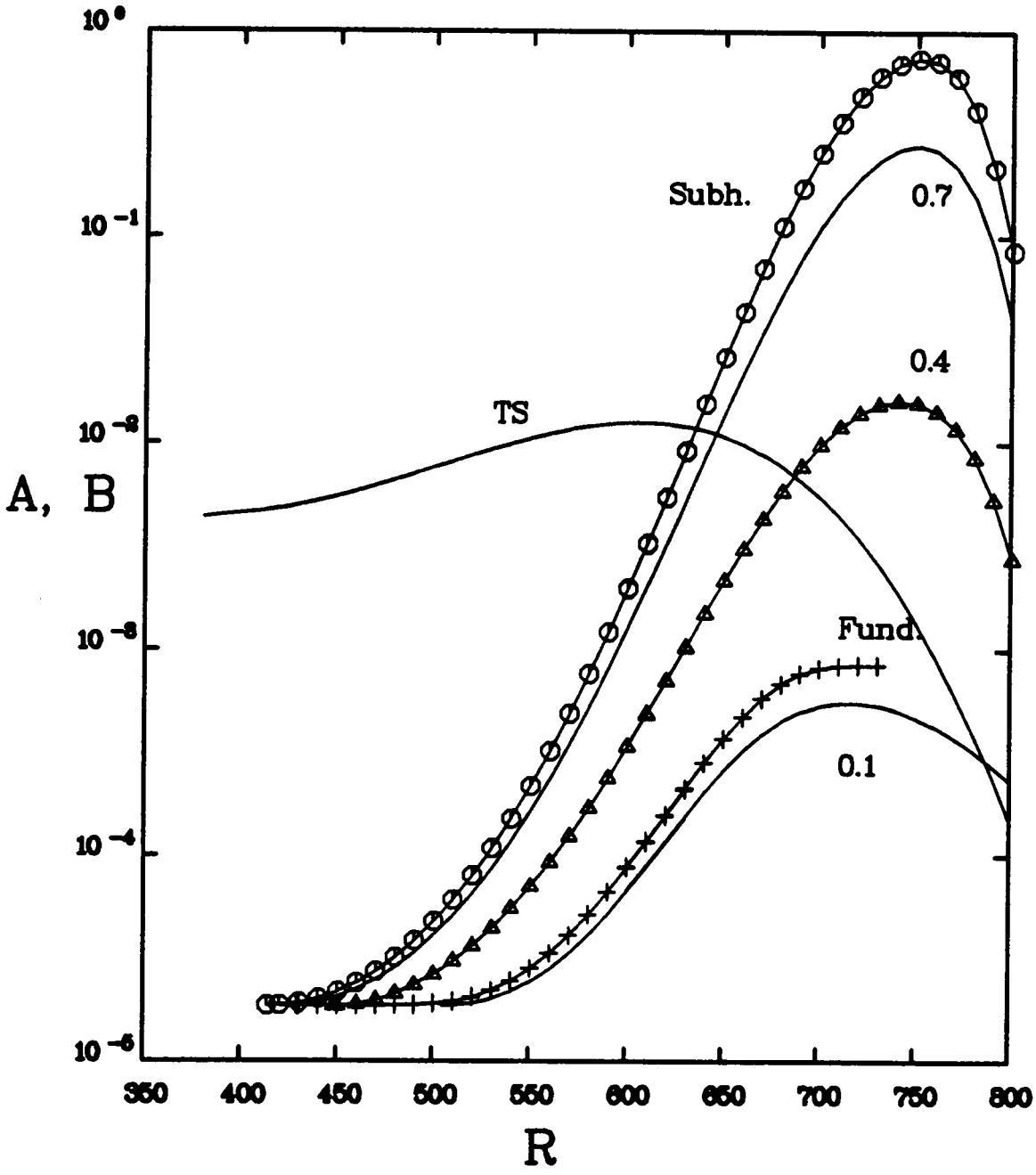

FIGURE 3.10 Streamwise Variation of the TS amplitude A and the amplitude B of secondary modes with different detunings. F = 124, Ao=0.0044, Bo=0.0000186, b=0.33 and a ~ 0.335.

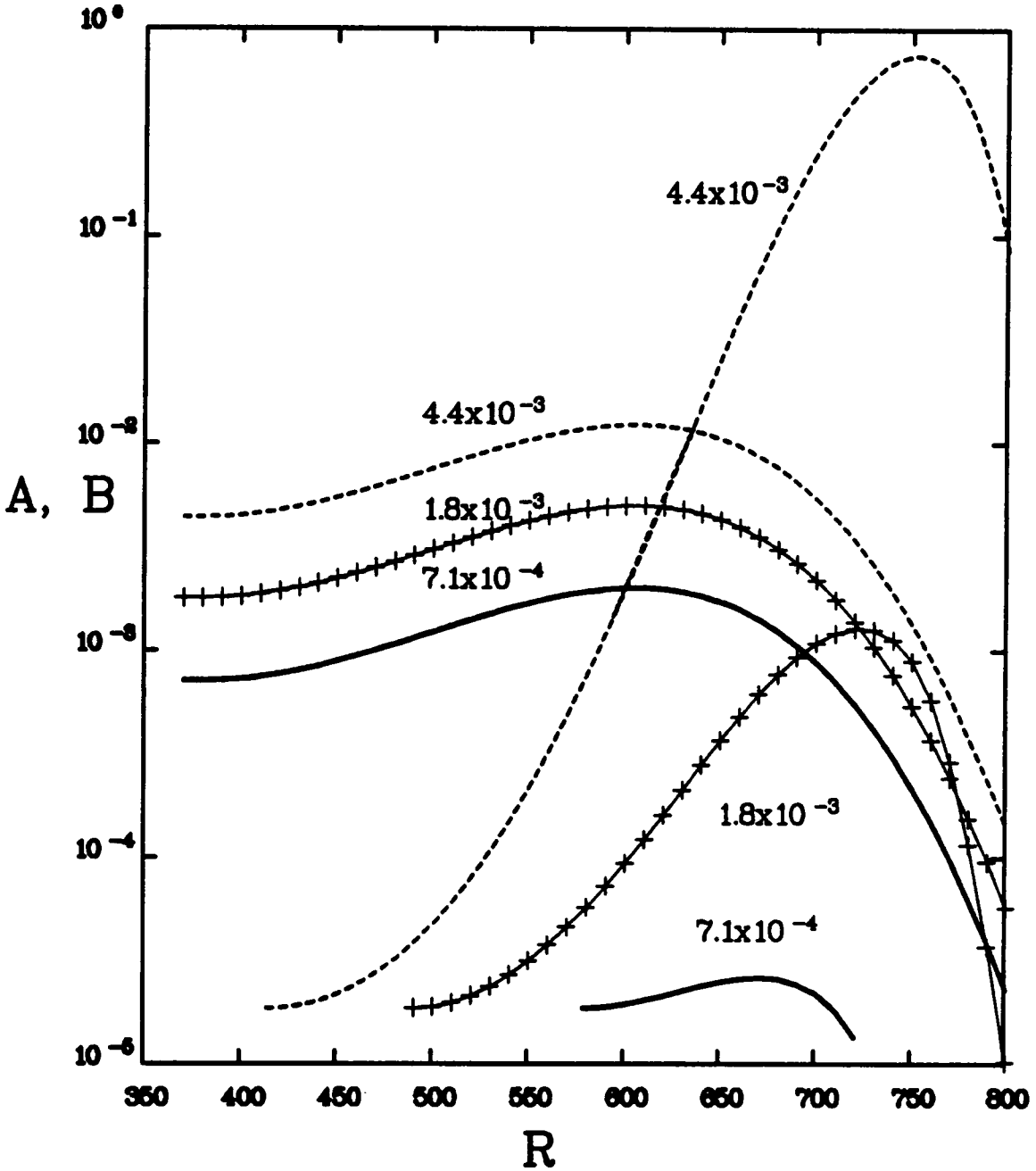

FIGURE 3.11 Streamwise Variation of the TS amplitude A and the amplitude B of subharmonic modes with different initial amplitudes Ao. F = 124, Bo=0.0000186, b=0.33 and a ~ 0.335.

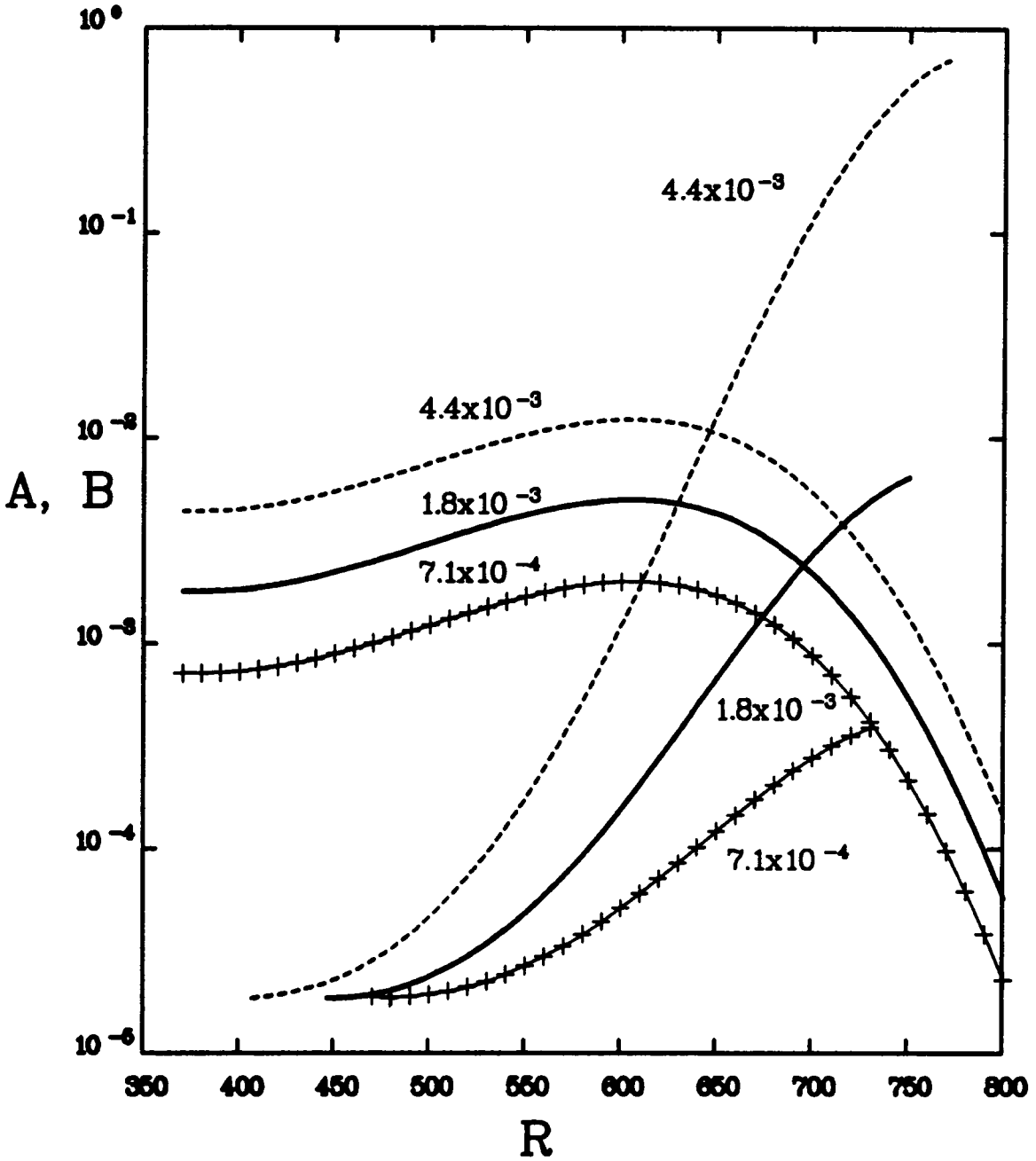

FIGURE 3.12 Streamwise Variation of the TS amplitude A and the amplitude B of subharmonic modes with different initial amplitudes Ao. F = 124, Bo=0.0000186, b=0.19 and a ~ 0.335.

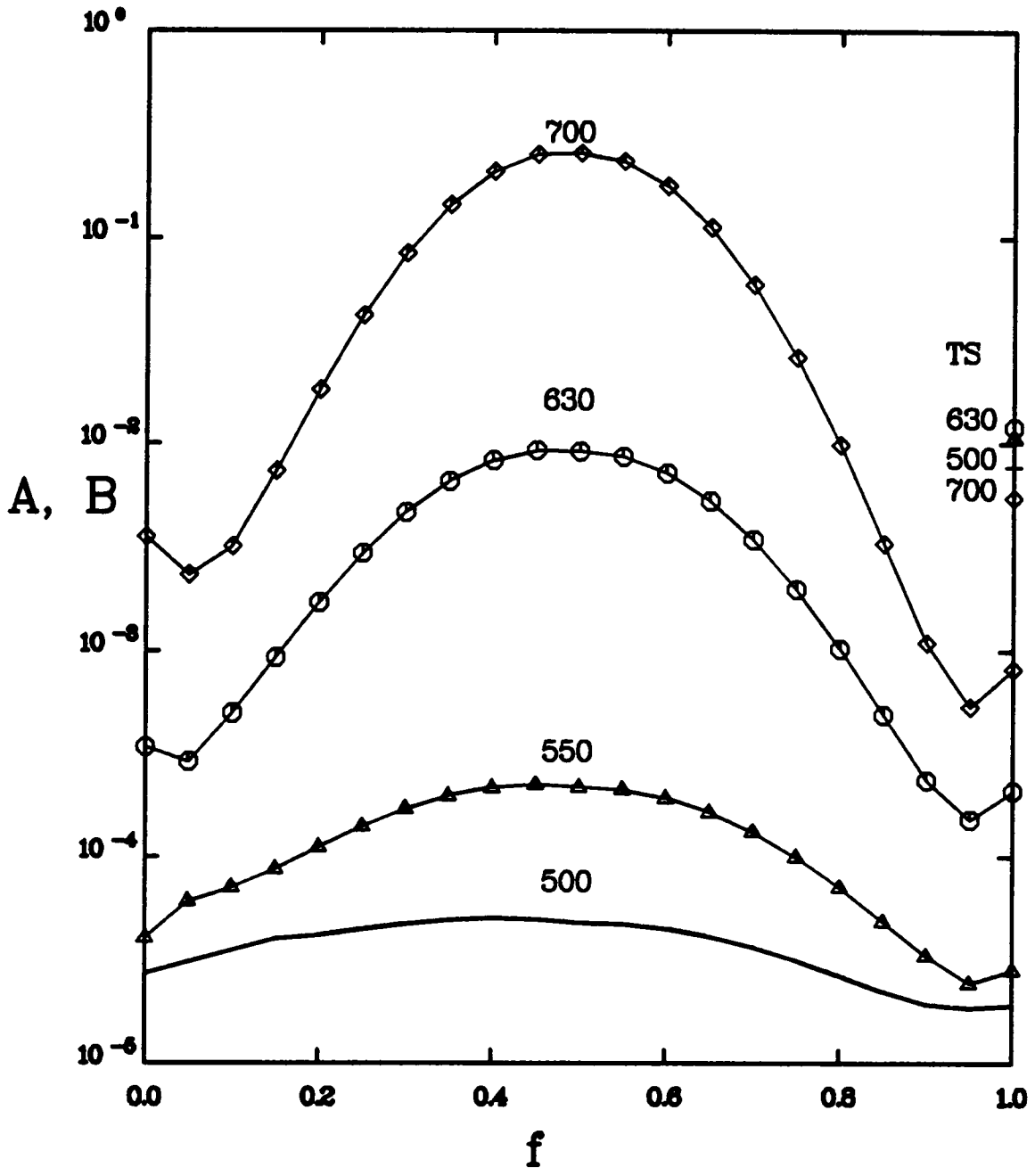

FIGURE 3.13 Streamwise evolution of the amplitude spectra of secondary instability modes. Frequency shift neglected. Ao=0.0044, F= 124, Bo=0.0000186, b=0.19 and a ~ 0.335

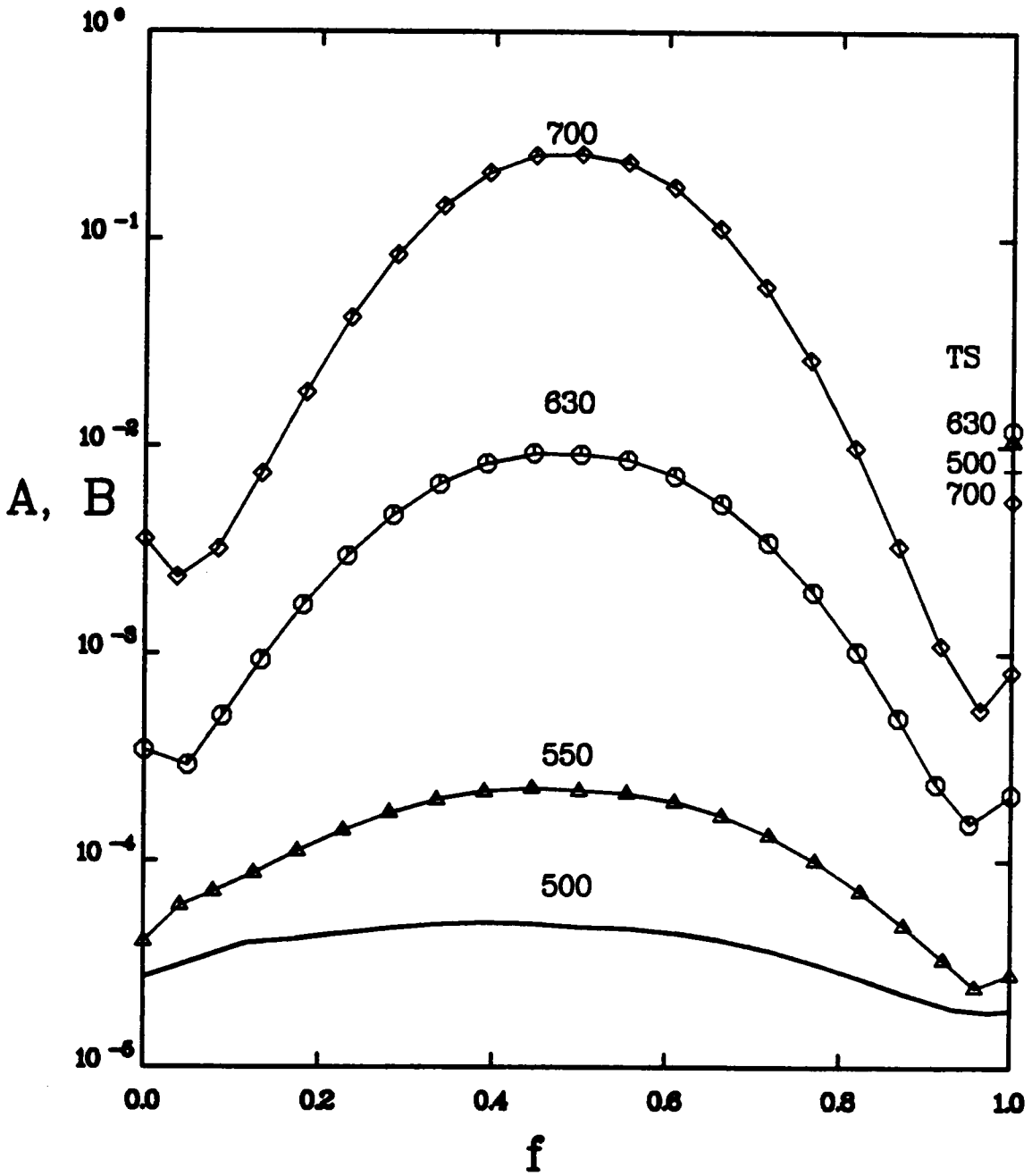

FIGURE 3.14 Streamwise evolution of the amplitude spectra of secondary instability modes. Frequency shift included. Ao=0.0044, F= 124, Bo=0.0000186, b=0.19 and a ~ 0.335

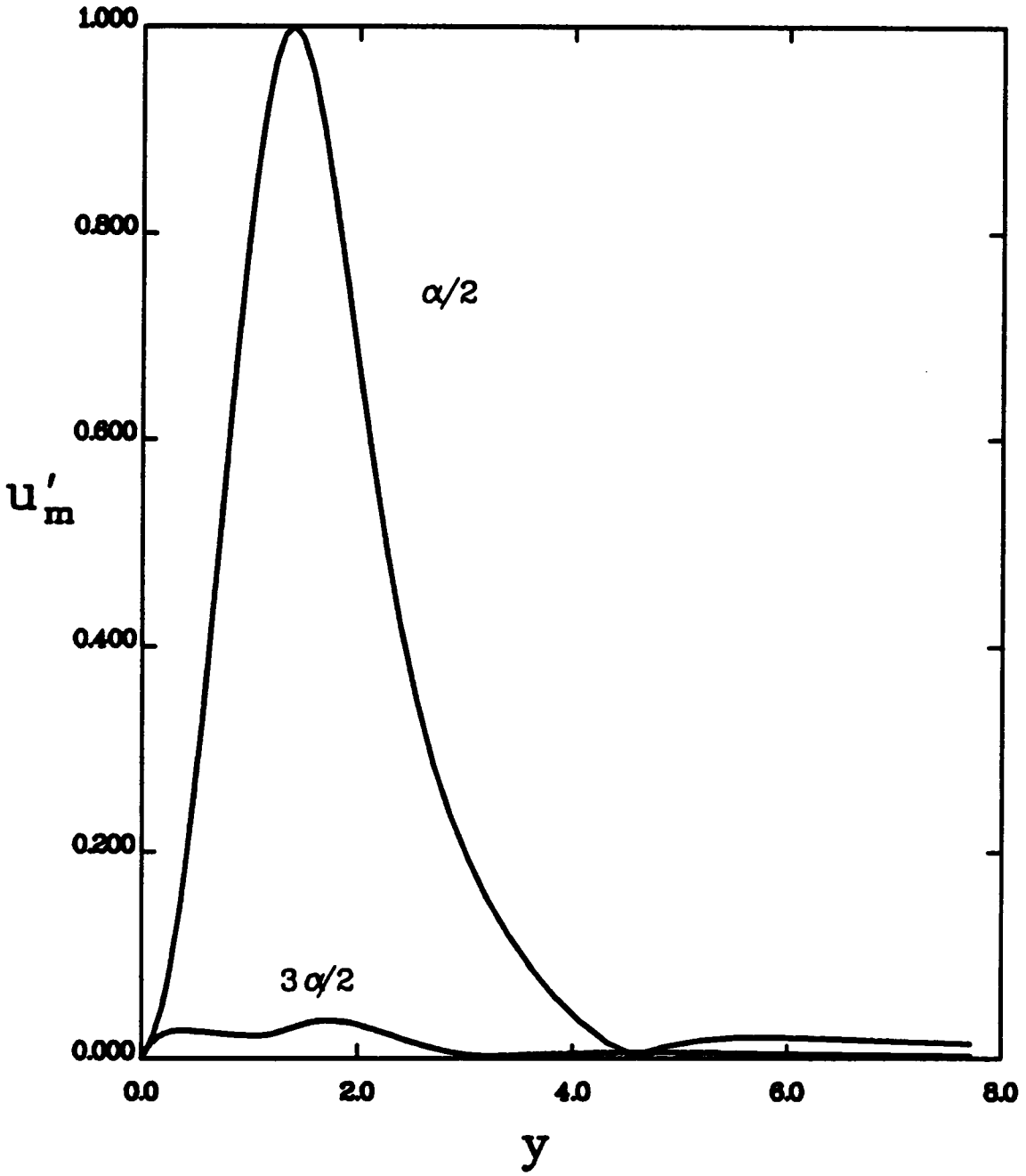

FIGURE 3.15 Normalized streamwise velocity components. Subharmonic mode (ε = 1.0), R = 606, α= 0.1017, A = 0.01, β = 0.2.

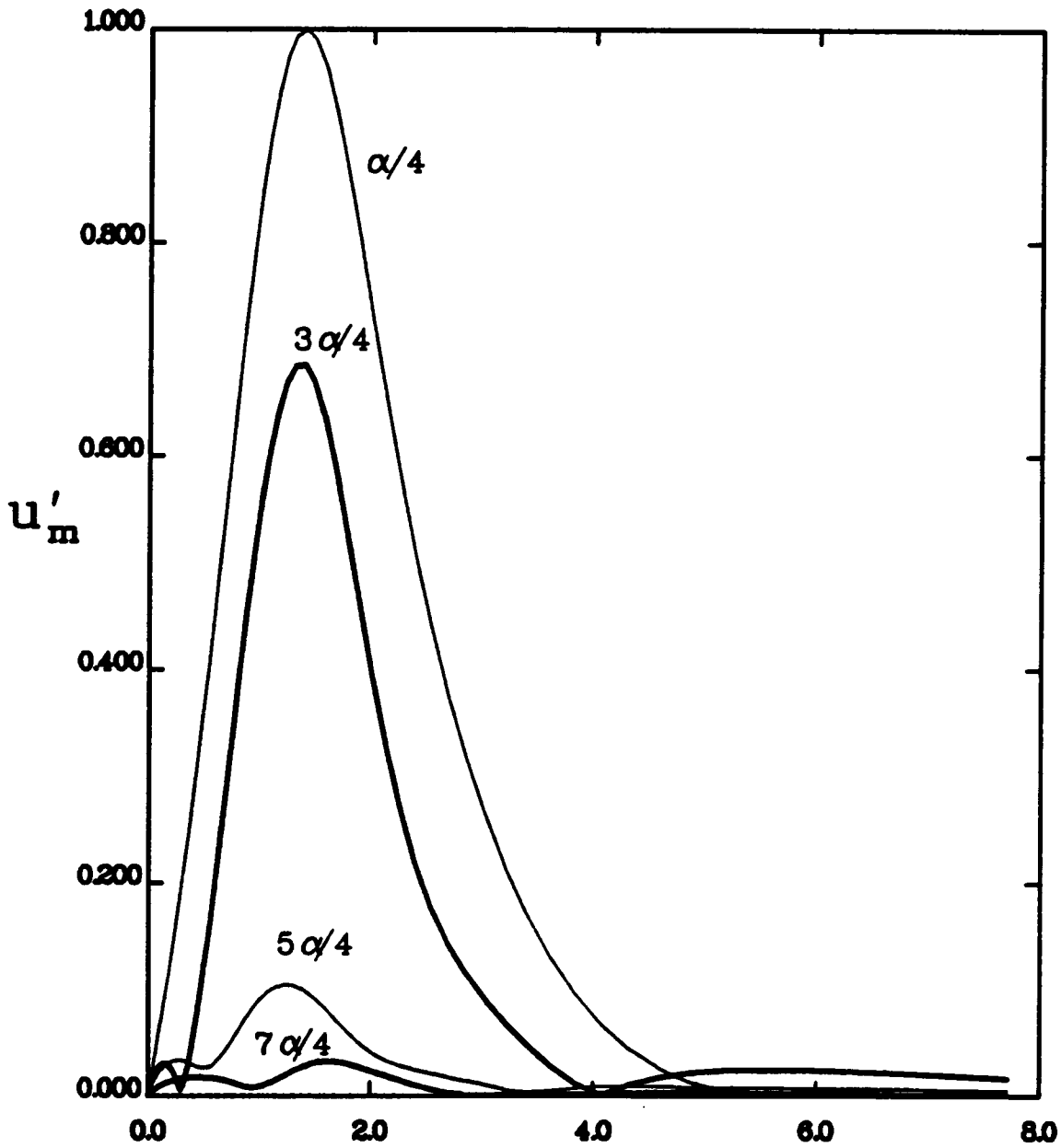

FIGURE 3.16 Normalized streamwise velocity components. Detuned mode (ε = 0.5), R = 606, α= 0.1017, A = 0.01, β = 0.2.

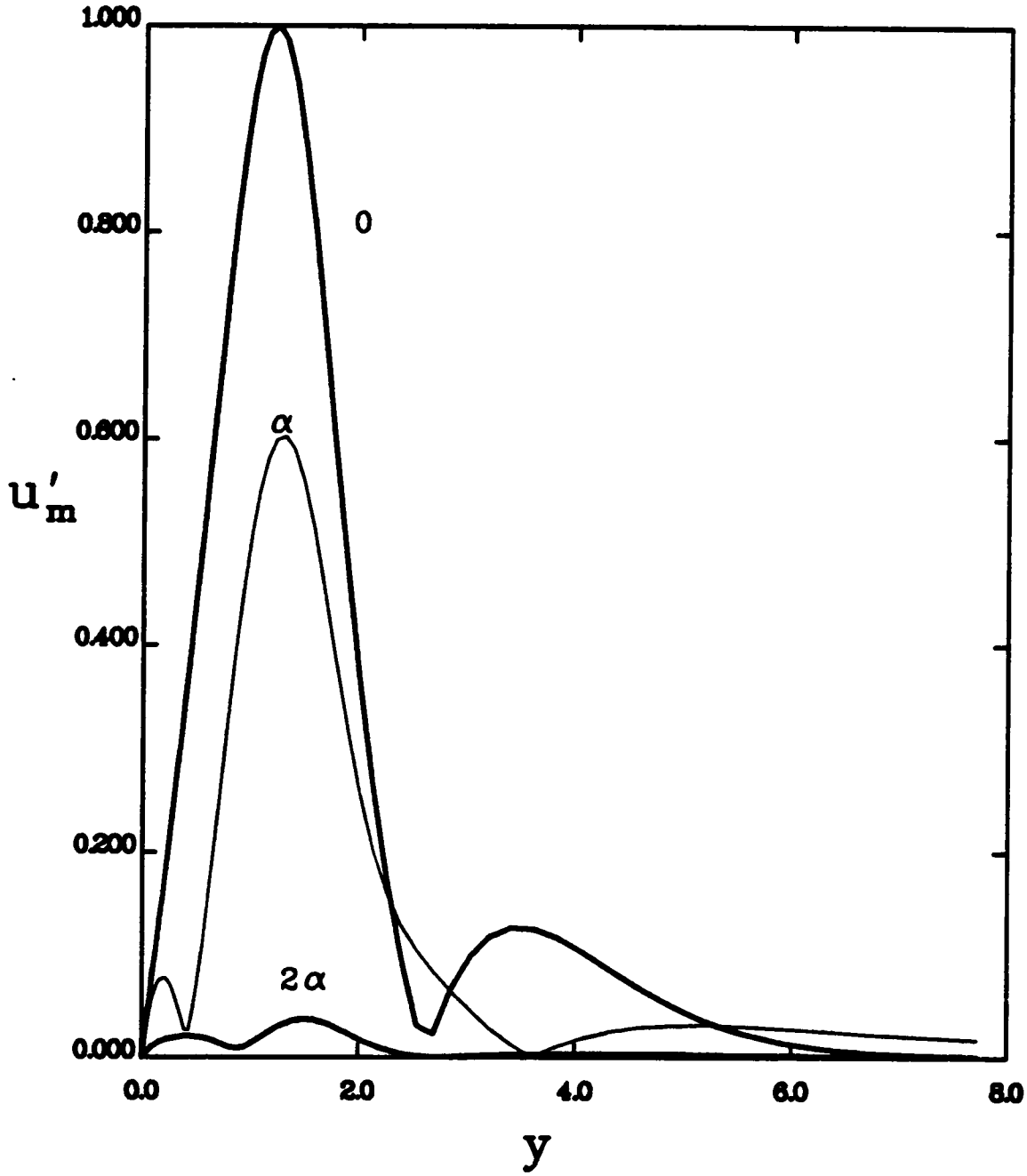

FIGURE 3.17 Normalized streamwise velocity components. Fundamental mode (ε = 0), R = 606, α= 0.1017, A = 0.01, β = 0.2.

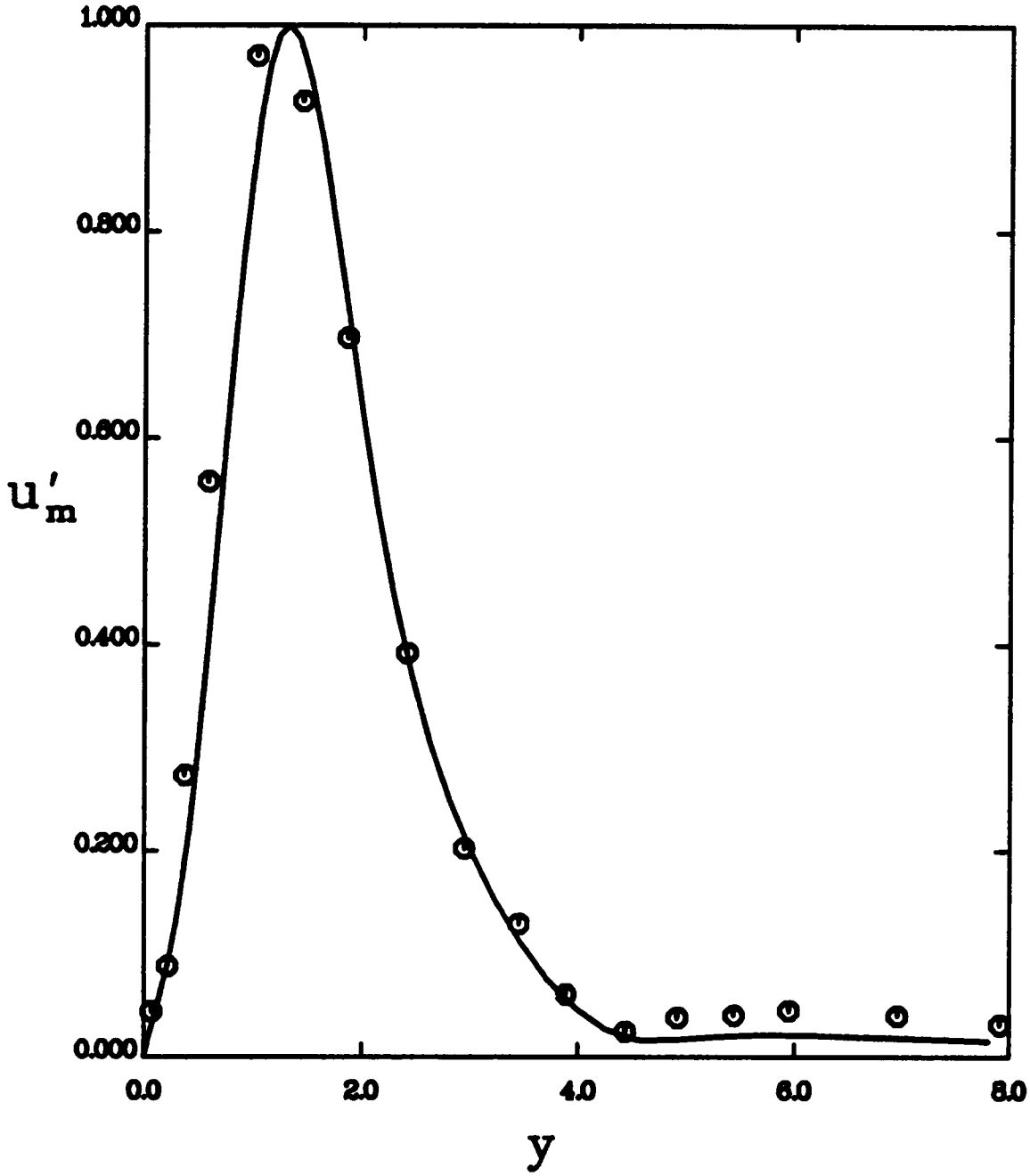

FIGURE 3.18. Normalized streamwise rms fluctuation of the subharmonic mode. Comparison with experiments (o) R = 608, F = 124, A = 0.0122, b = 0.33. (From Herbert)

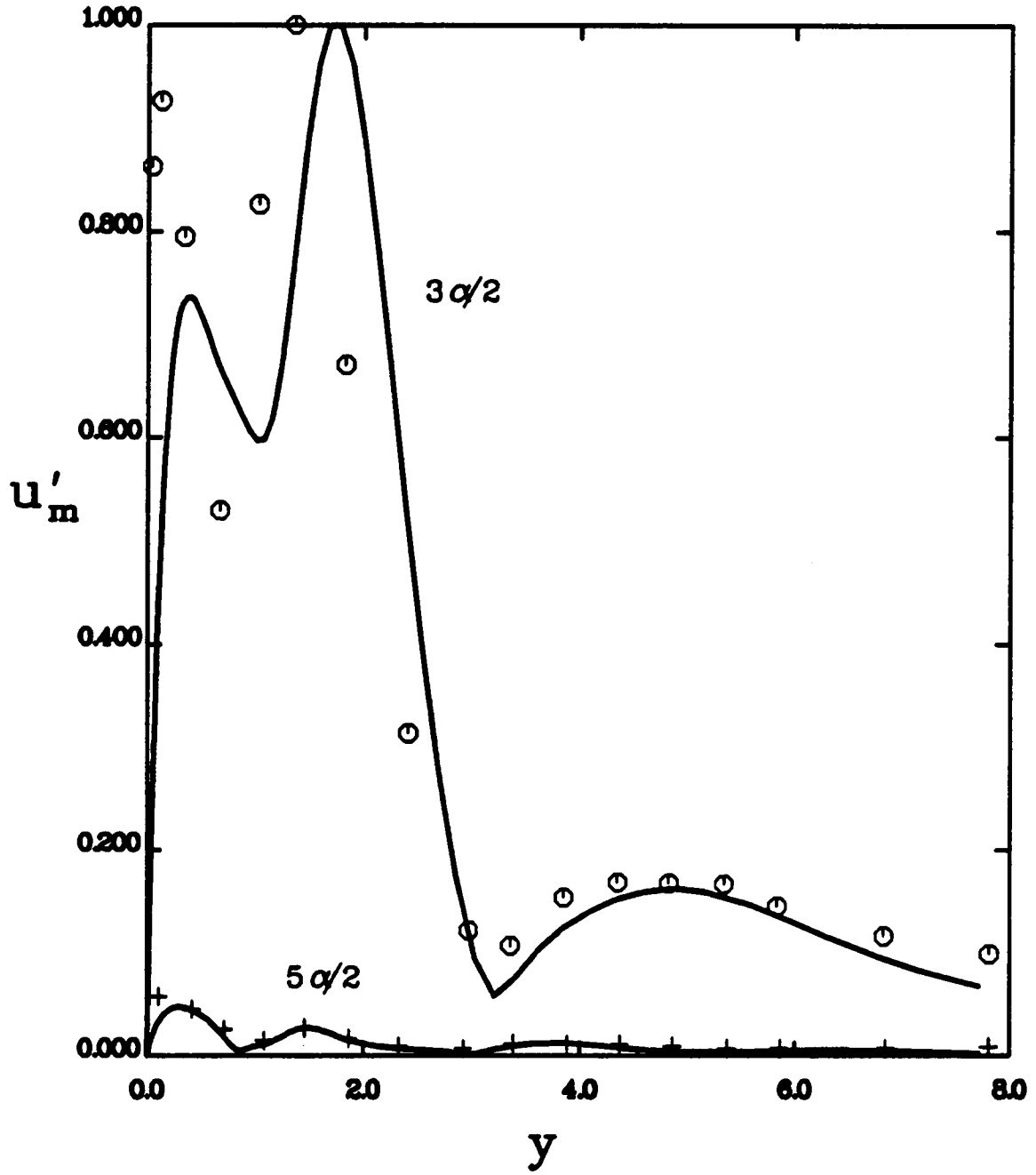

FIGURE 3.19. Normalized streamwise rms fluctuations of the subharmonic components with $3\alpha/2$ and $5\alpha/2$. Theory(−), experiment (o,+). R = 608, F = 124, A = 0.01.

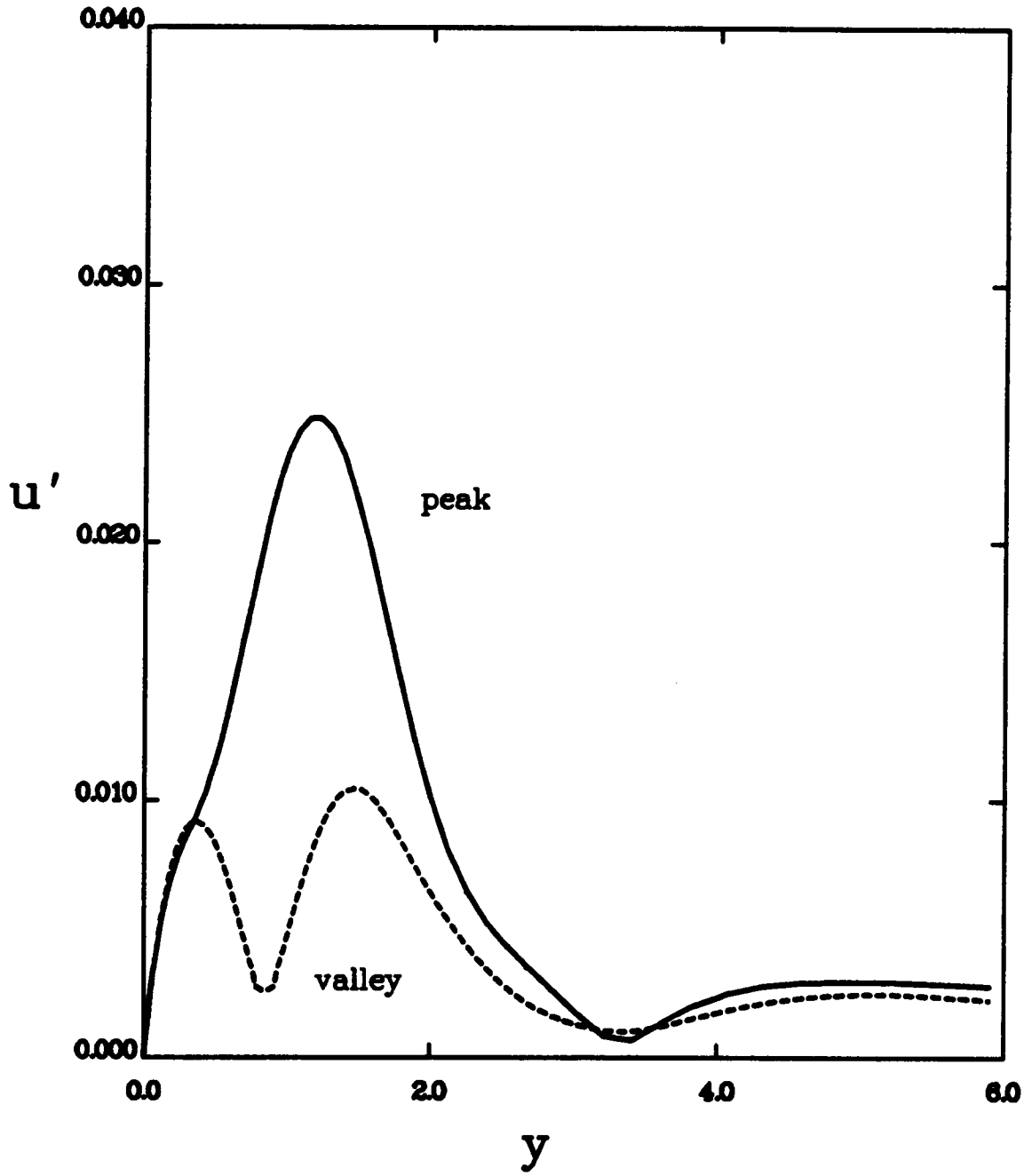

FIGURE 3.20. Streamwise rms fluctuation at the peak and valley for temporally growing fundamental.
R = 606, F=124, A = 0.01, α = 0.2034, β = 0.2

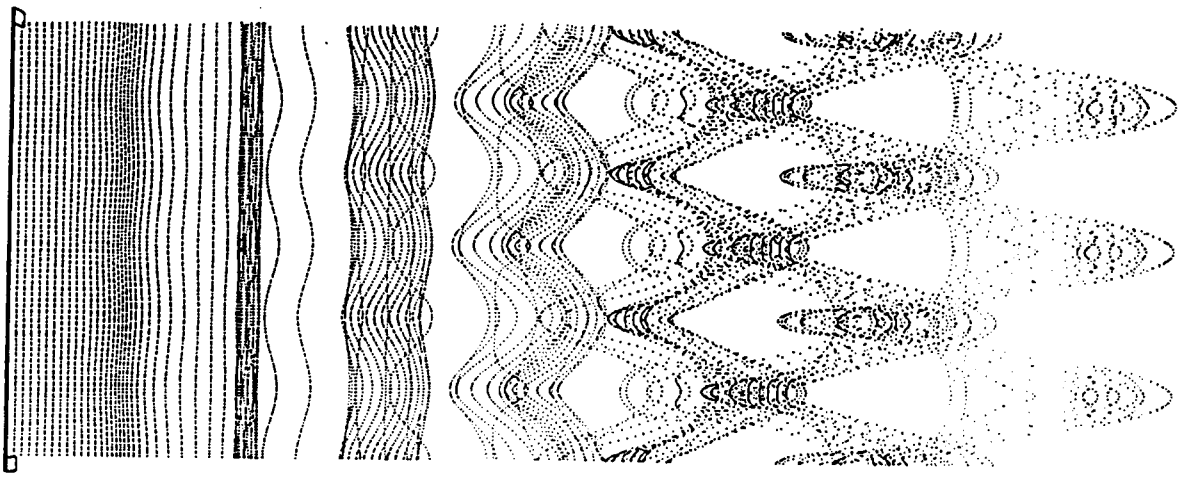

FIGURE 3.21. Computer-generated 'staggered' pattern of particles convected in the three-dimensional flow that develops from secondary instability to a subharmonic mode.

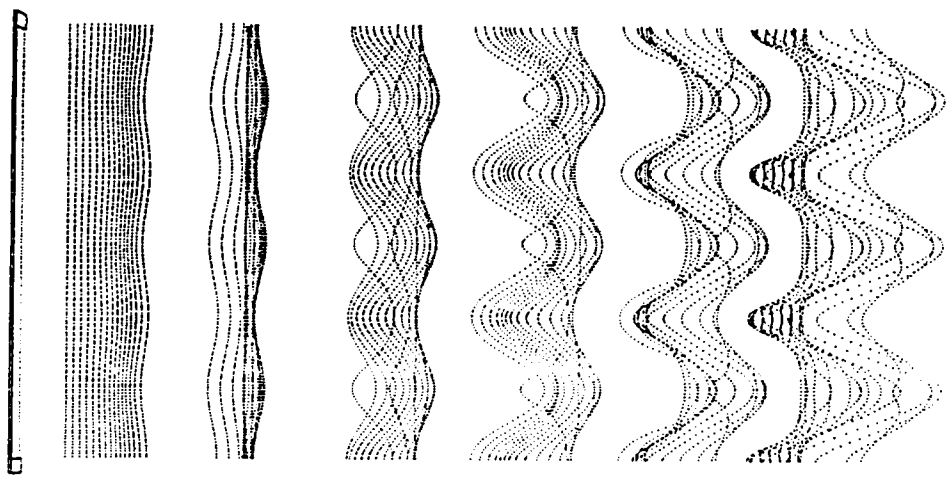

FIGURE 3.22. Computer-generated 'aligned' pattern of particles convected in the three-dimensional flow that develops from secondary instability to a fundamental mode.

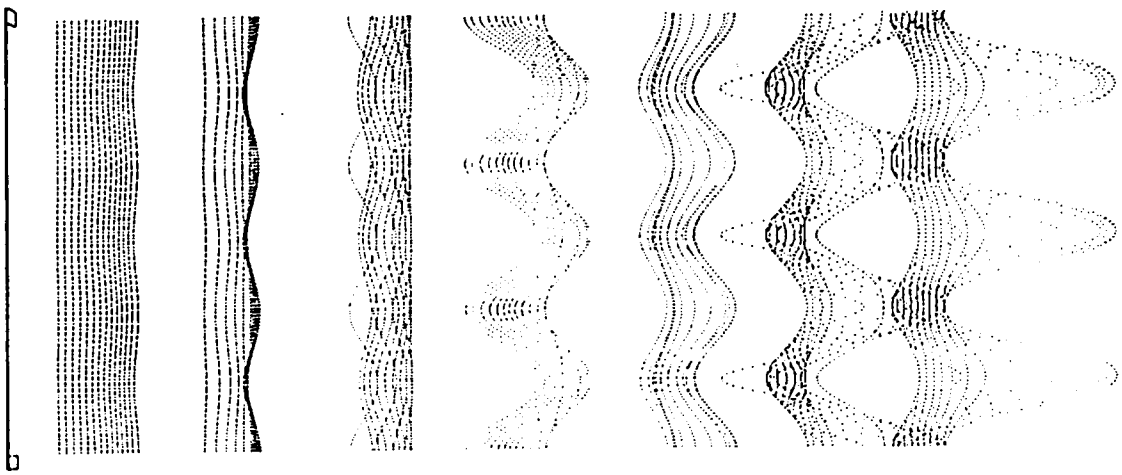

FIGURE 3.23. Computer-generated pattern of particles convected in the three-dimensional flow that develops from secondary instability to a combination mode with $\varepsilon = 0.6$.

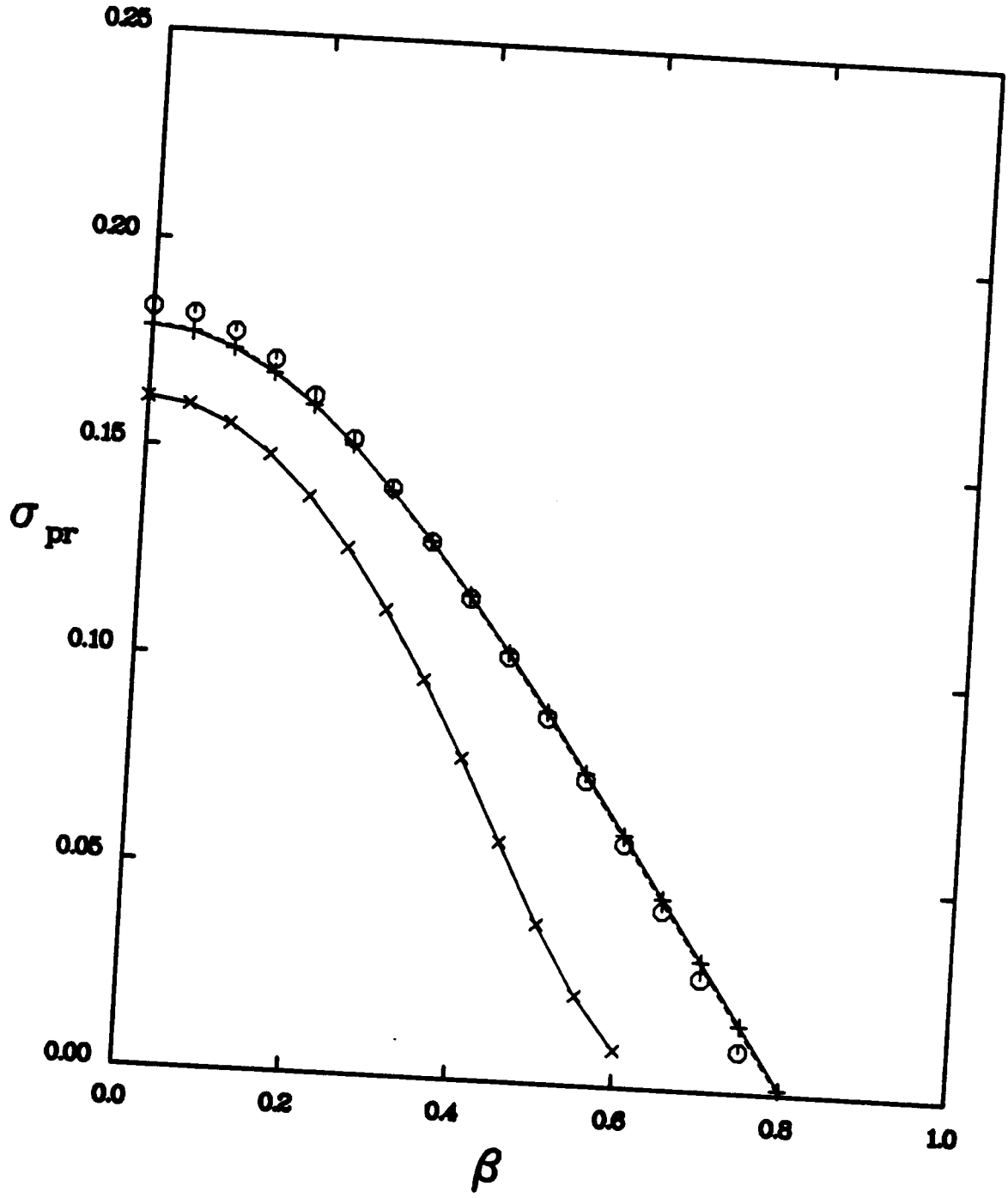

FIGURE 4.1 Growth rates of the TS as a function of β for ηo = 0.5 (o), 1 (+), 2 (--) and 4 (x). Solution using Chebyshev polynomials. α = 0.5, JJ = 17, R =200.

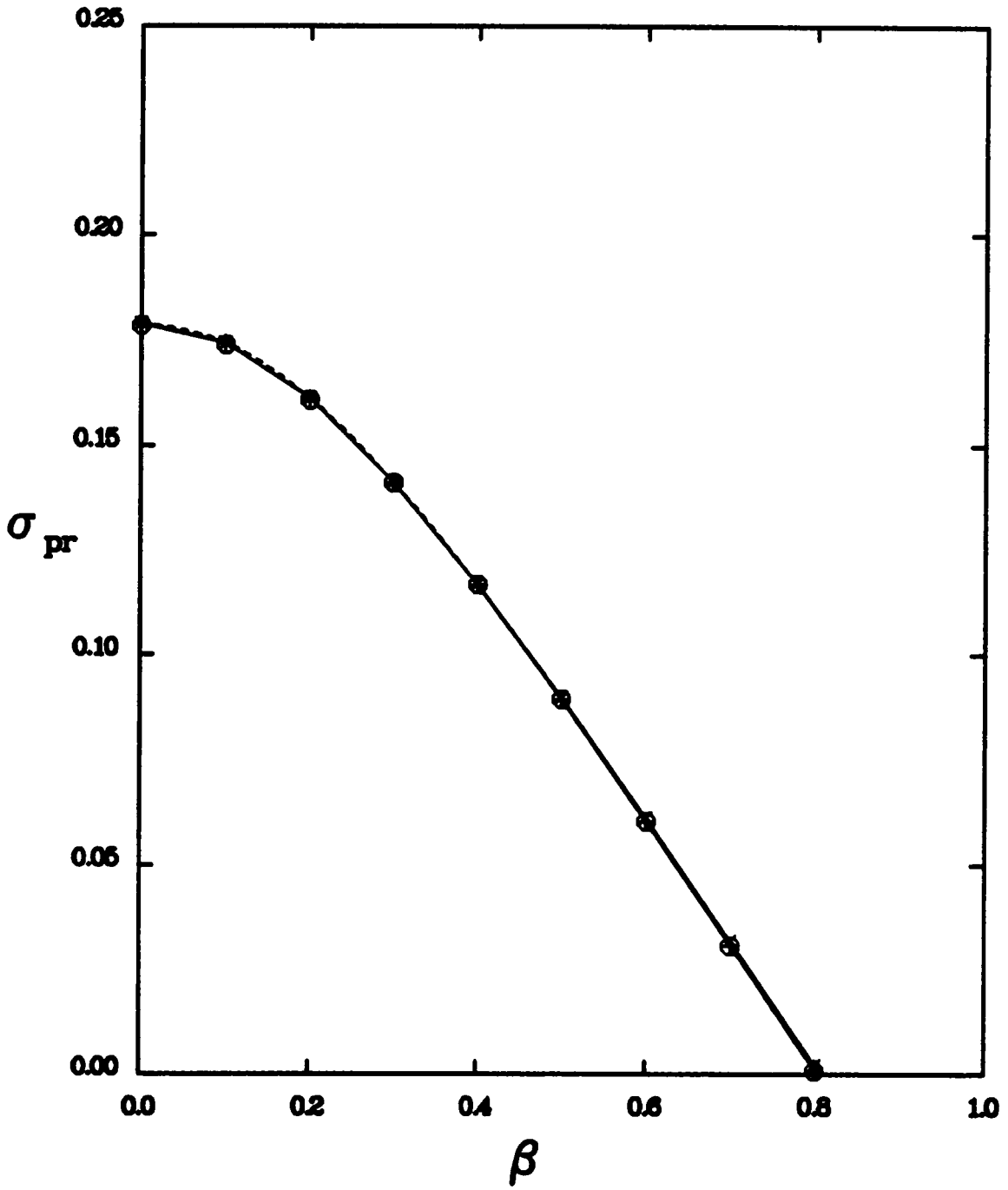

FIGURE 4.2 Growth rates of the TS as a function of β for ηo = 0.5 (o), 1 (+), 2 (--) and 4 (x). Solution using Chebyshev polynomials. α = 0.5, JJ = 32, R =200.

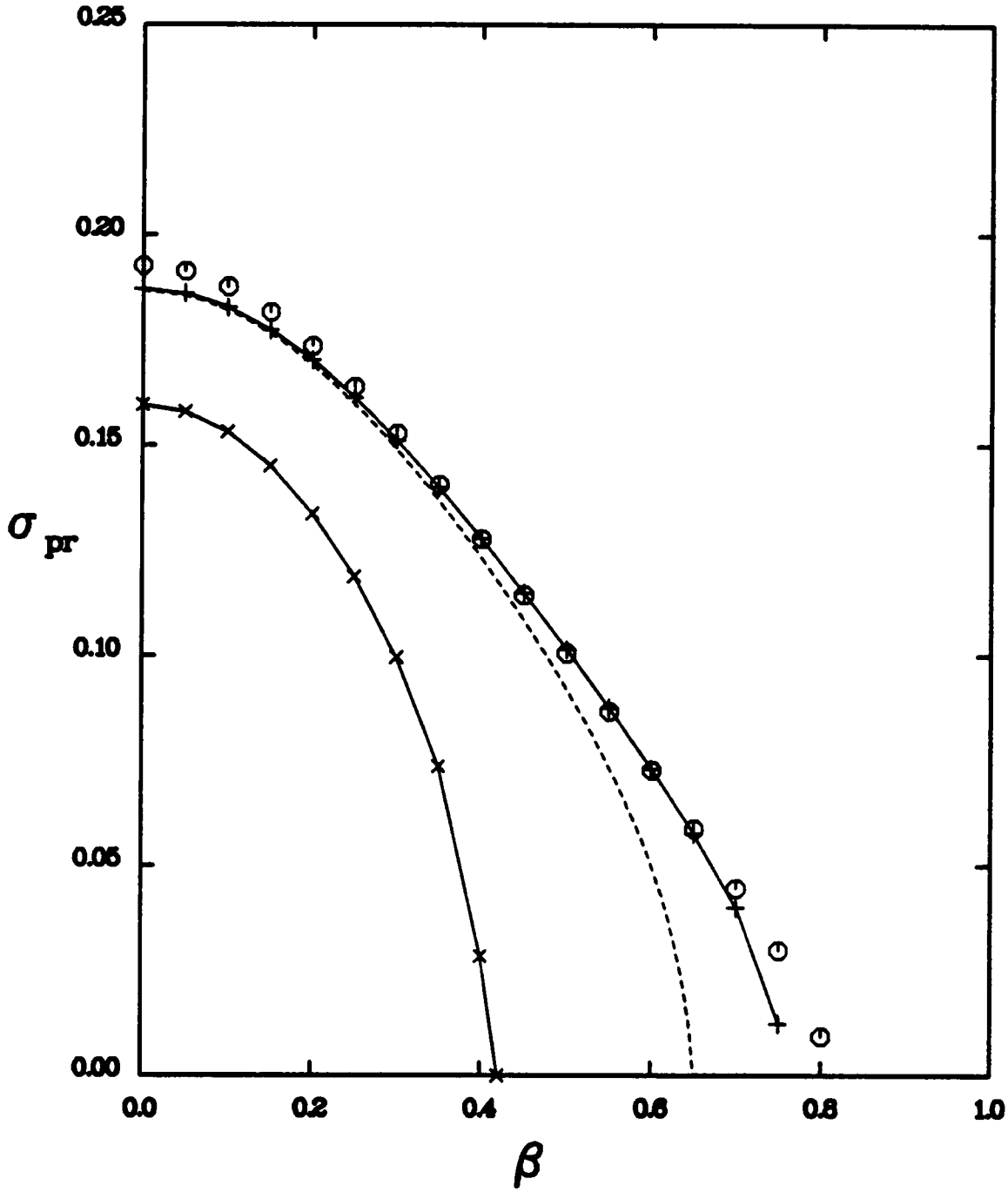

FIGURE 4.3 Growth rates of the inviscid TS as a function of β for mapping parameters of 0.5 (o), 1 (+), 2 (--) and 4 (x). Solution using Chebyshev polynomials. α = 0.5, JJ = 17.

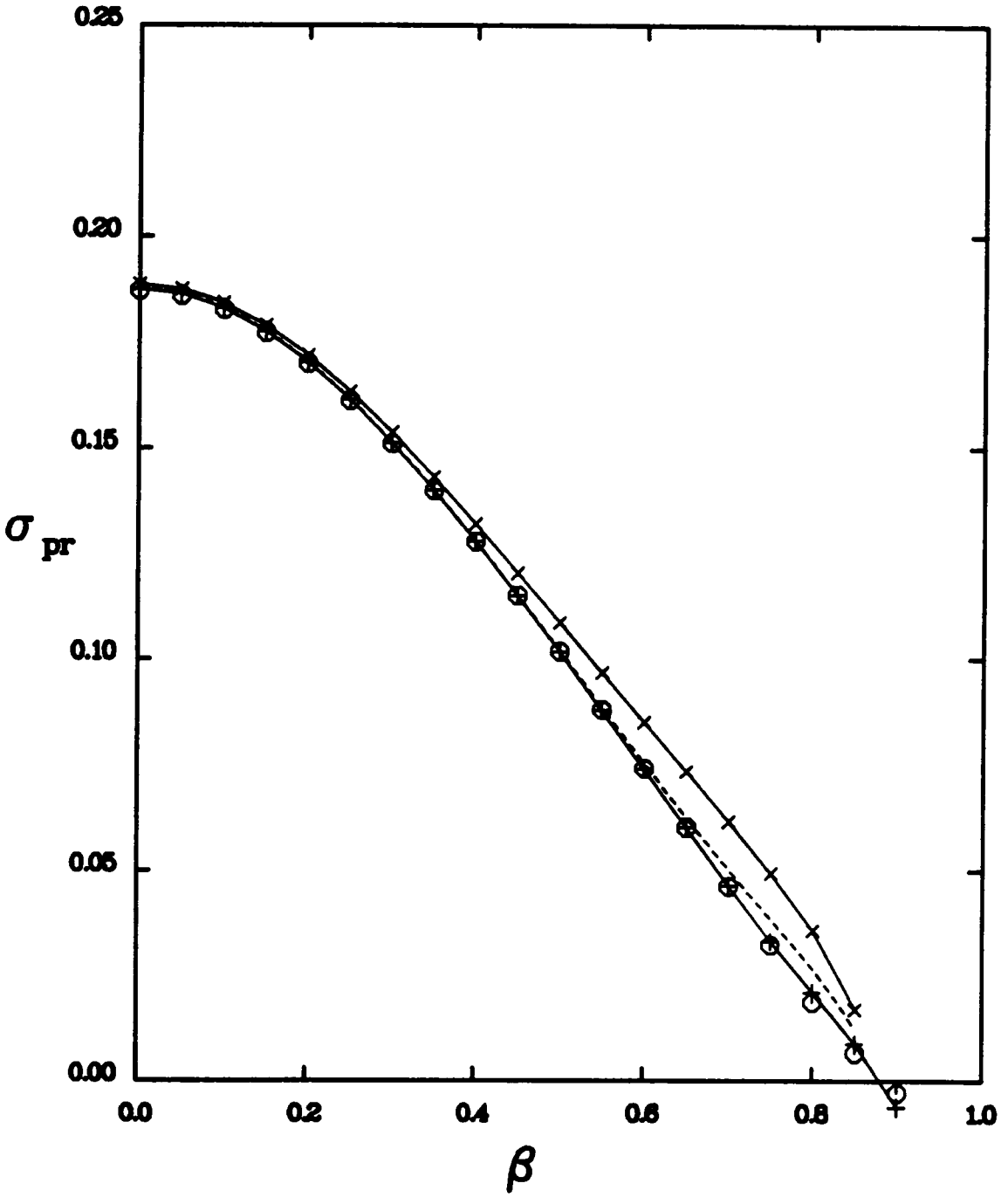

FIGURE 4.4 Growth rates of the inviscid TS as a function of β for mapping parameters of 0.5 (o), 1 (+), 2 (--) and 4 (x). Solution using Chebyshev polynomials. α = 0.5, JJ = 32.

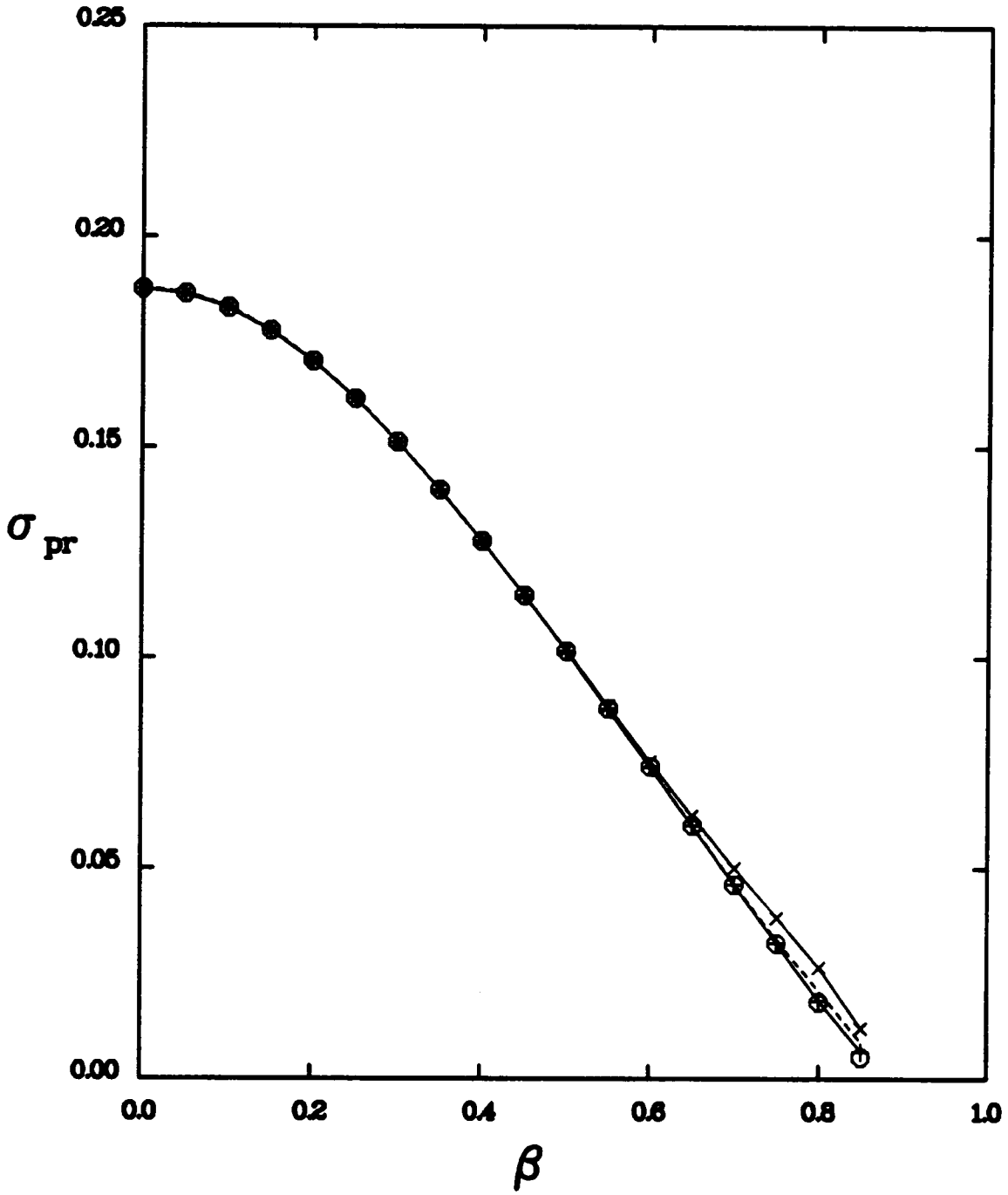

FIGURE 4.5 Growth rates of the inviscid TS as a function of β for mapping parameters of 0.5 (o), 1 (+), 2 (--) and 4 (x). Solution using Chebyshev polynomials. α = 0.5, JJ = 64.

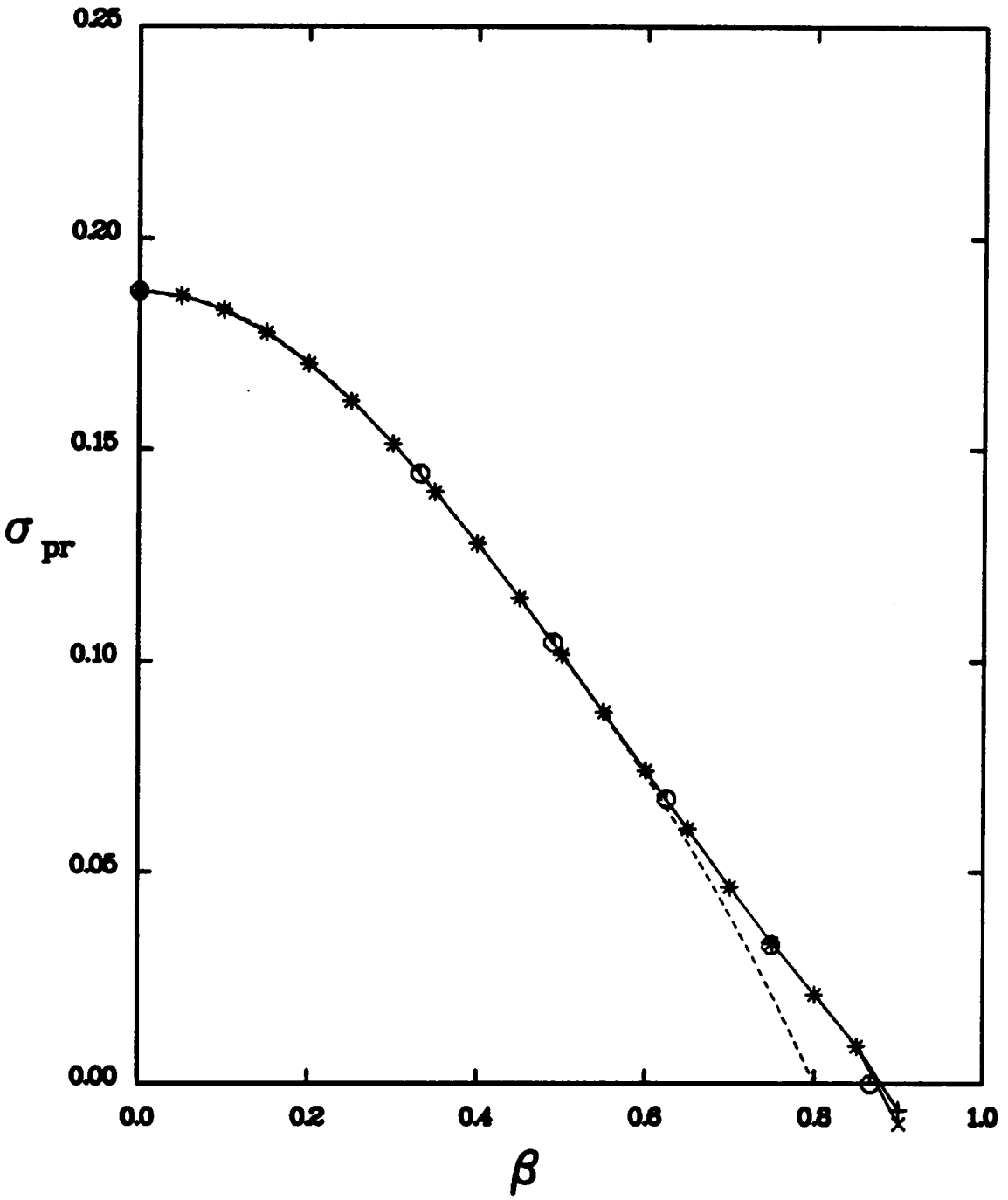

FIGURE 4.6 Growth rates of the inviscid TS as a function of β. Comparison with Michalke (o), Squires trans. (+), secondary instability (--) and direct (x). α = 0.5, JJ = 33 Yo=2.

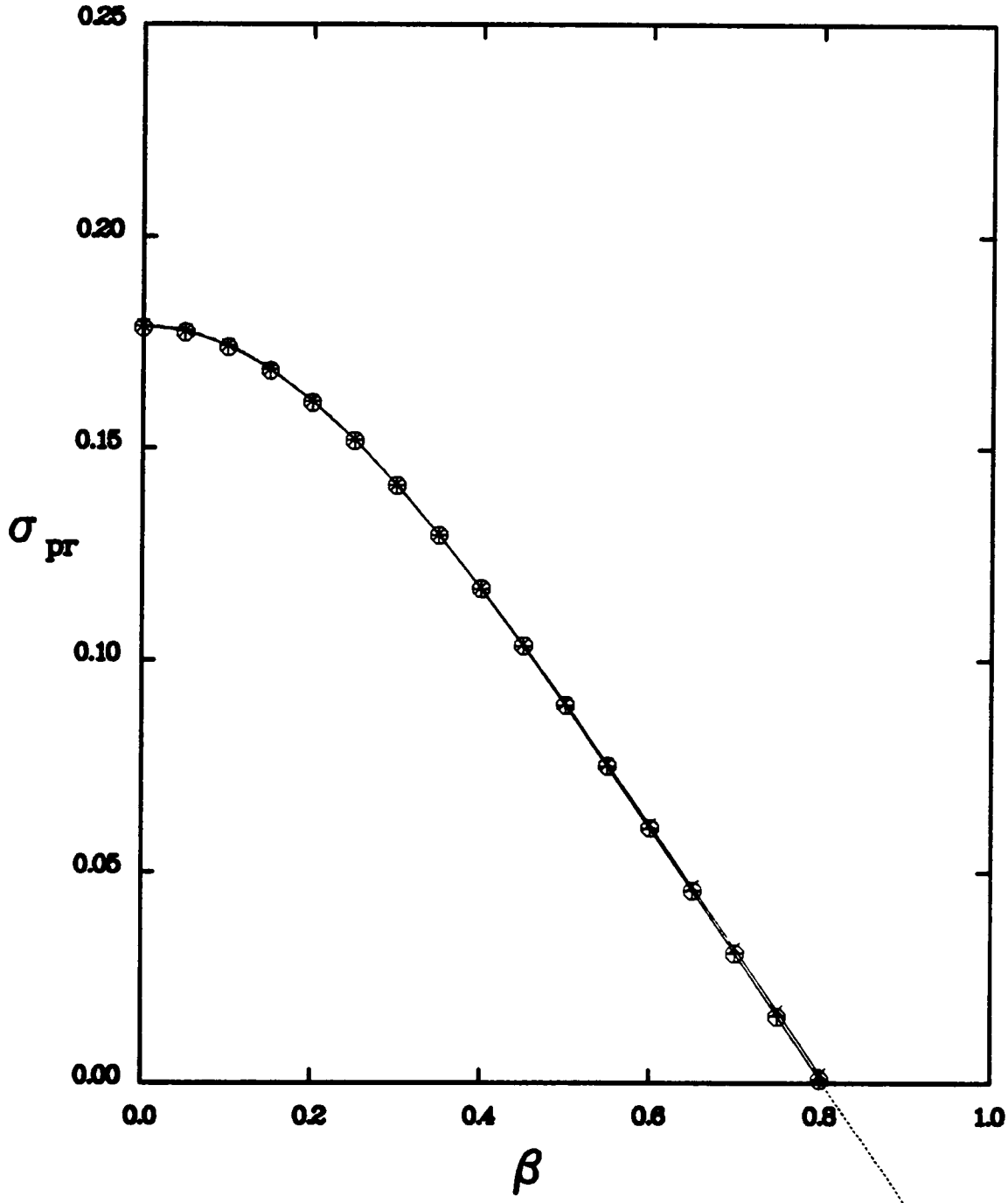

FIGURE 4.7 Growth rates of the TS as a function of β for ηo = 0.5 (o), 1 (+), 2 (--) and 4 (x) and secondary instability. Chebyshev polynomials α= 0.5, JJ = 32, R =200.

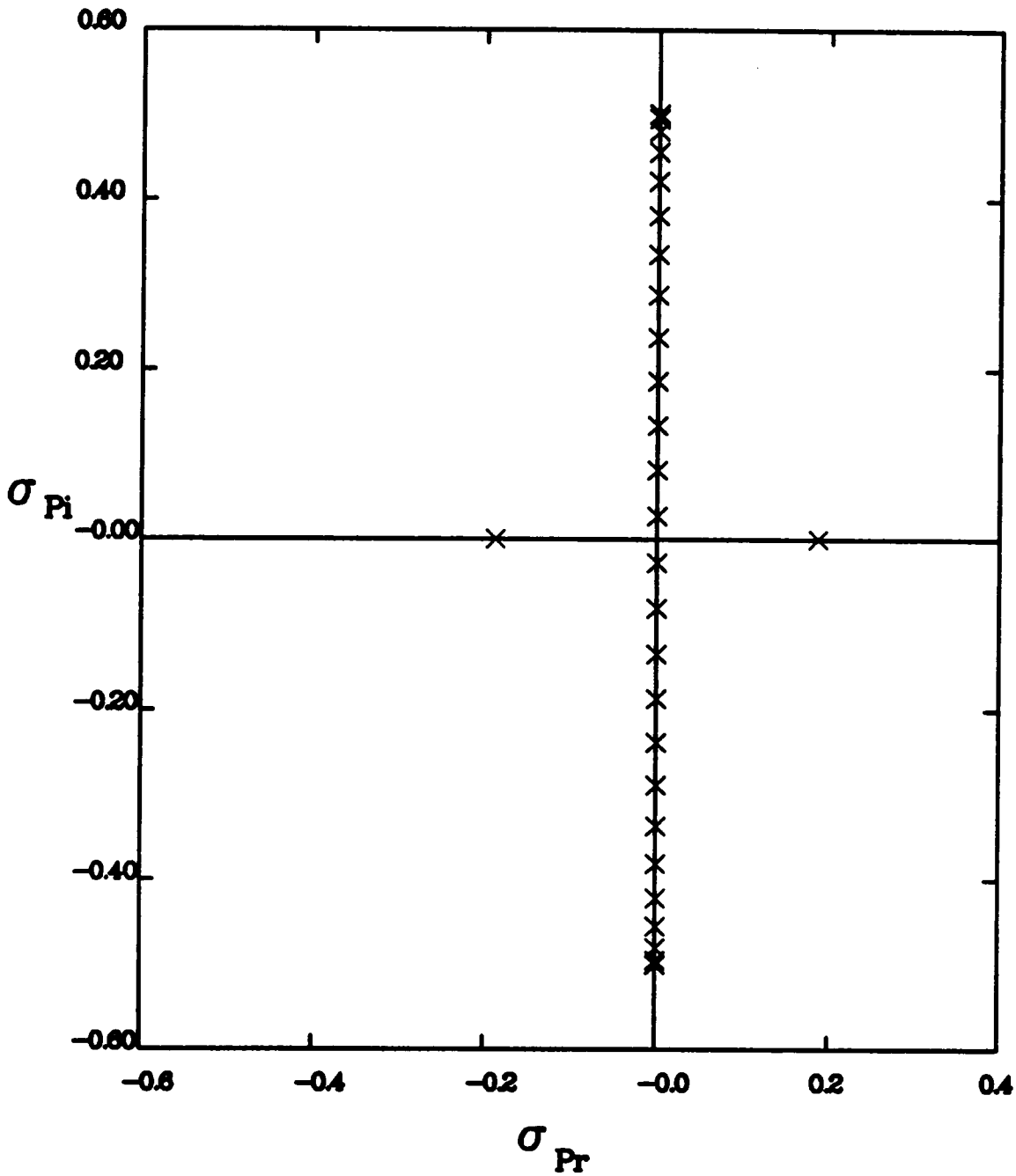

FIGURE 4.8 Spectrum of temporal eigenvalues of the Rayleigh equation using Chebyshev polynomials and the algebraic mapping. α = 0.5, JJ=32 and ηo = 1.0.

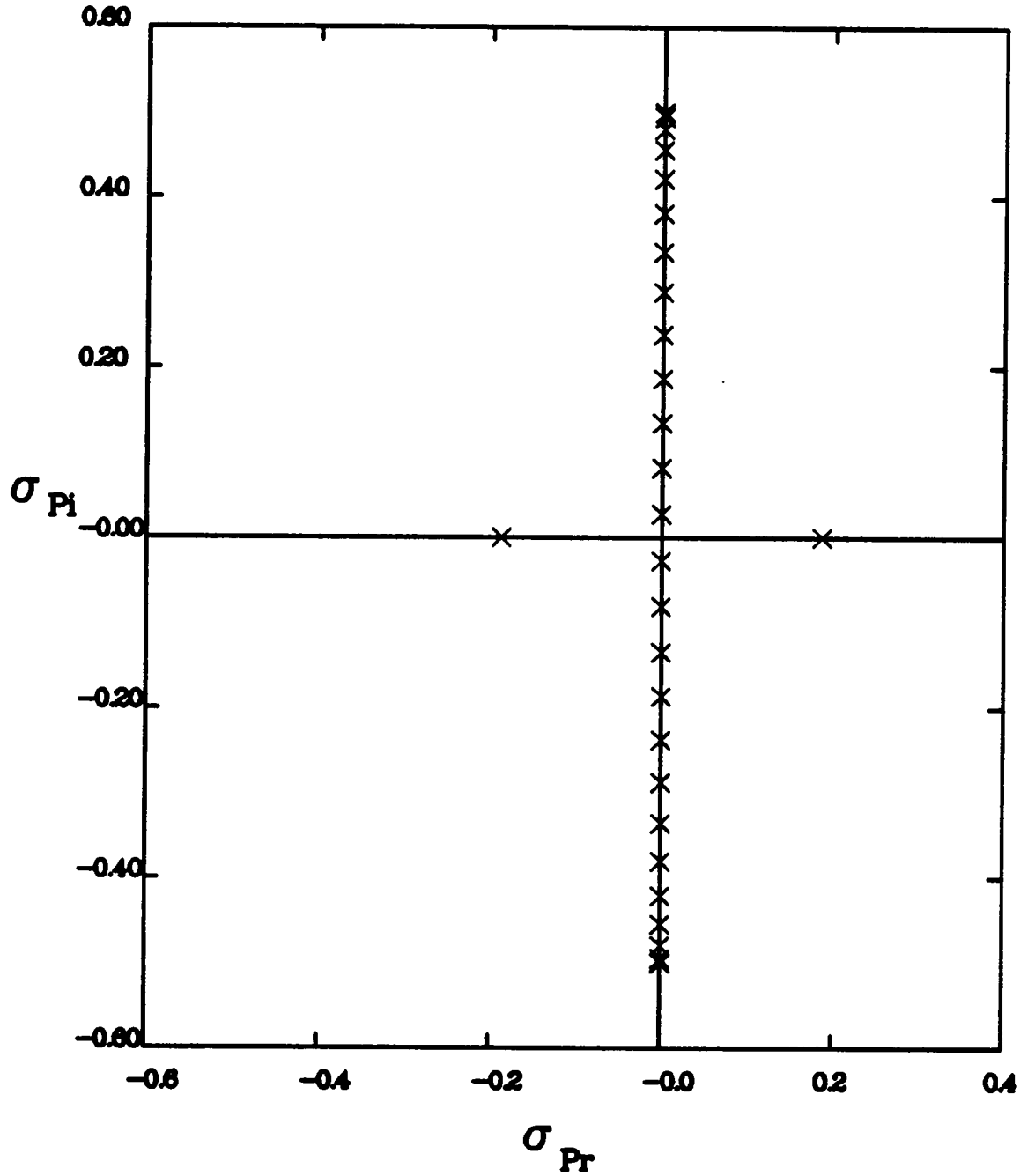

FIGURE 4.9 Spectrum of temporal eigenvalues of the OS equation using Chebyshev polynomials and the algebraic mapping. α = 0.5, JJ=32 and η_o = 1.0, R = 500000.

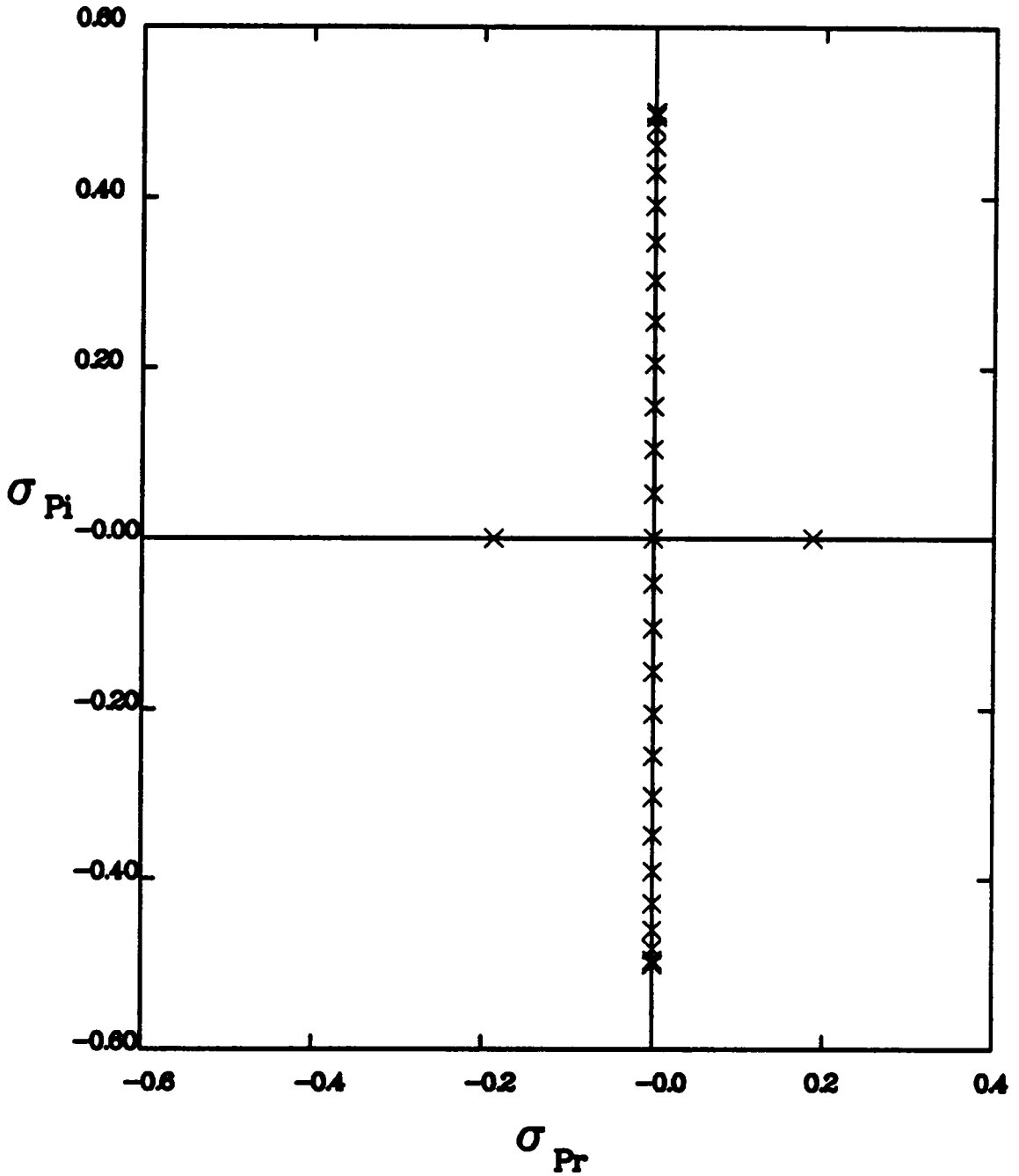

FIGURE 4.10 Spectrum of temporal eigenvalues of the OS equation using Chebyshev polynomials and the algebraic mapping. α = 0.5, JJ=33 and ηo = 1.0, R = 500000.

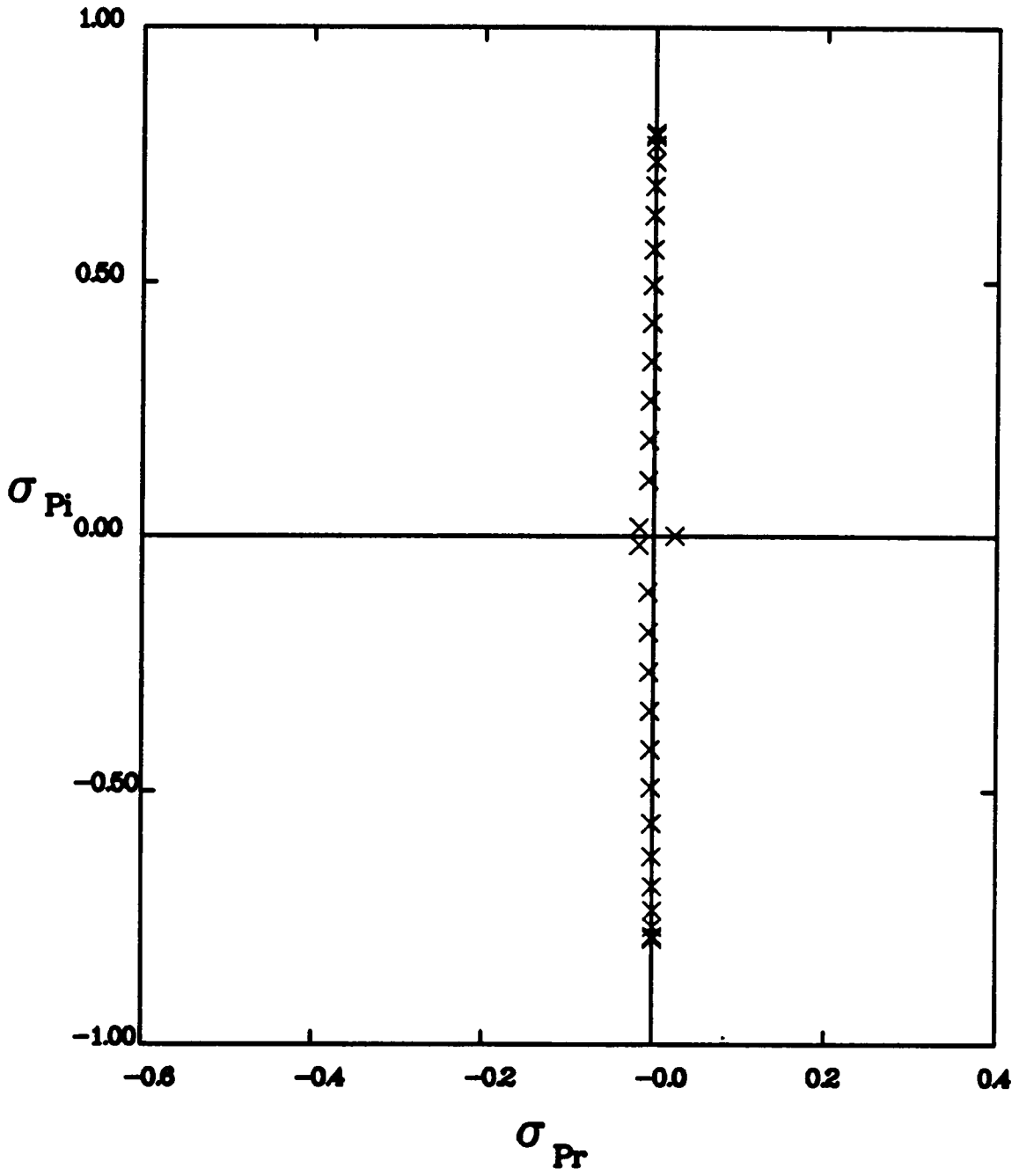

FIGURE 4.11 Spectrum of temporal eigenvalues of the OS equation using Chebyshev polynomials and the algebraic mapping. α = 0.95, JJ=33 and ηo = 1.0, R = 500000.

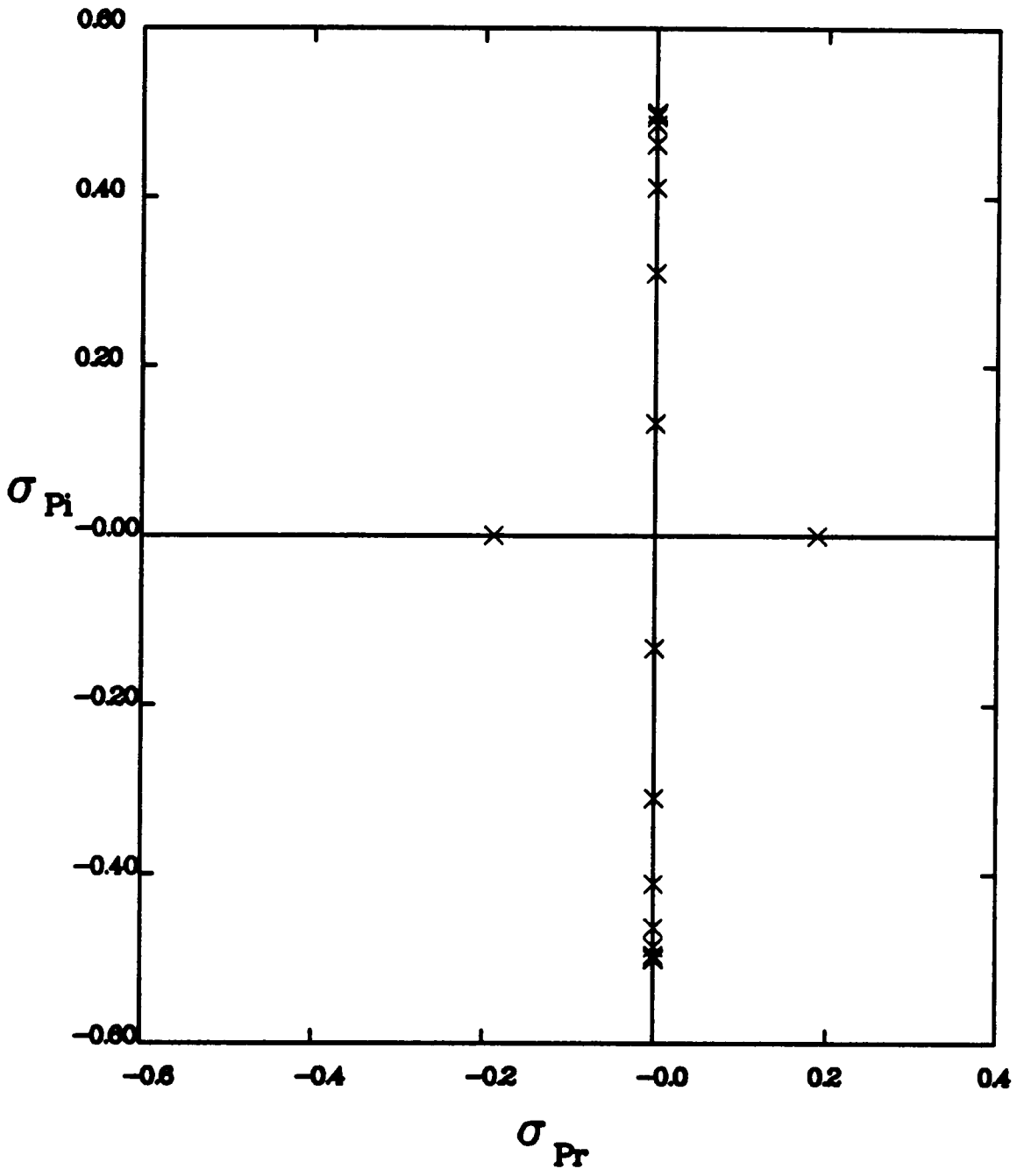

FIGURE 4.12 Spectrum of temporal eigenvalues of the OS equation using Chebyshev polynomials and the algebraic mapping. α = 0.5, JJ=32 and ηo = 4.0, R = 500000.

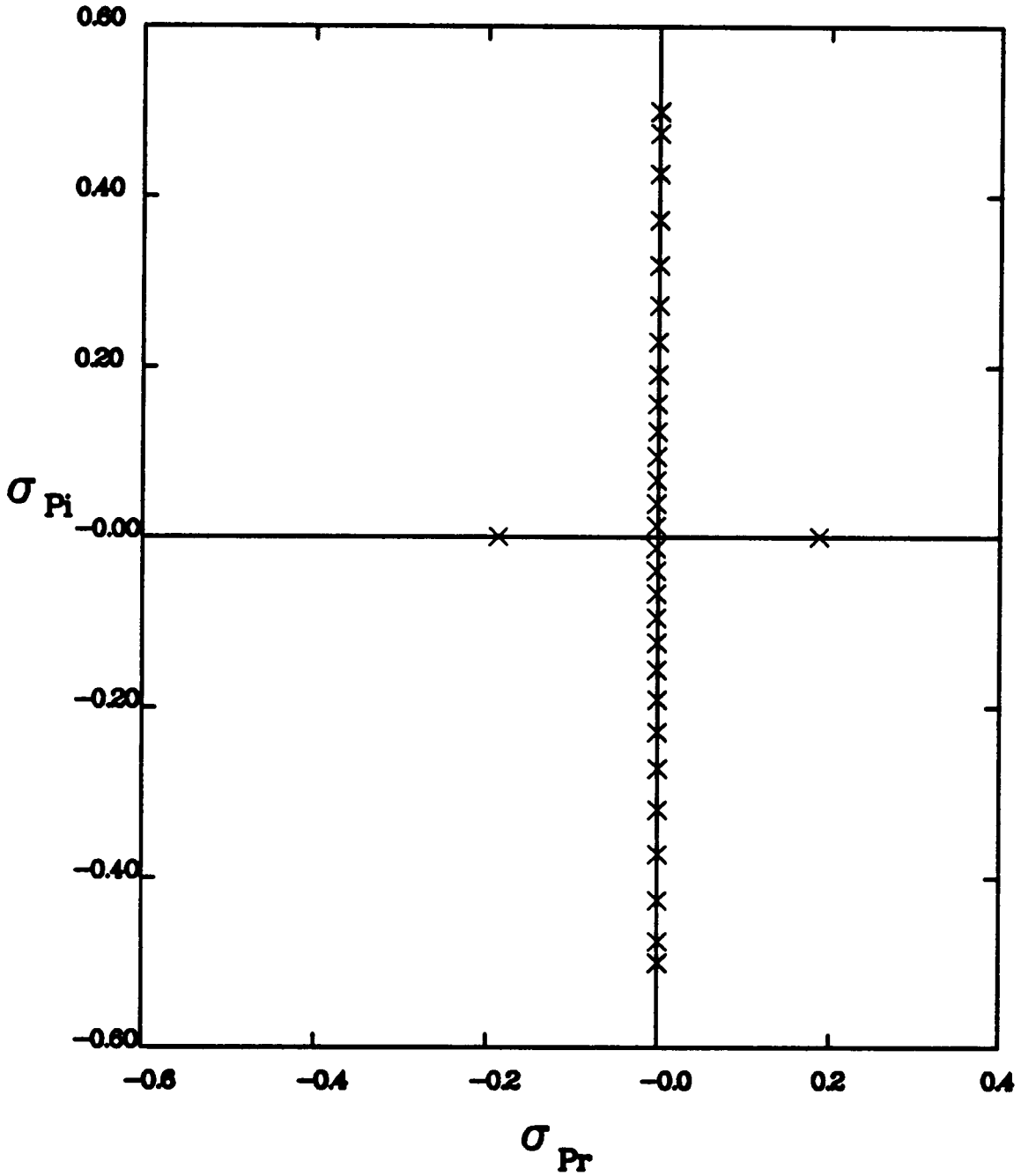

FIGURE 4.13 Spectrum of temporal eigenvalues of the OS equation using Chebyshev polynomials and the algebraic mapping. α = 0.5, JJ=32 and ηo = 0.5, R = 500000.

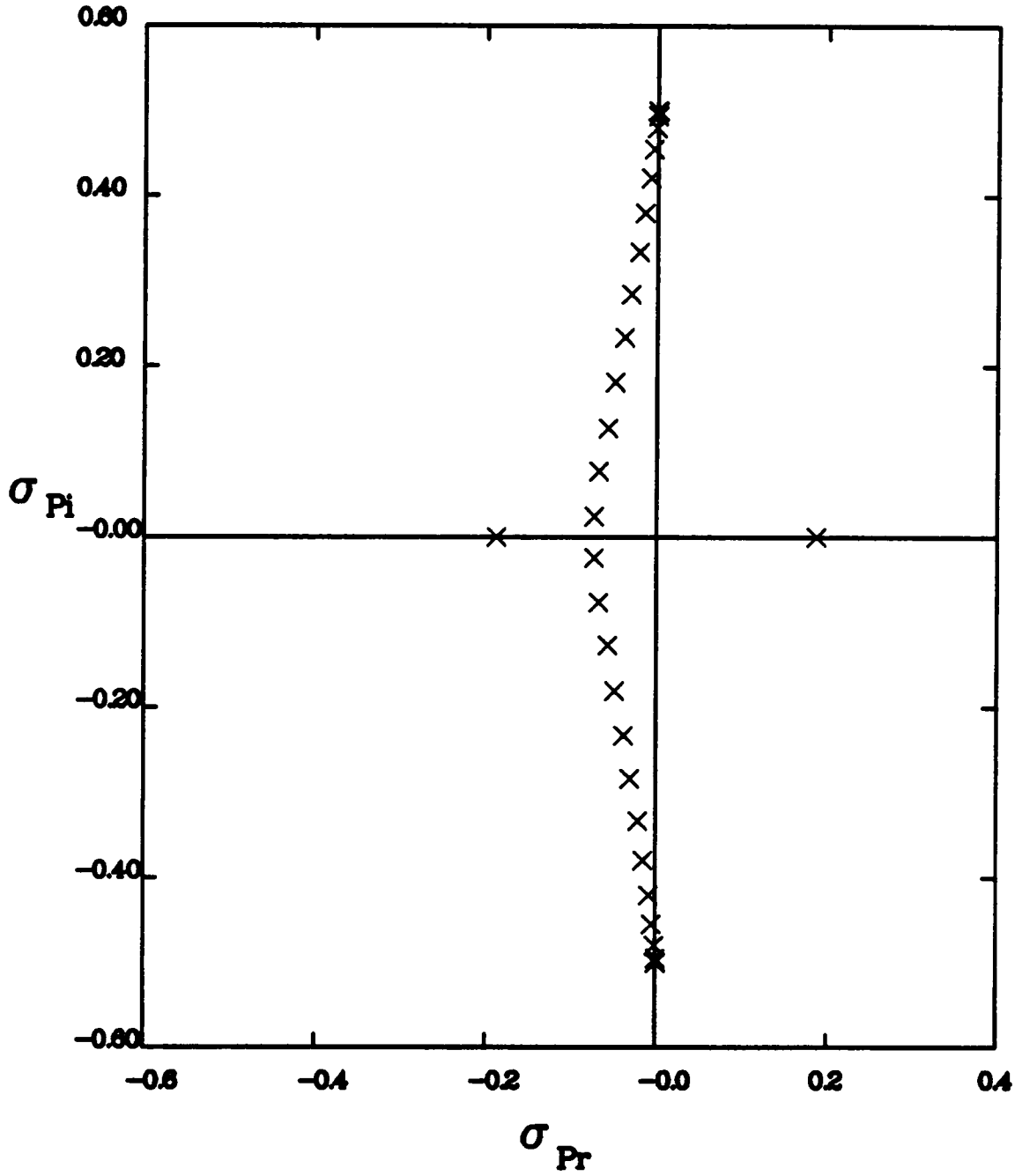

FIGURE 4.14 Spectrum of temporal eigenvalues of the OS equation using Chebyshev polynomials and the algebraic mapping. α = 0.5, JJ=32 and ηo = 1.0, R = 5000.

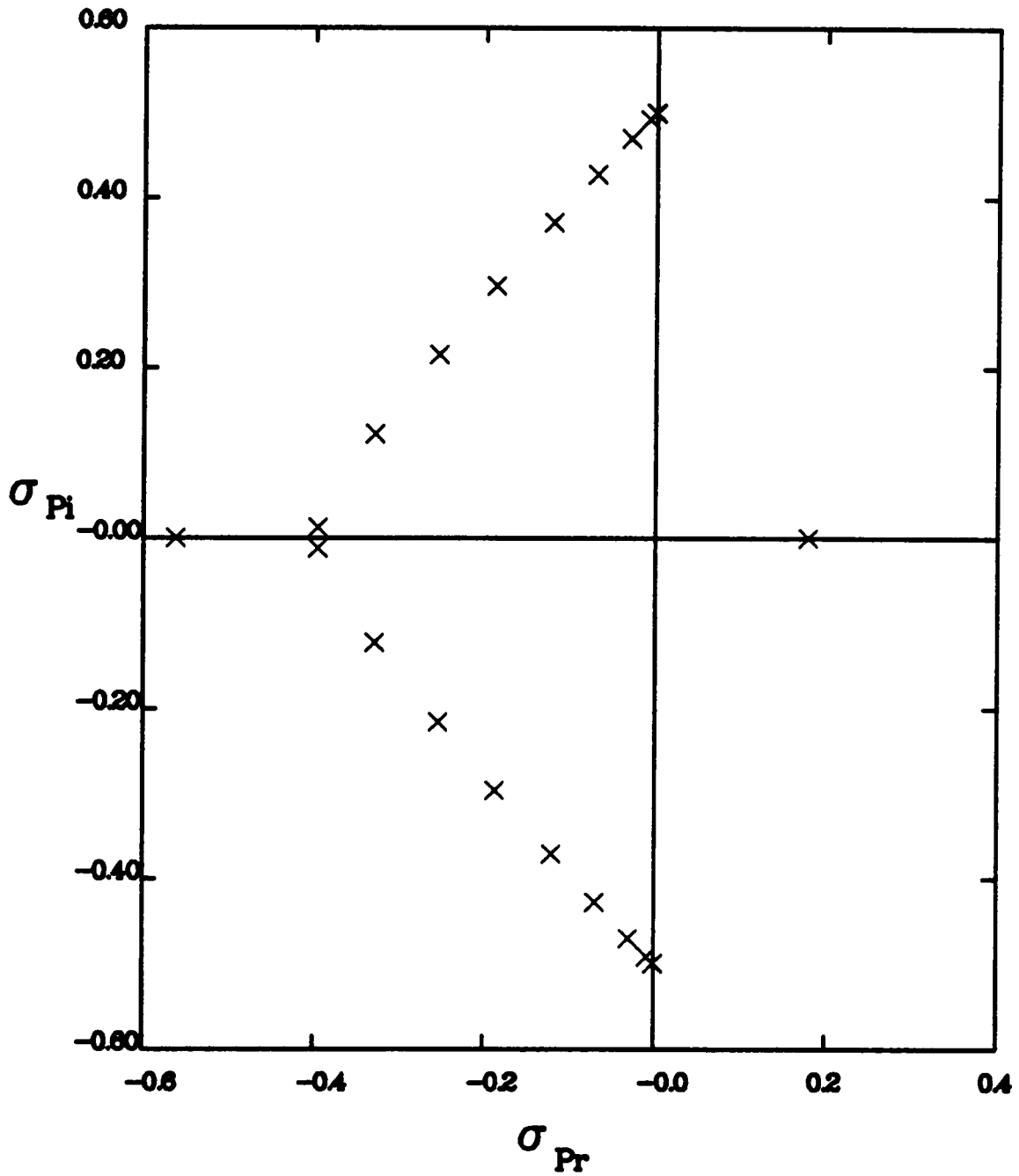

FIGURE 4.15 Spectrum of temporal eigenvalues of the OS equation using Chebyshev polynomials and the algebraic mapping. α = 0.5, JJ=32 and η o = 1.0, R = 200.

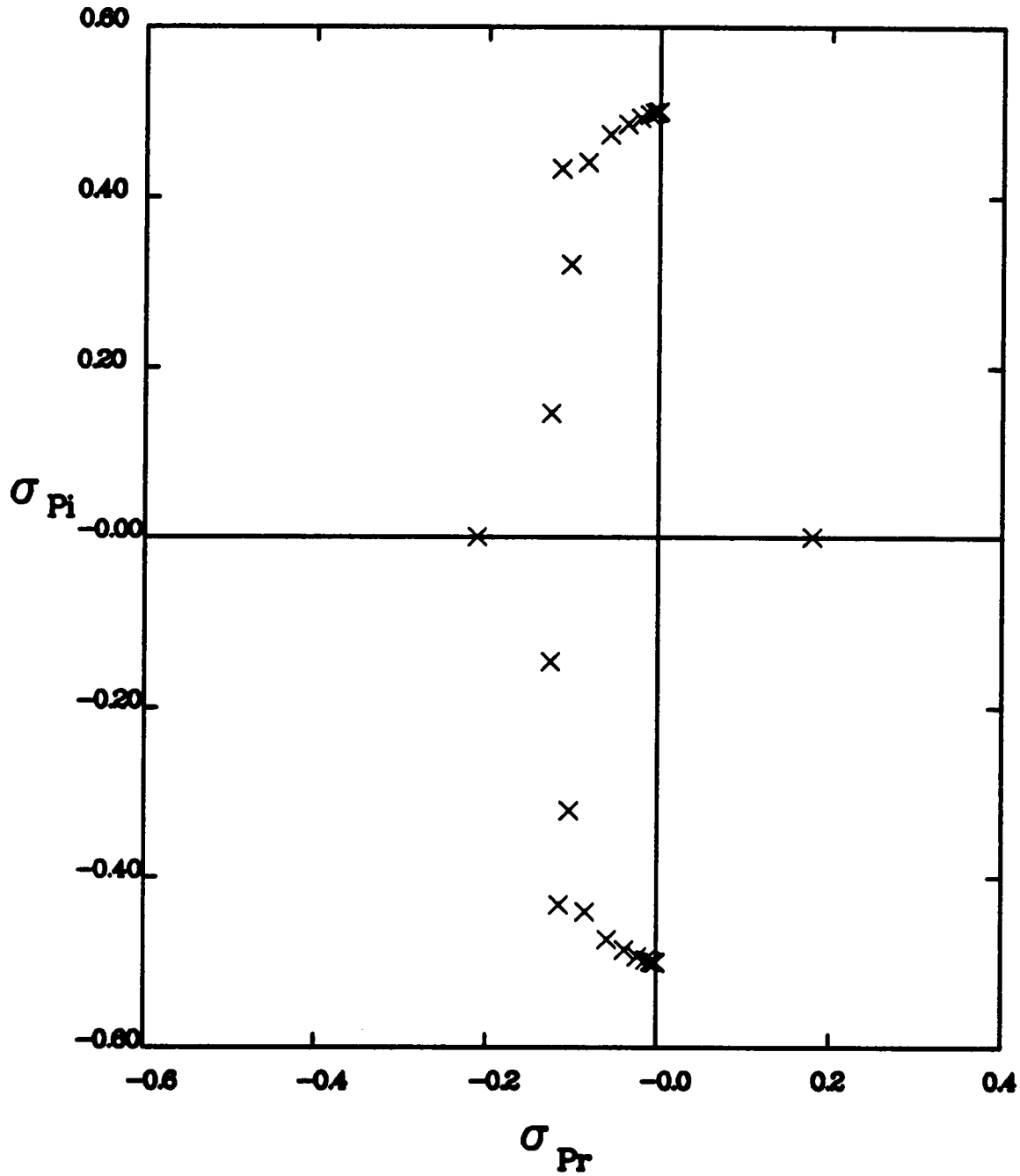

FIGURE 4.16 Spectrum of temporal eigenvalues of the OS equation using Chebyshev polynomials and the algebraic mapping. α = 0.5, JJ=32 and ηo = 4.0, R = 200.

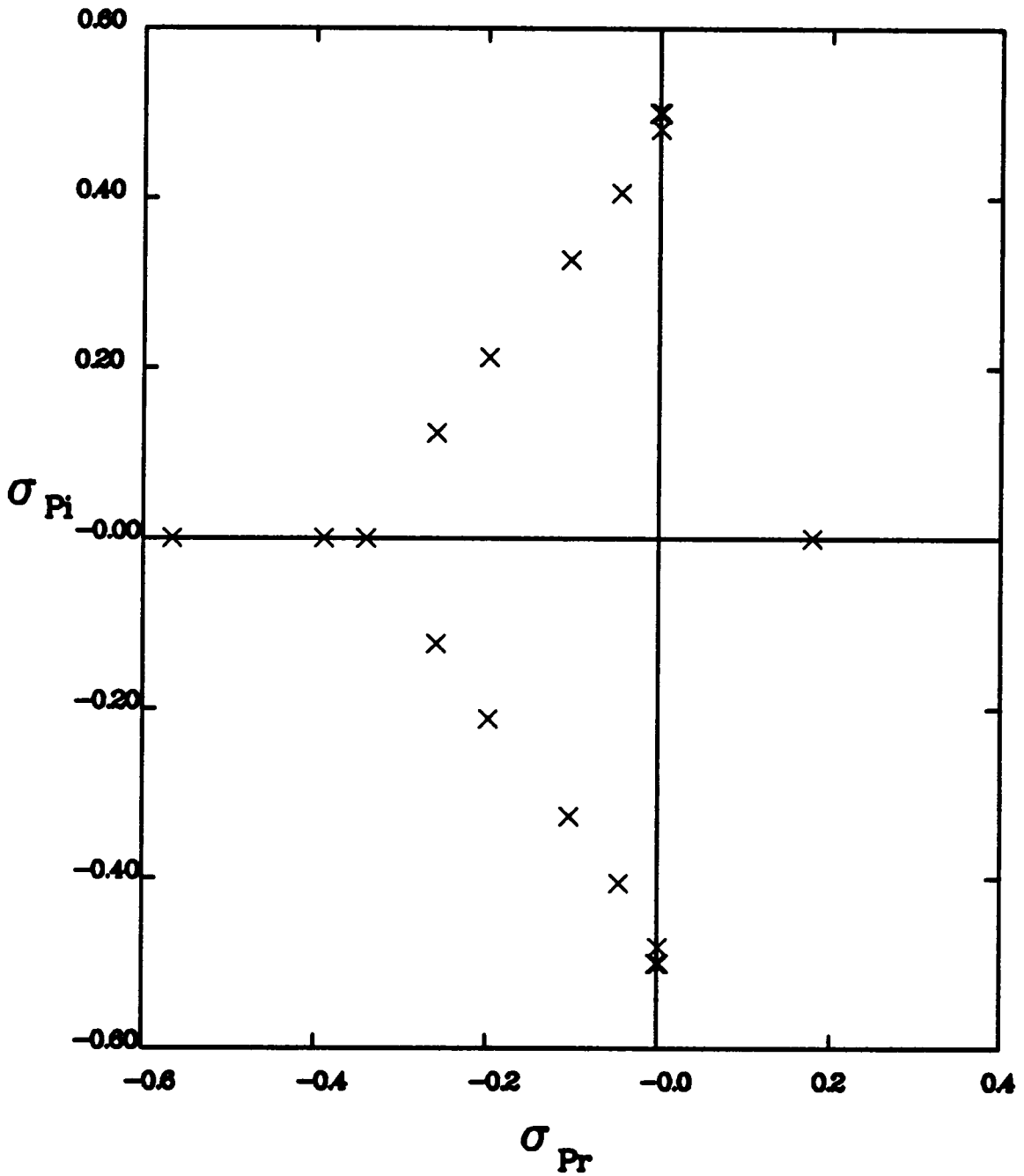

FIGURE 4.17 Spectrum of temporal eigenvalues of the OS equation using Chebyshev polynomials and the algebraic mapping. α = 0.5, JJ=32 and η o = 0.5, R = 200.

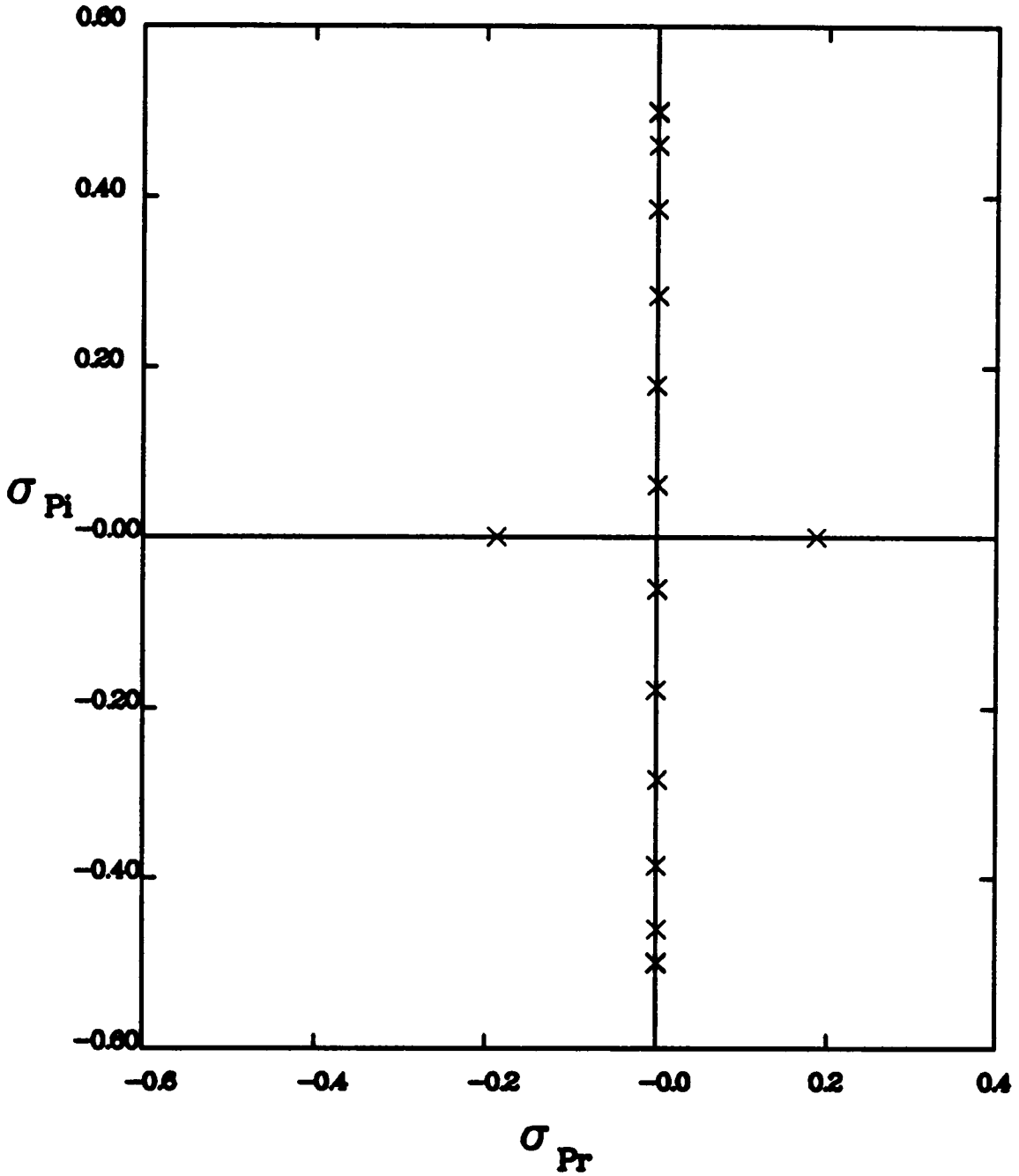

FIGURE 4.18 Spectrum of temporal eigenvalues of the Rayleigh equation using Fourier series and the trigonometric mapping. α = 0.5, JJ=16 and ηo = 1.0, R = 200.

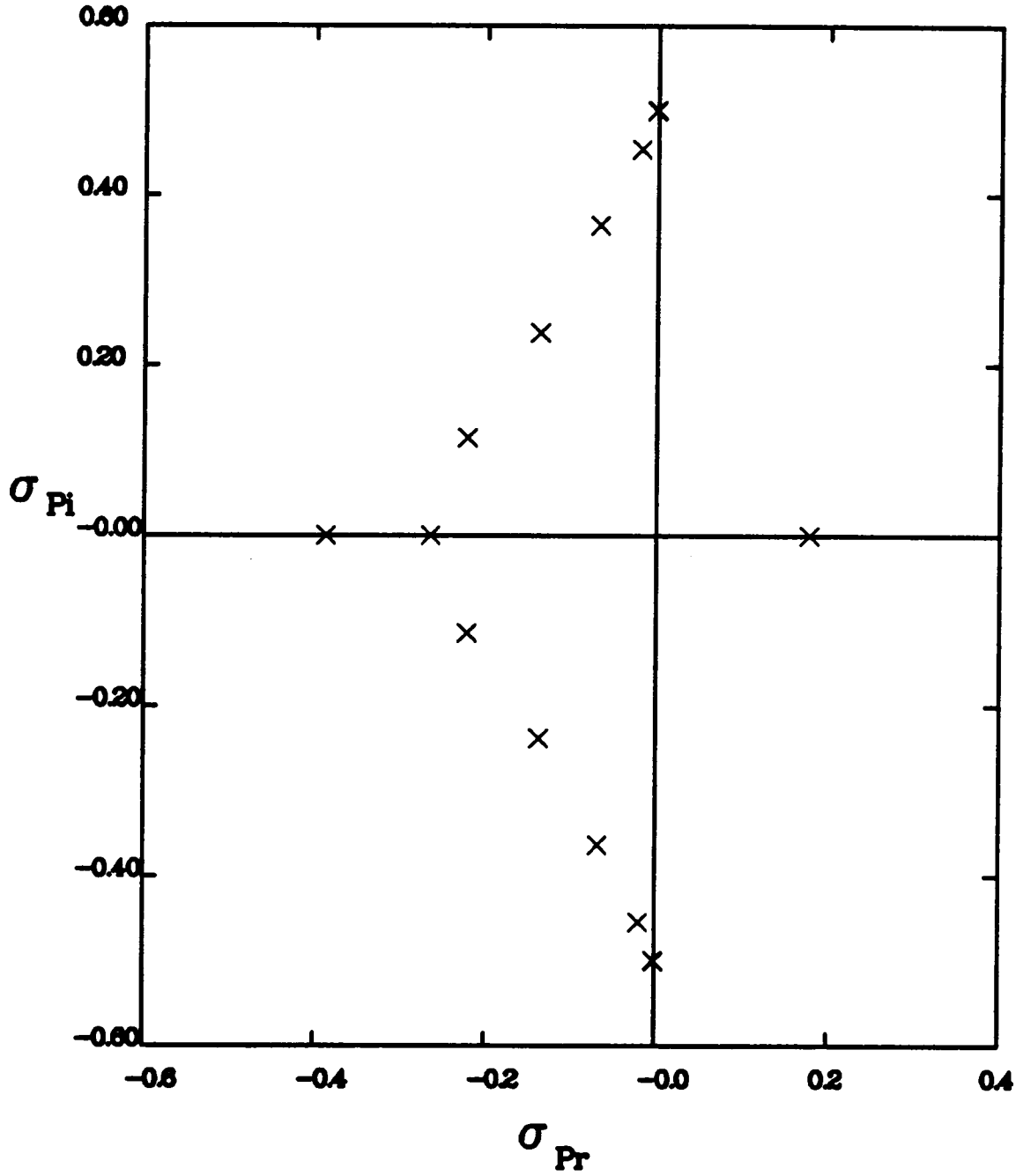

FIGURE 4.19 Spectrum of temporal eigenvalues of the OS equation using Fourier series and the trigonometric mapping. α = 0.5, JJ=16 and ηo = 1.0, R = 200.

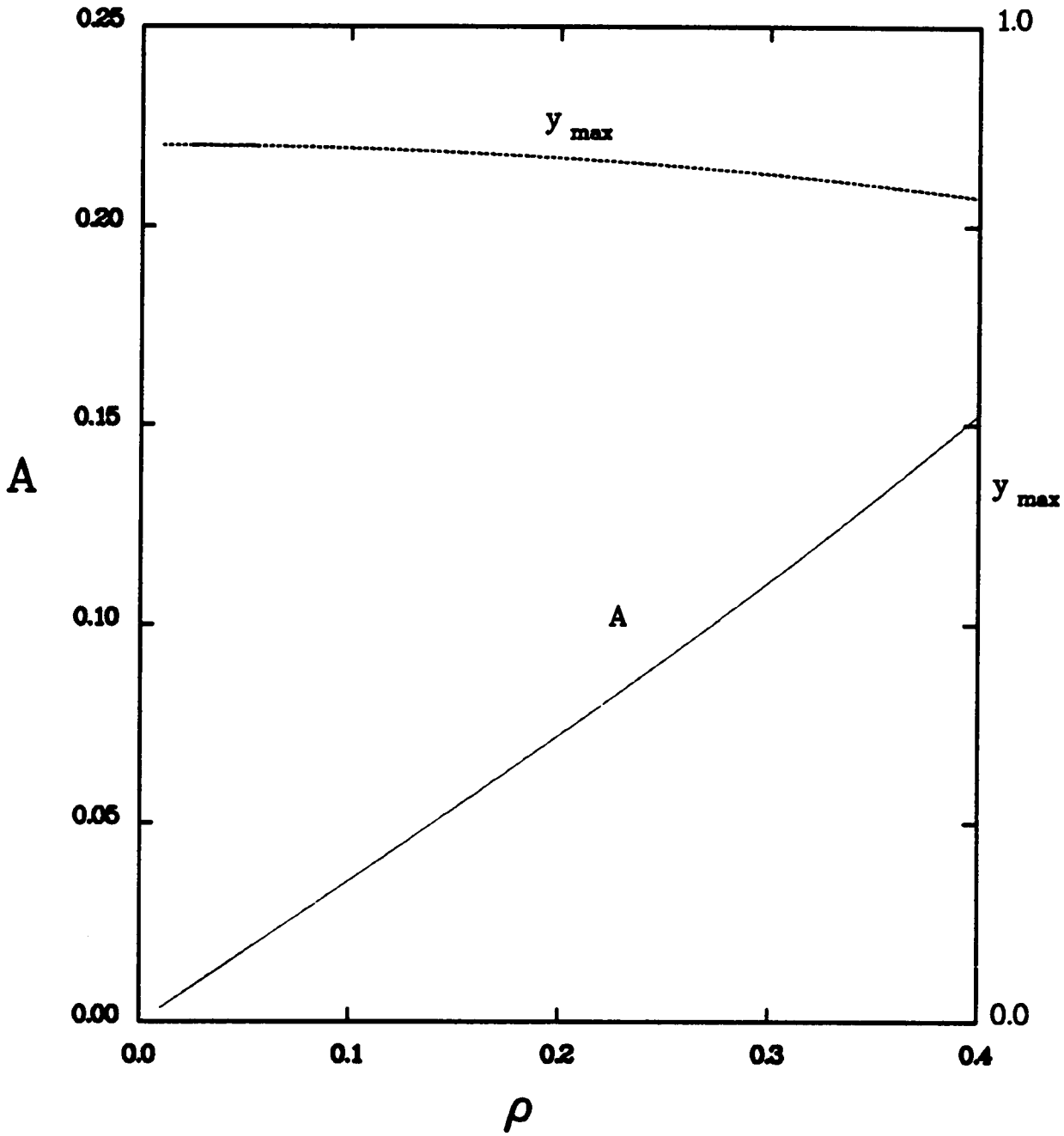

FIGURE 4.20 Maximum rms amplitude and its y-location for Stuart vortices as a function of the amplitude parameter ρ.

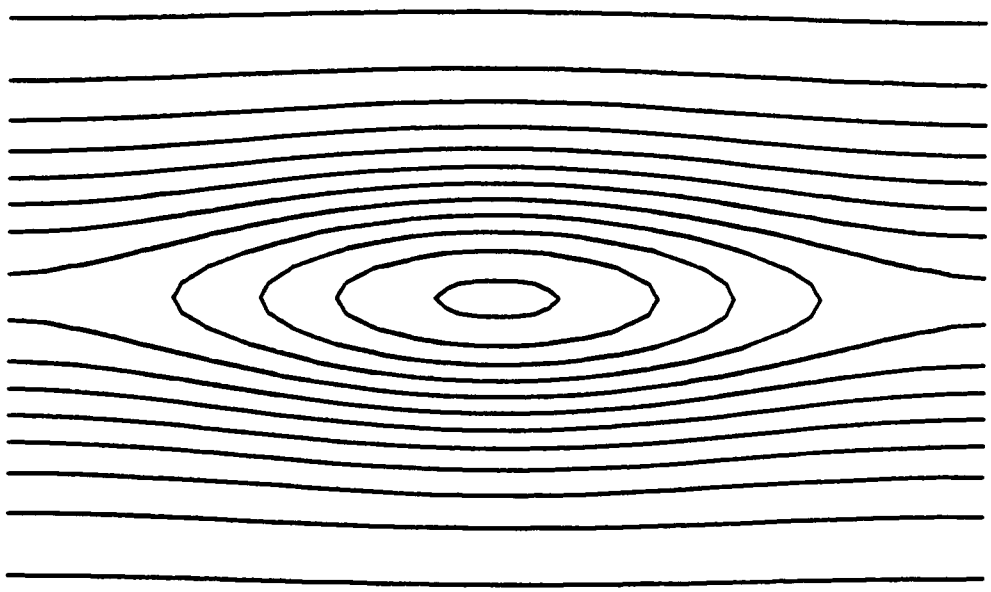

FIGURE 4.21 Contour plot of the vorticity field for the Stuart vortices with ρ = 0.10. The minimum level is −1.7 and difference in levels is 0.10.

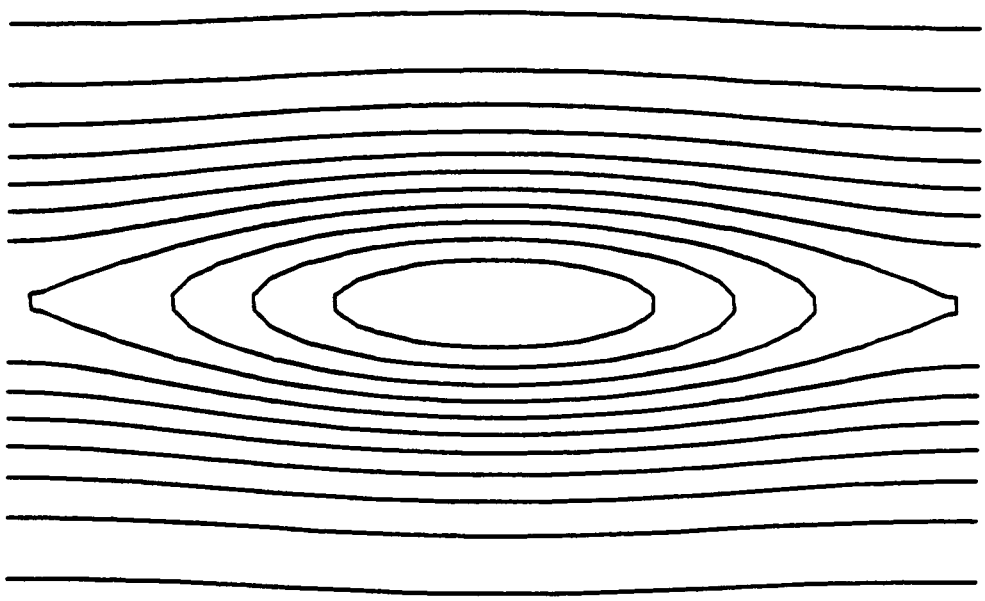

FIGURE 4.22 Contour plot of the vorticity field of the inviscid neutral TS wave with A=0.0355. The minimum level is −1.7 and difference in levels is 0.10.

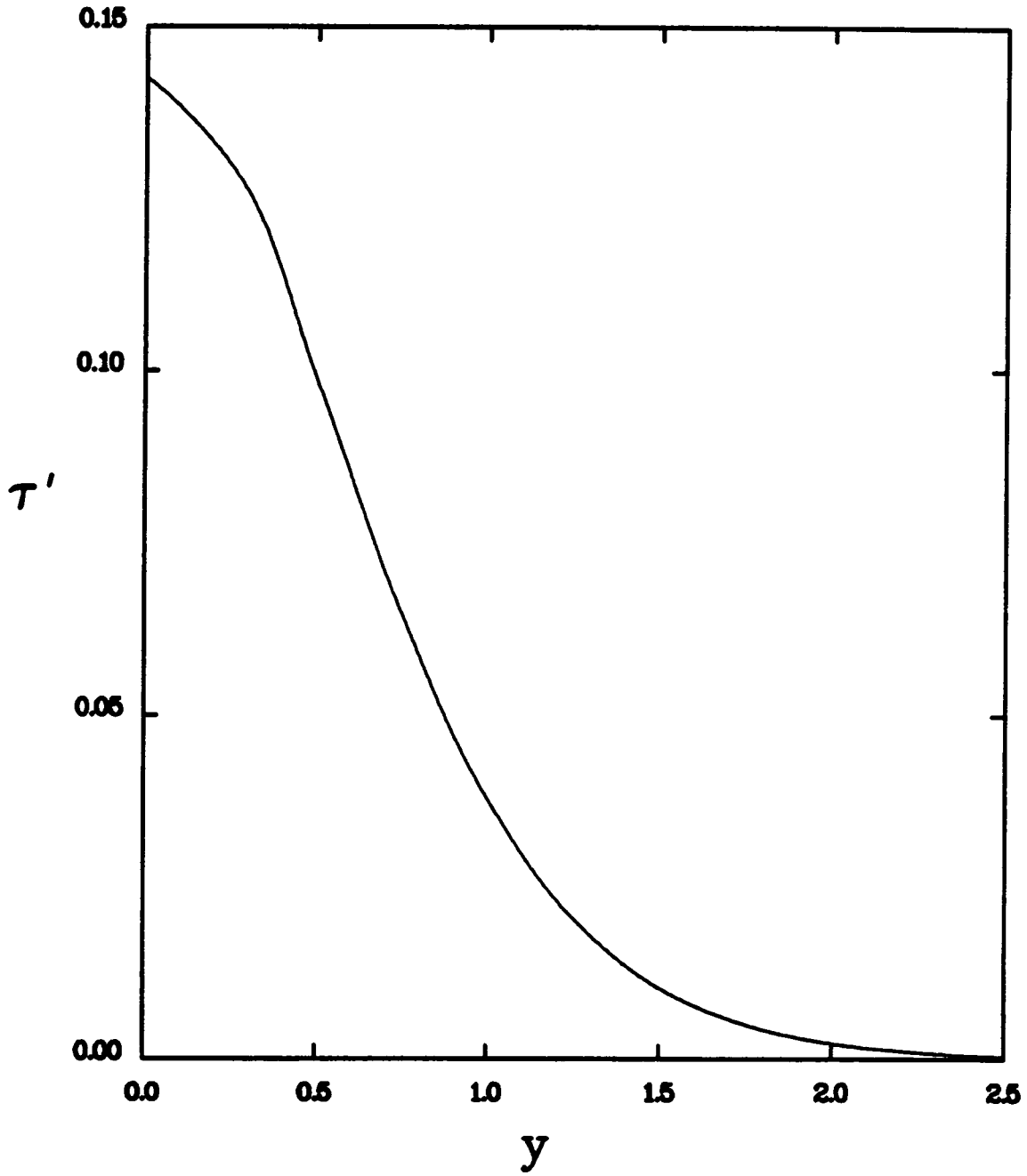

FIGURE 4.23 Distribution of the rms vorticity amplitude across the shear layer of Stuart vortices with ρ = 0.1.

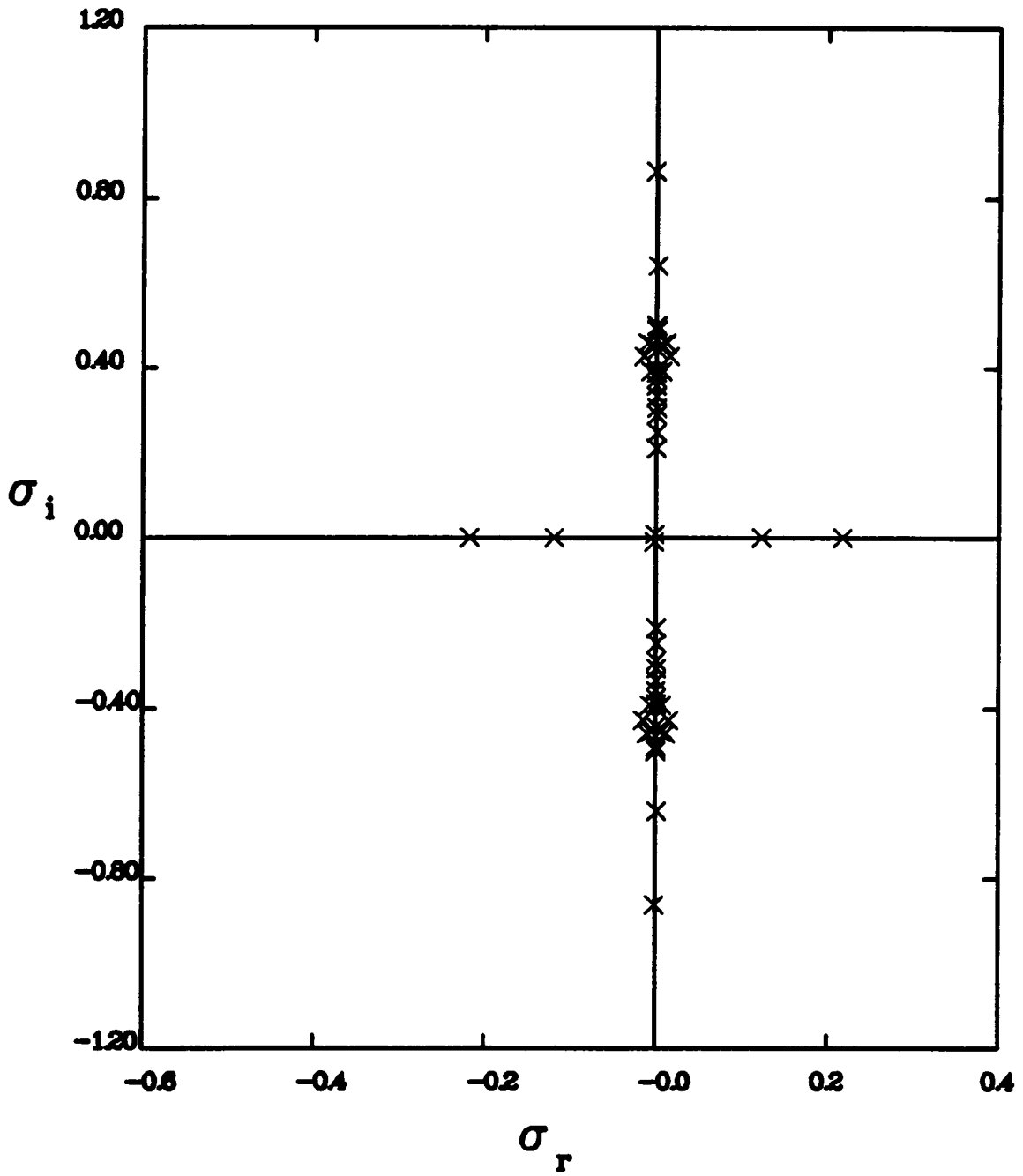

FIGURE 4.24 Spectrum of temporal eigenvalues of the subharmonic mode using Chebyshev polynomials. α = 1.00, JJ = 16 and ηo = 1.0, R = inf, β = 0.

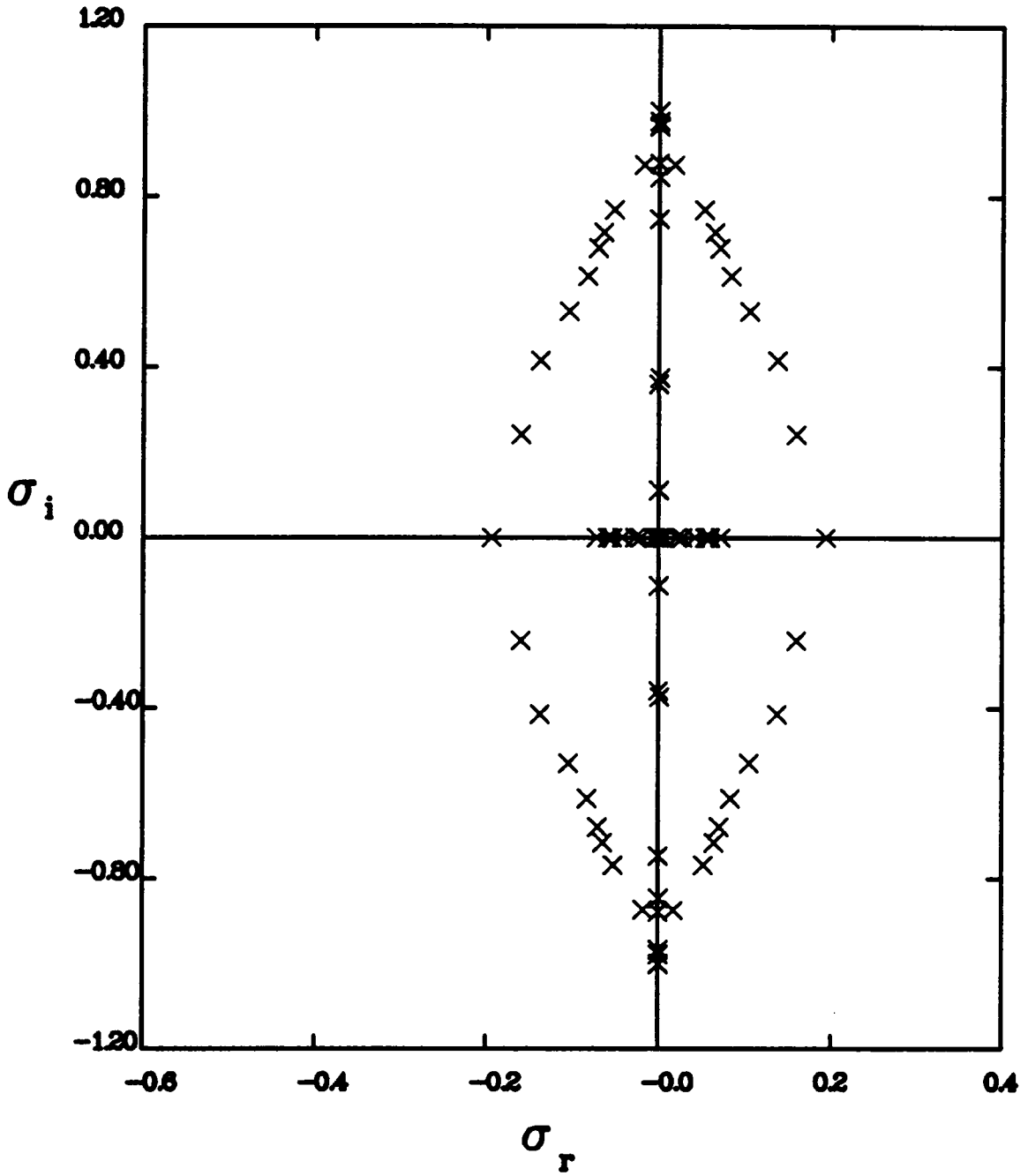

FIGURE 4.25 Spectrum of temporal eigenvalues of the fundamental mode using Chebyshev polynomials.
α = 1.00, JJ = 16 and ηo = 1.0, R = inf, β = 2.

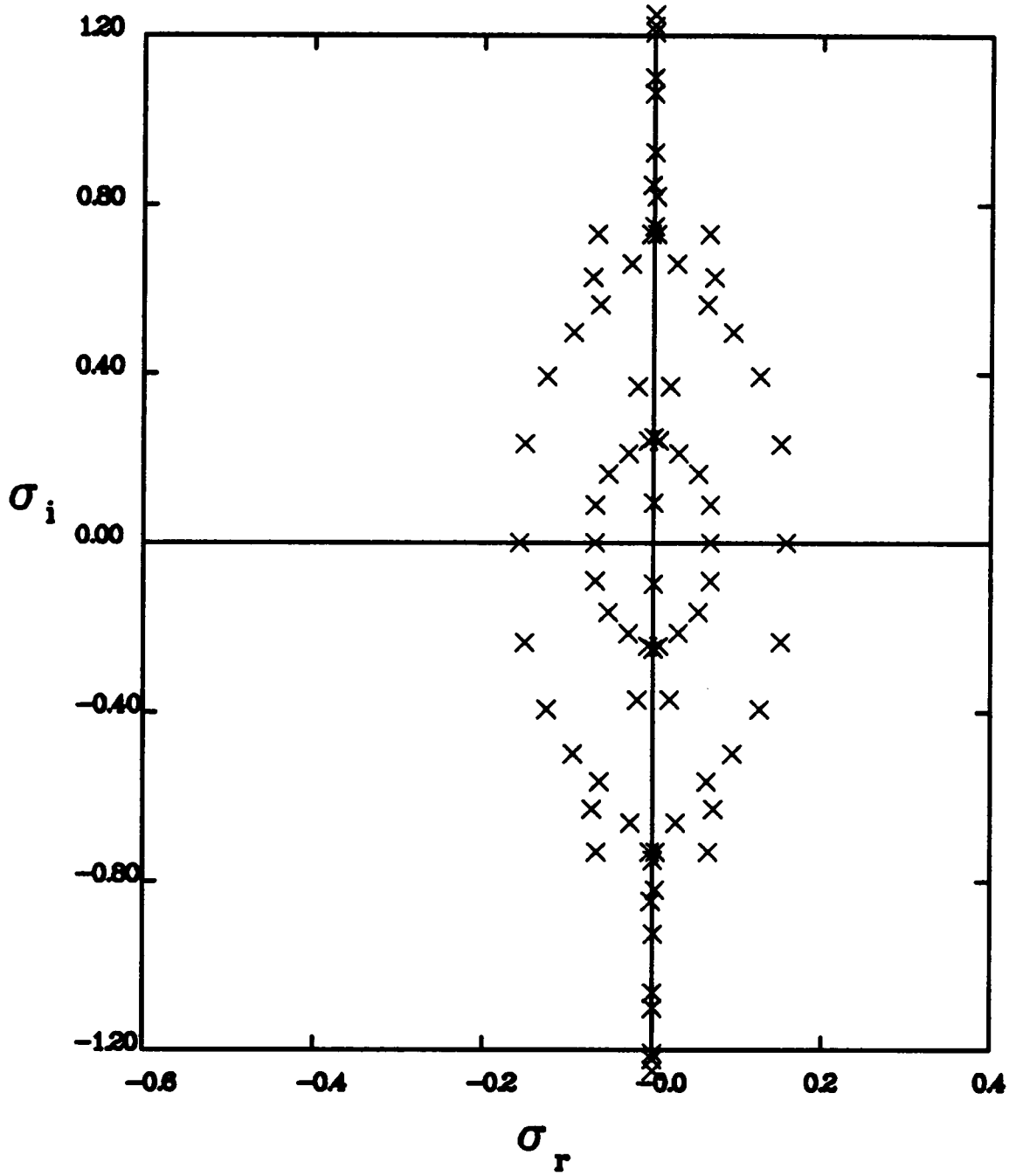

FIGURE 4.26 Spectrum of temporal eigenvalues of the detuned mode with ε = 0.5 using Chebyshev polynomials.
α = 1.00, JJ = 16 and ηo = 1.0, R = inf, β = 2.

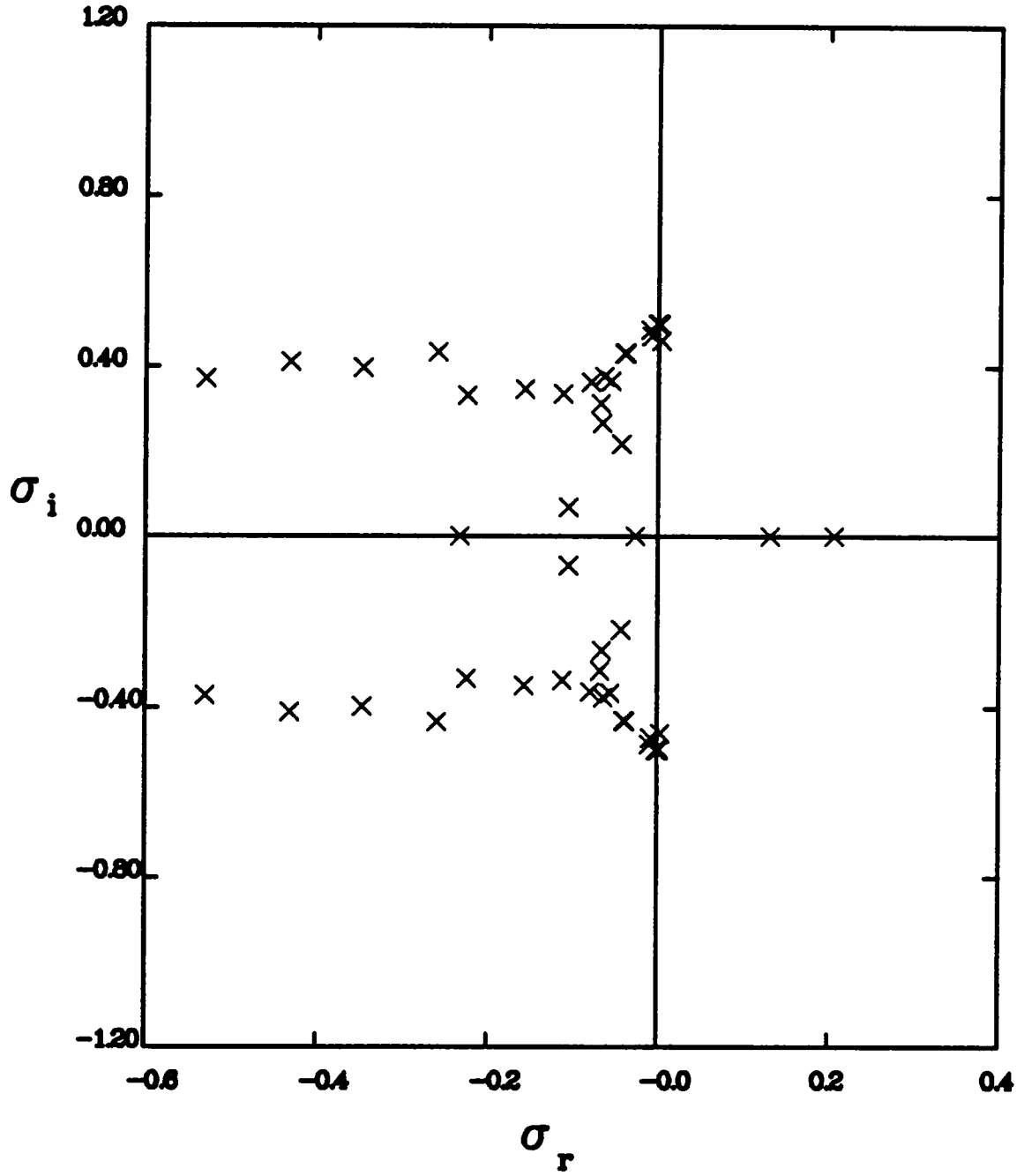

FIGURE 4.27 Spectrum of temporal eigenvalues of the subharmonic mode using Chebyshev polynomials. α = 1.00, JJ = 16 and ηo = 1.0, R = 200, β = 0.

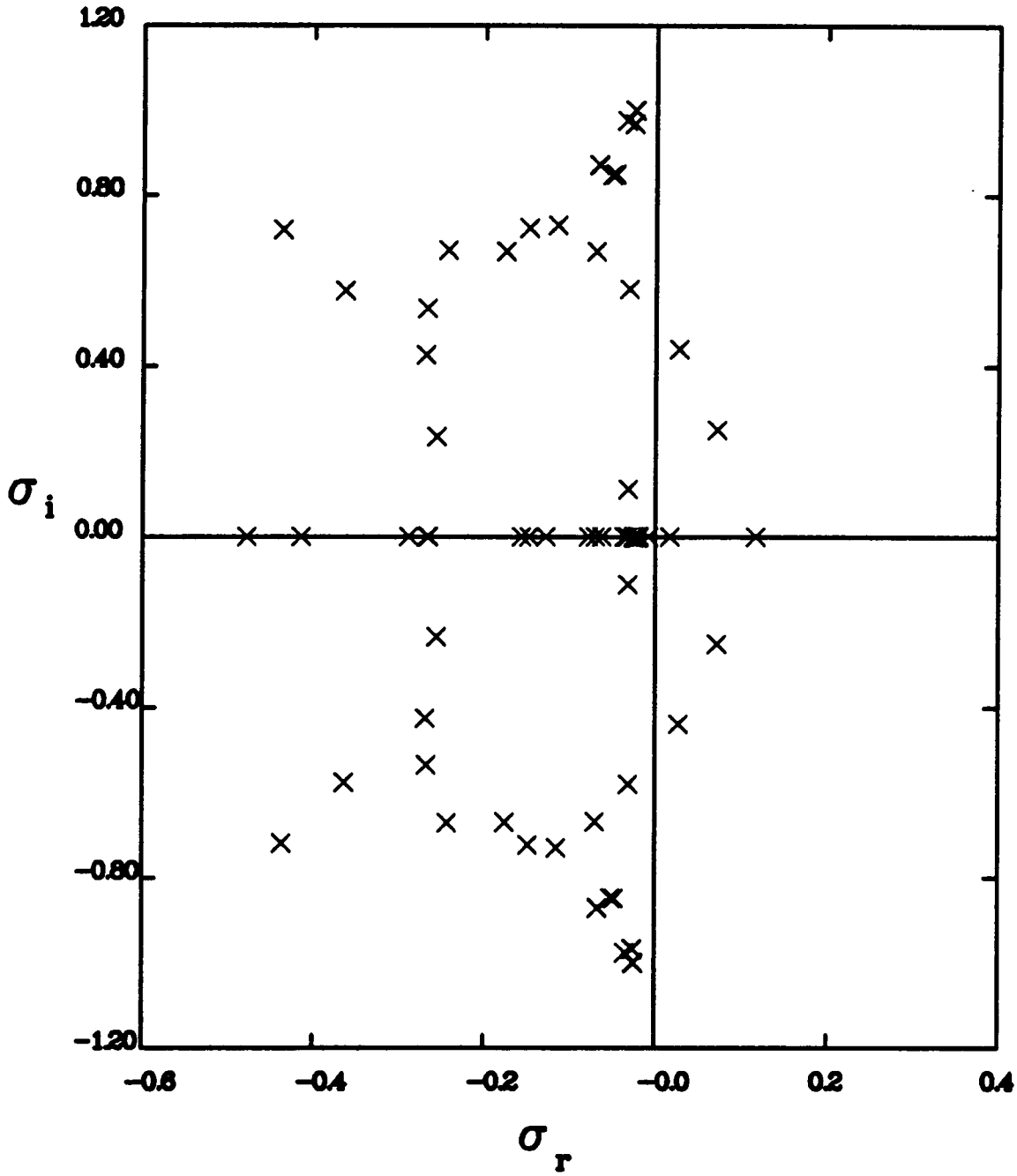

FIGURE 4.28 Spectrum of temporal eigenvalues of the fundamental mode using Chebyshev polynomials. α = 1.00, JJ = 16 and ηo = 1.0, R = 200, β = 2.

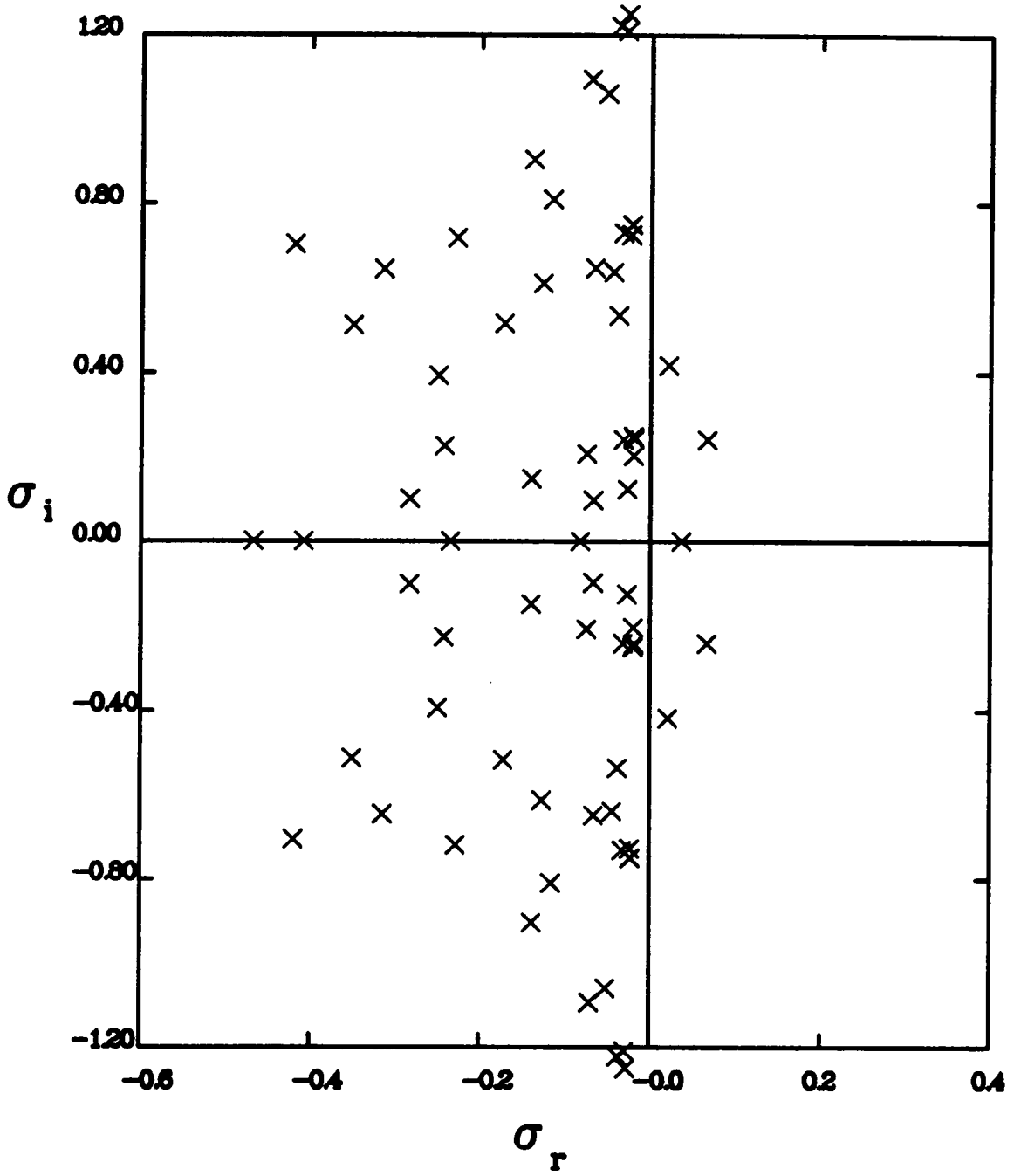

FIGURE 4.29 Spectrum of temporal eigenvalues of the detuned mode with ε = 0.5 using Chebyshev polynomials.
α = 1.00, JJ = 16 and ηo = 1.0, R = 200, β = 2.

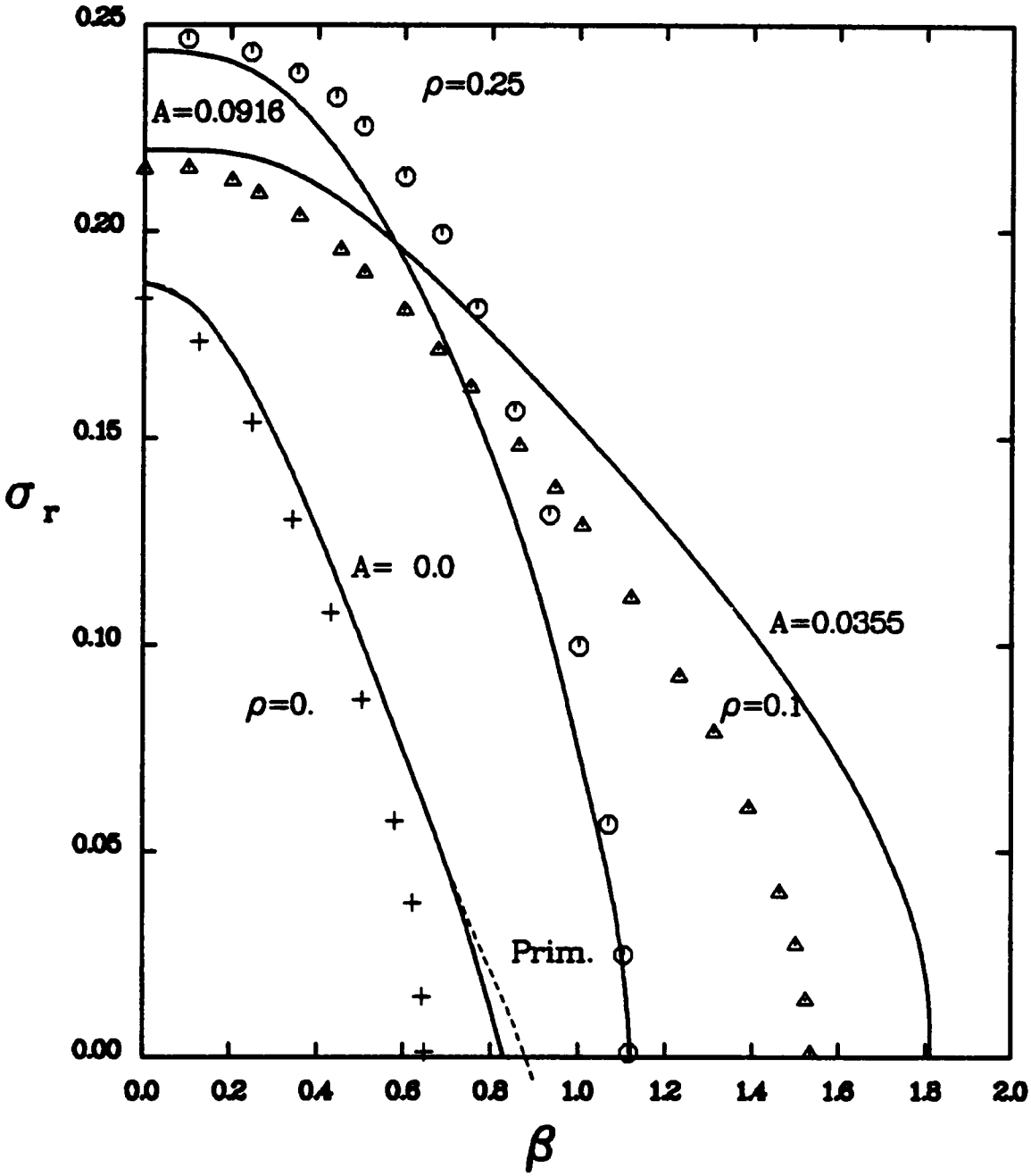

FIGURE 4.30 Growth rates of the subharmonic mode as a funct of the spanwise wavenumber for various amplitudes of the TS. Comparison with Pierrehumbert.

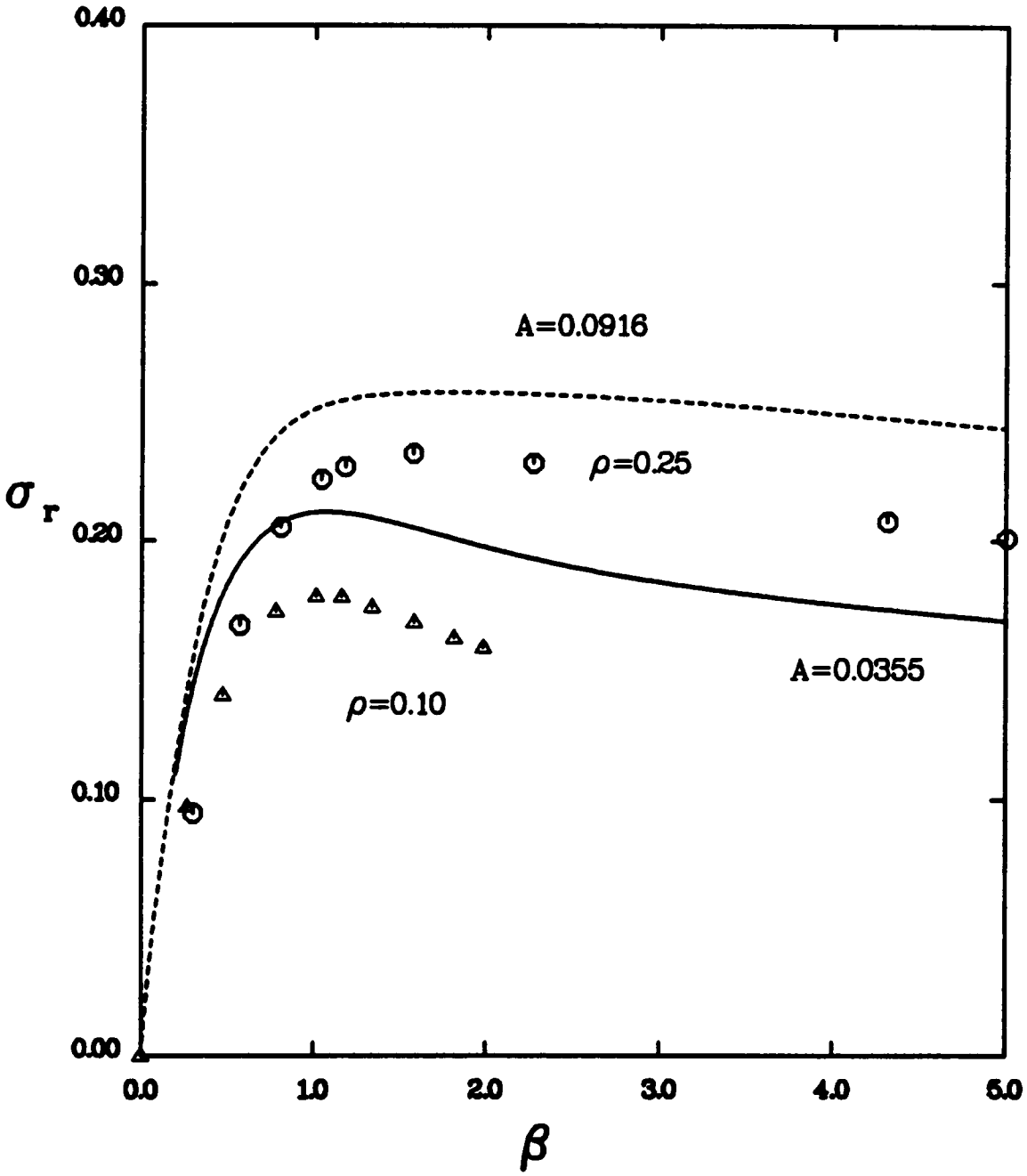

FIGURE 4.31 Growth rates of the fundamental mode as a function of the spanwise wavenumber for various amplitudes of the TS. Comparison with Pierrehumbert.

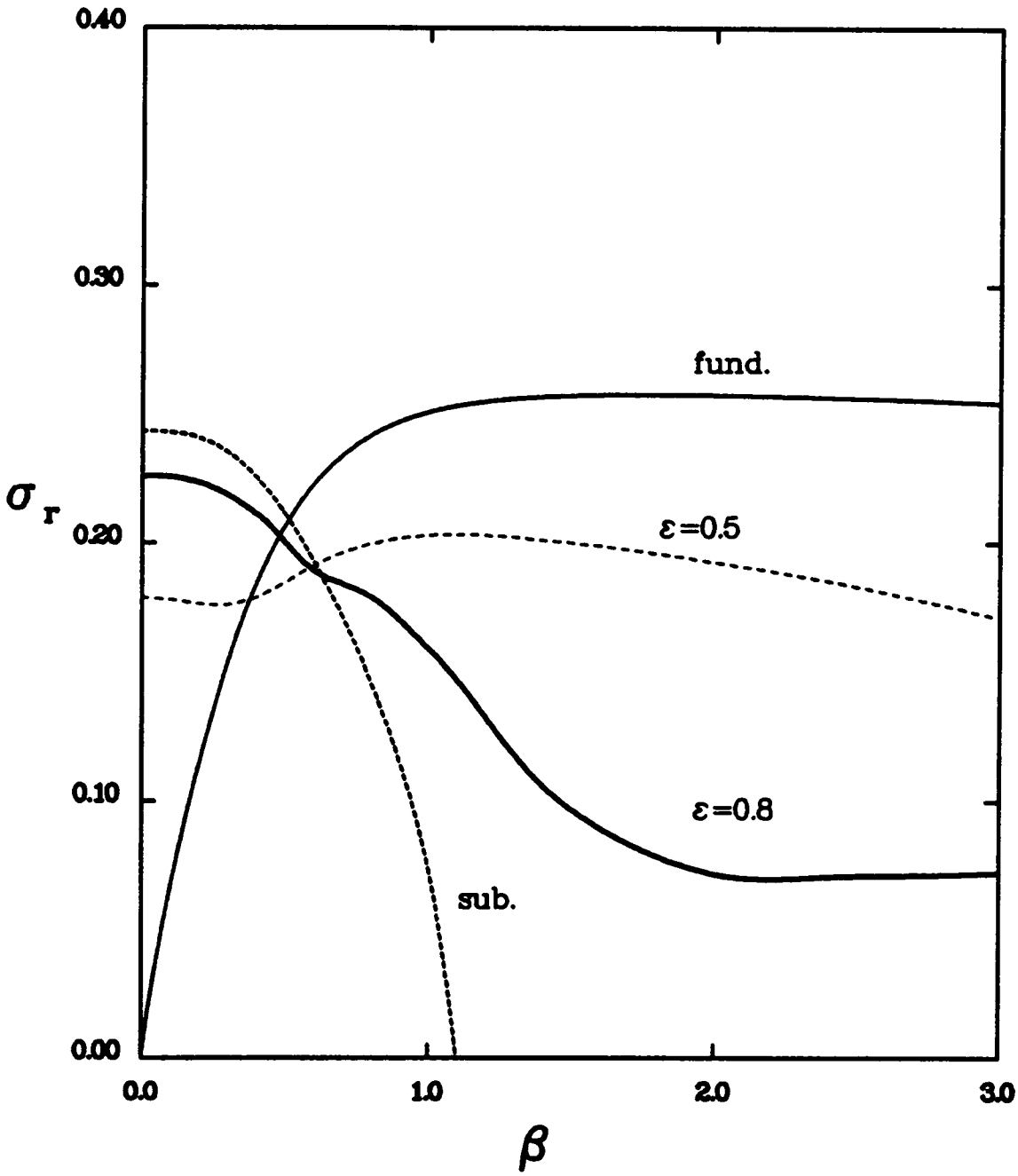

FIGURE 4.32 Growth rates of detuned modes as a function of the spanwise wavenumber for a TS amplitudes of A=0.091, α=1.0, R=5000, JJ=33, η =2.

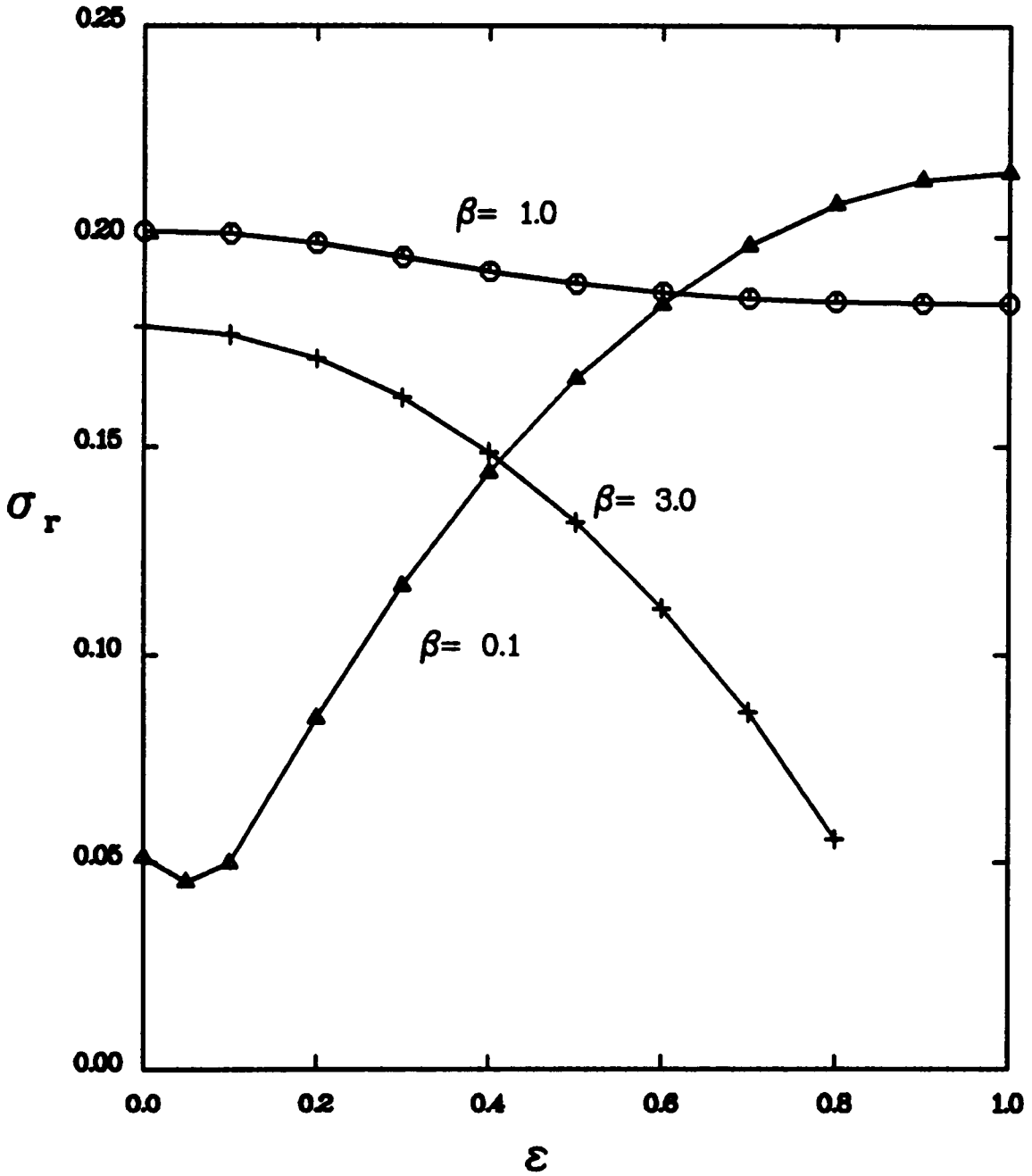

FIGURE 4.33 Variation of growth rates as a function of the detuning for various streamwise wavenumbers. A = 0.0355, R = 5000, α = 1.0.

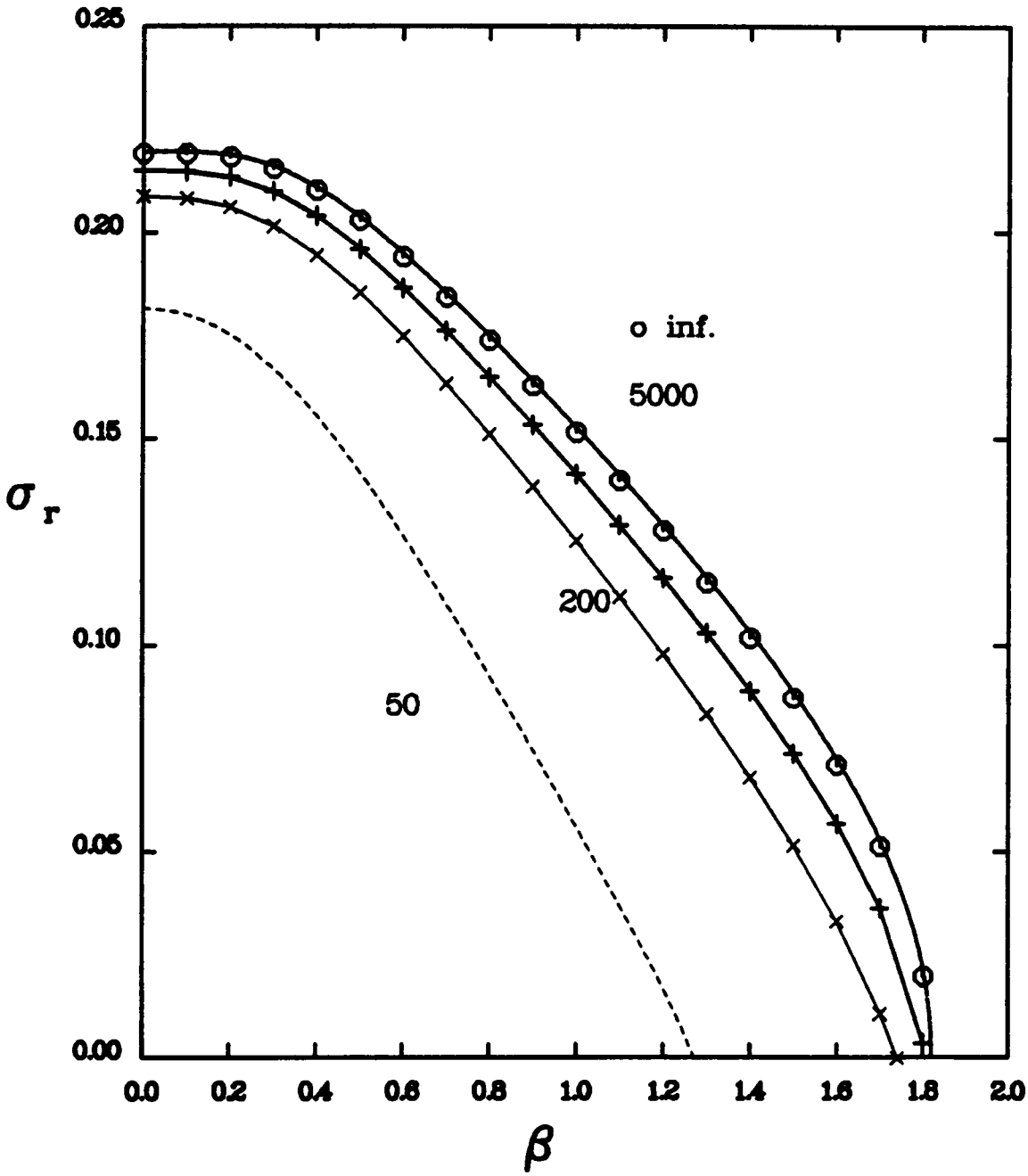

FIGURE 4.34 Growth rates of the subharmonic mode as a function of the spanwise wavenumber for various R. A=0.0355, α=1. R=inf (o), 5000 (–), 500(+), 200 (x), 50 (––)

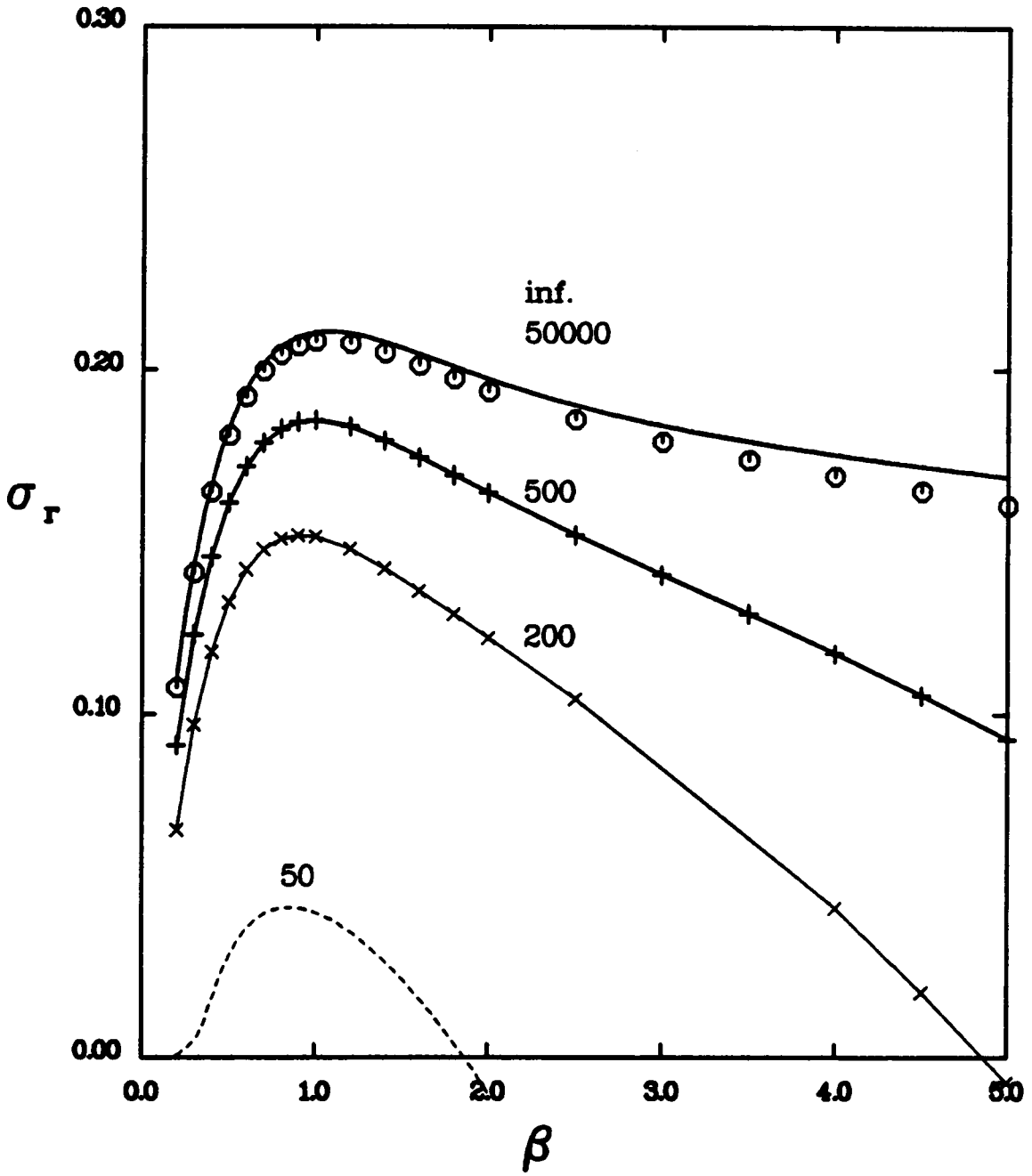

FIGURE 4.35 Growth rates of the fundamental mode as a function of the spanwise wavenumber for various R. A=0.0355, α=1. R=inf (o), 5000 (–), 500(+), 200 (x), 50 (––)

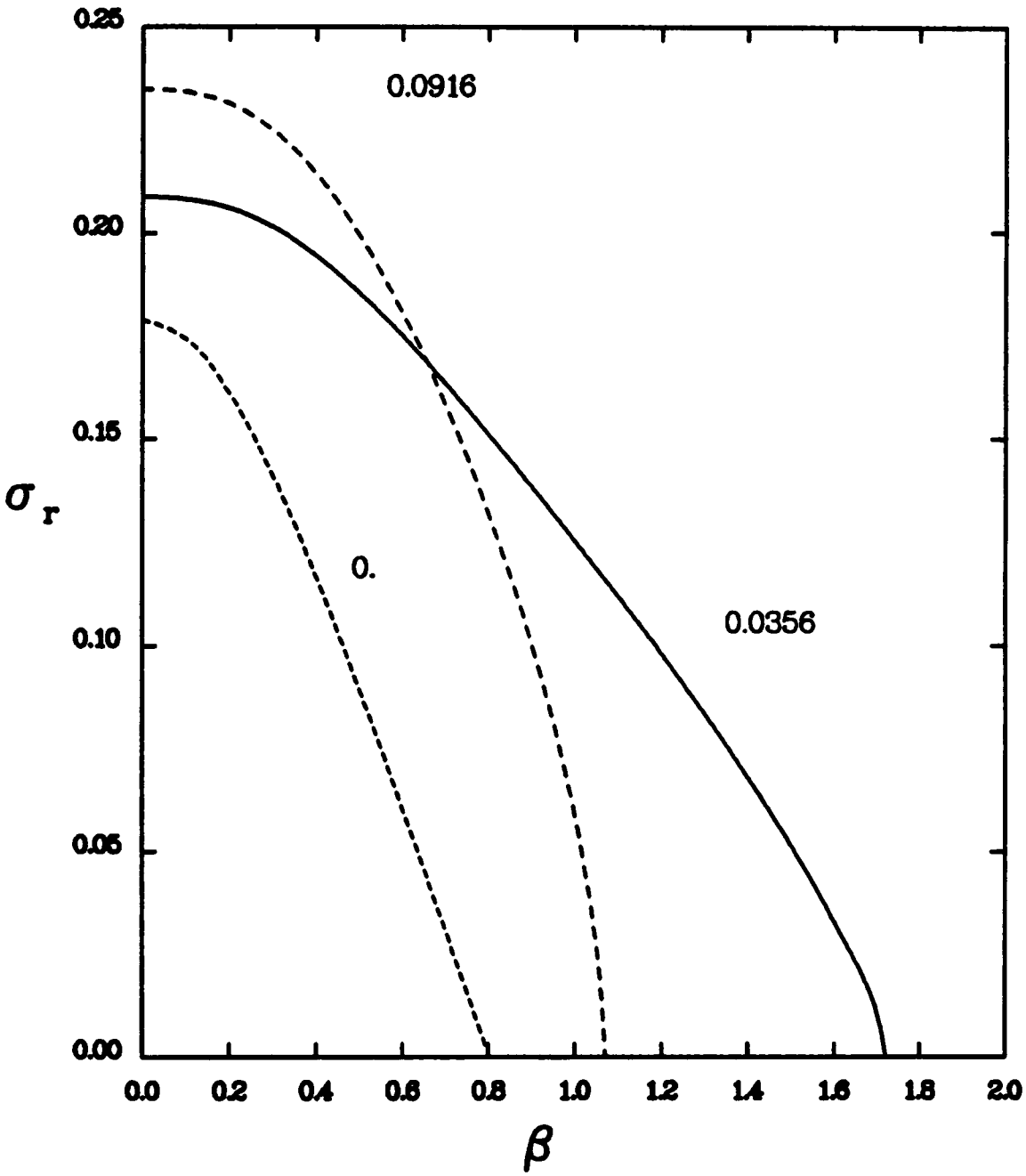

FIGURE 4.36 Growth rates of the subharmonic mode as a function of the spanwise wavenumber for various amplitudes of the TS. R=200, α=1

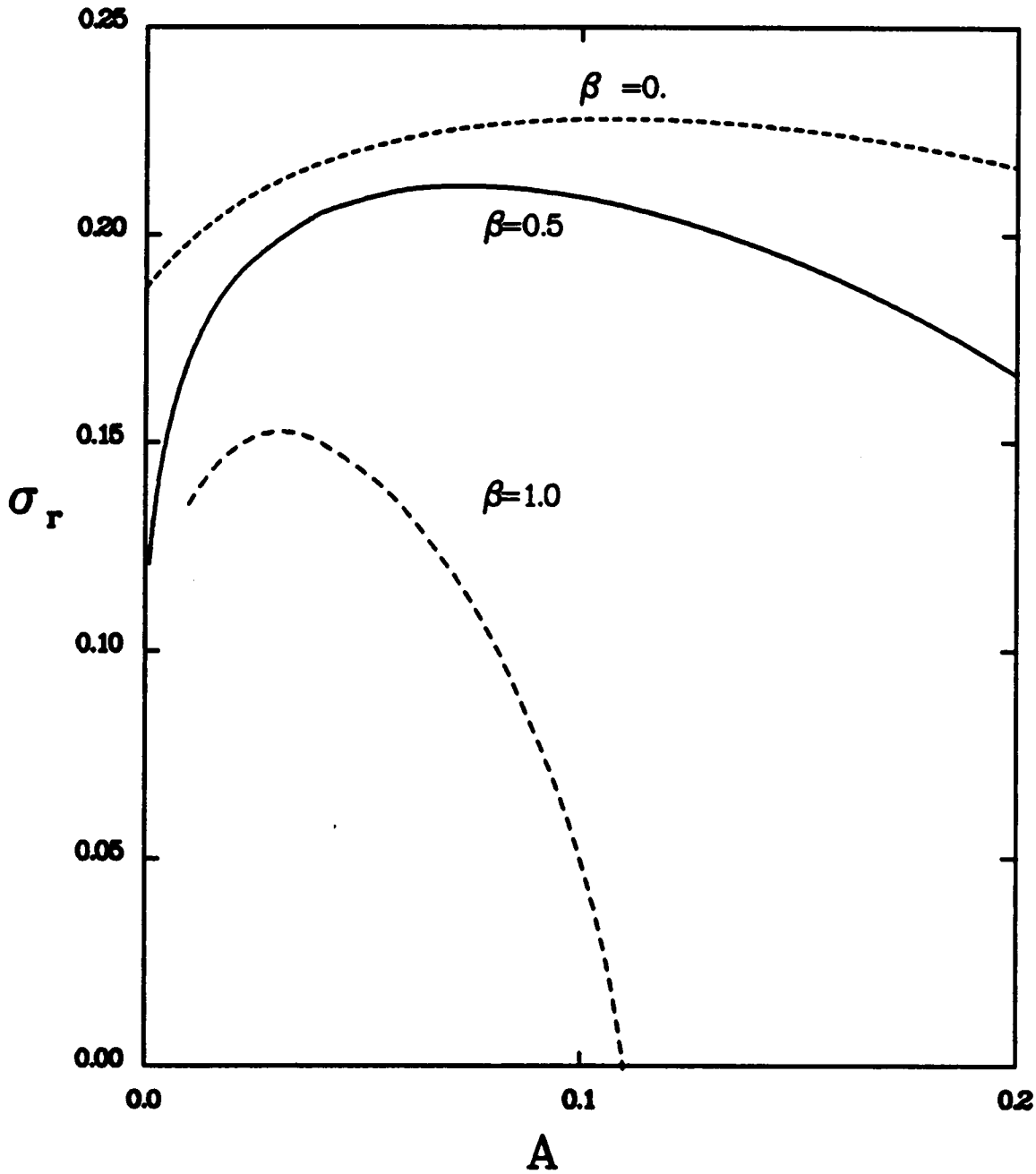

FIGURE 4.37 Variation of growth rates of the subharmonic with the TS amplitude for various spanwise wavenumbers. A = 0.0355, R = 5000, α = 1.0.

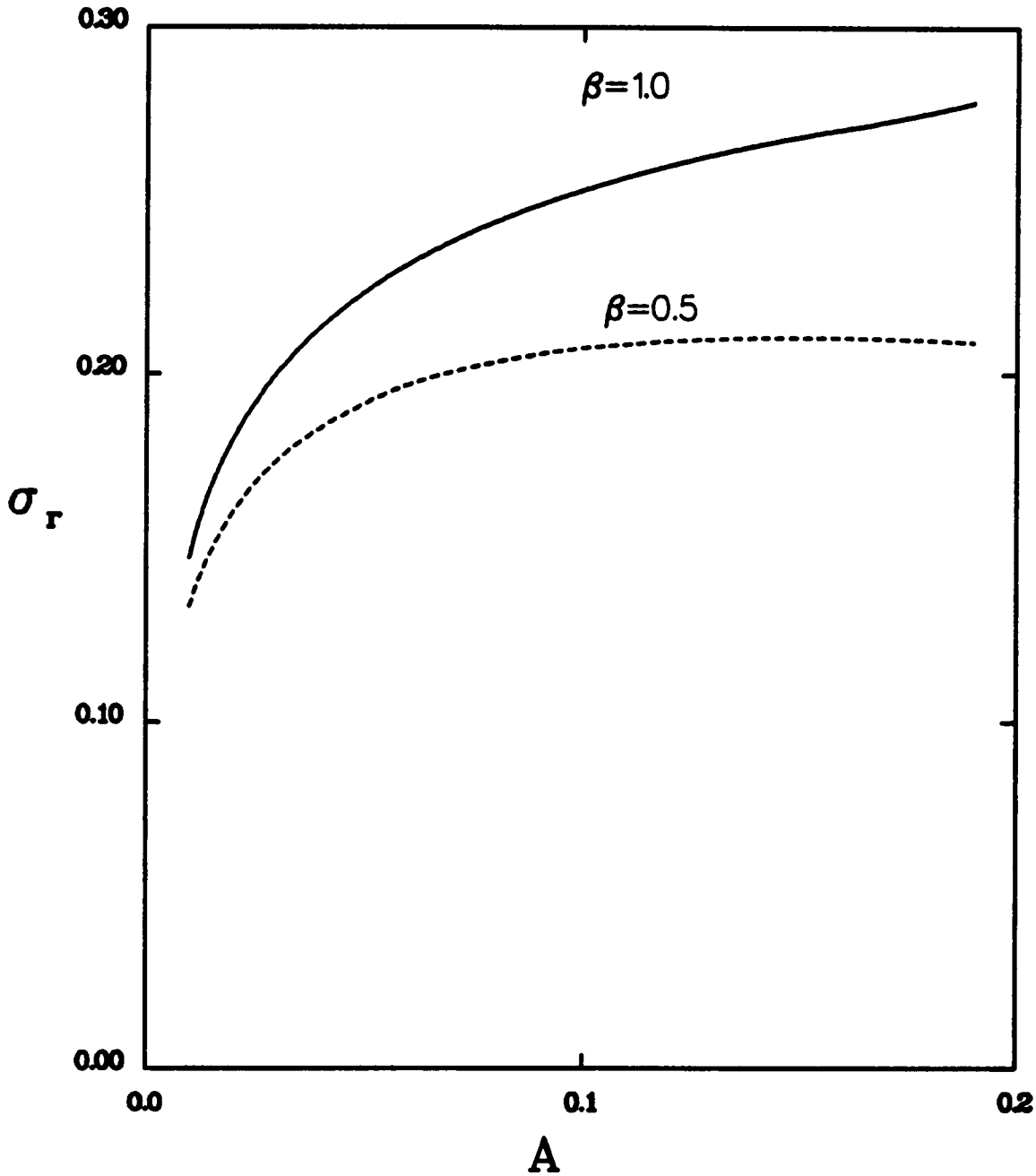

FIGURE 4.38 Variation of growth rates of the fundamental with the TS amplitude for various spanwise wavenumbers. A = 0.0355, R = 5000, α = 1.0.

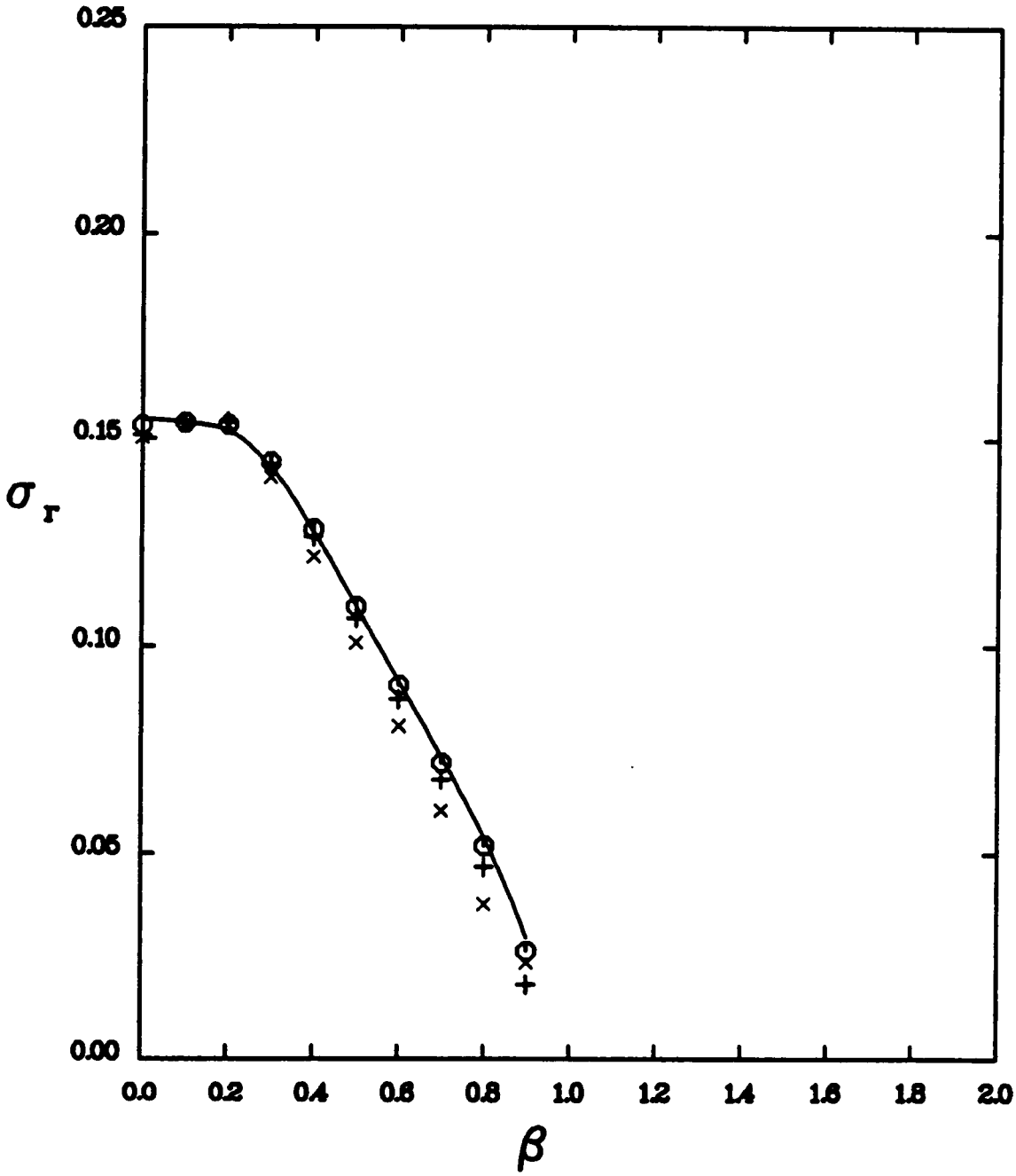

FIGURE 4.39 Growth rates of the subharmonic mode as a function of the spanwise wavenumber for various R. A=0.1777, α=.4 R=1600 (o), 800 (−), 400 (+), 200 (x).

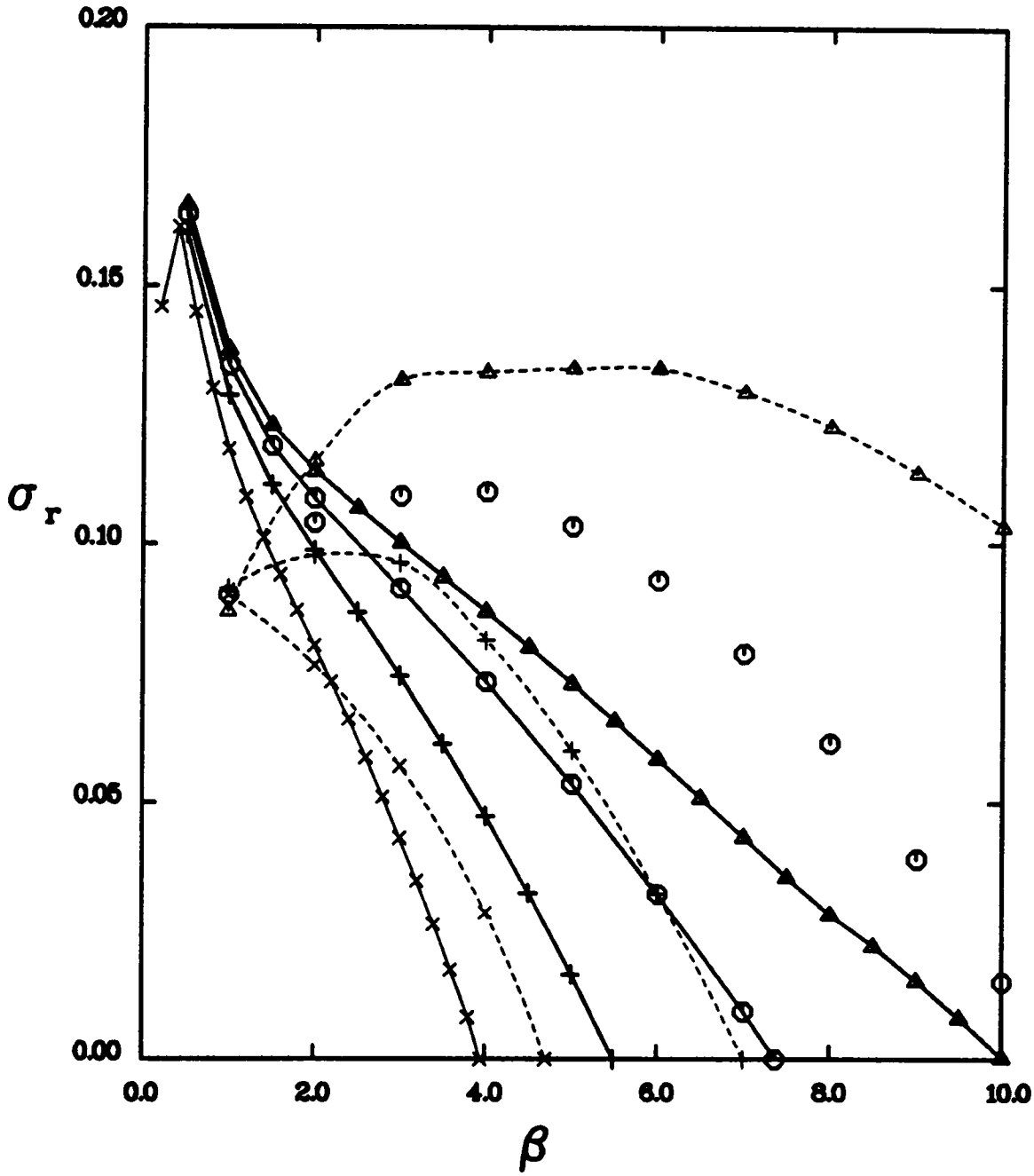

FIGURE 4.40 Growth rates of the fundamental mode as a function of the spanwise wavenumber. A=0.177, α=0.4, R=1600(~), 800(o), 400(+), 200(x). Theory (–), Metcalfe (––)

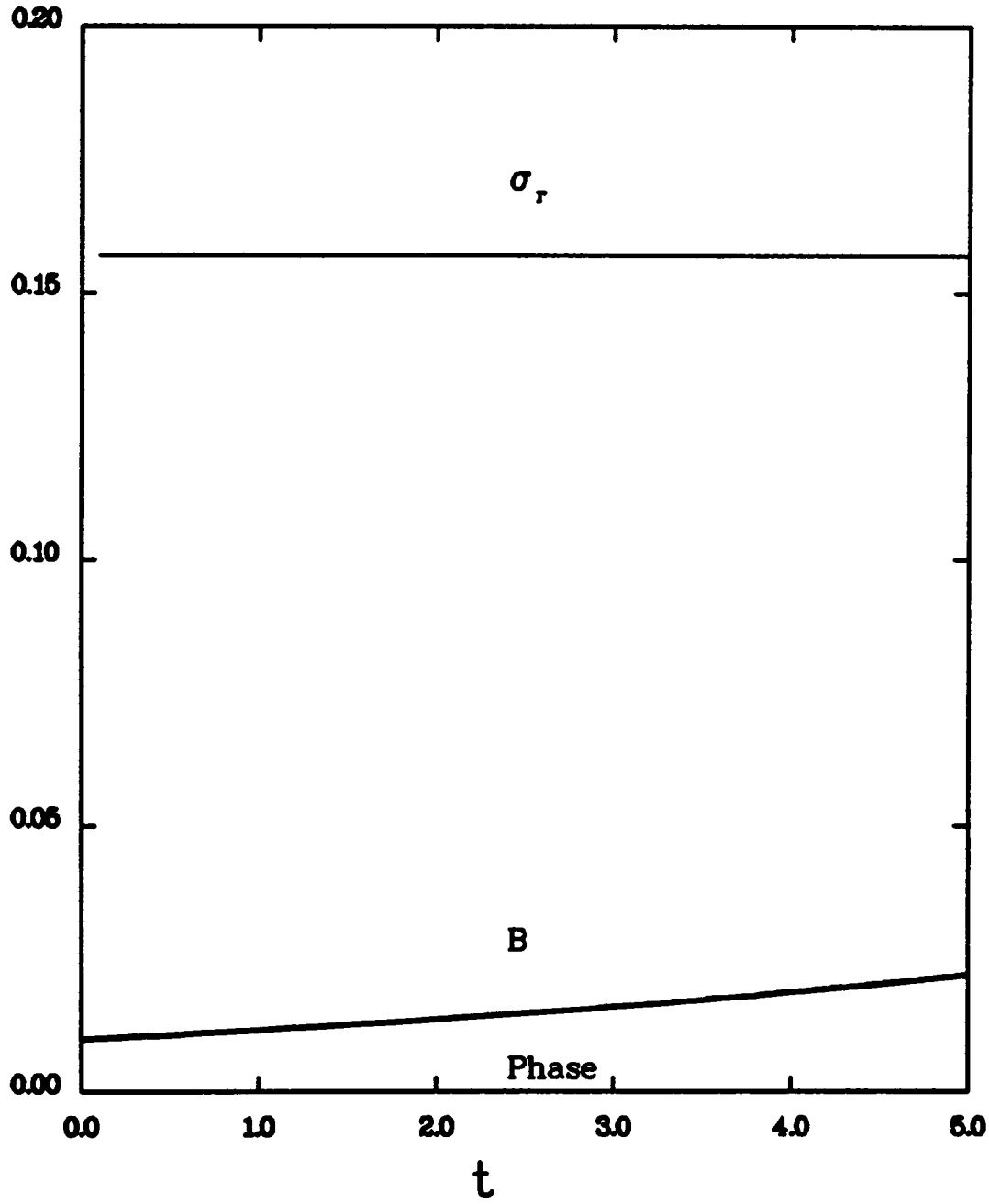

FIGURE 4.41 Temporal evolution of the subharmonic mode in presence of a constant amplitude TS wave.
A = 0.177, R = 1600, α = 0.4.

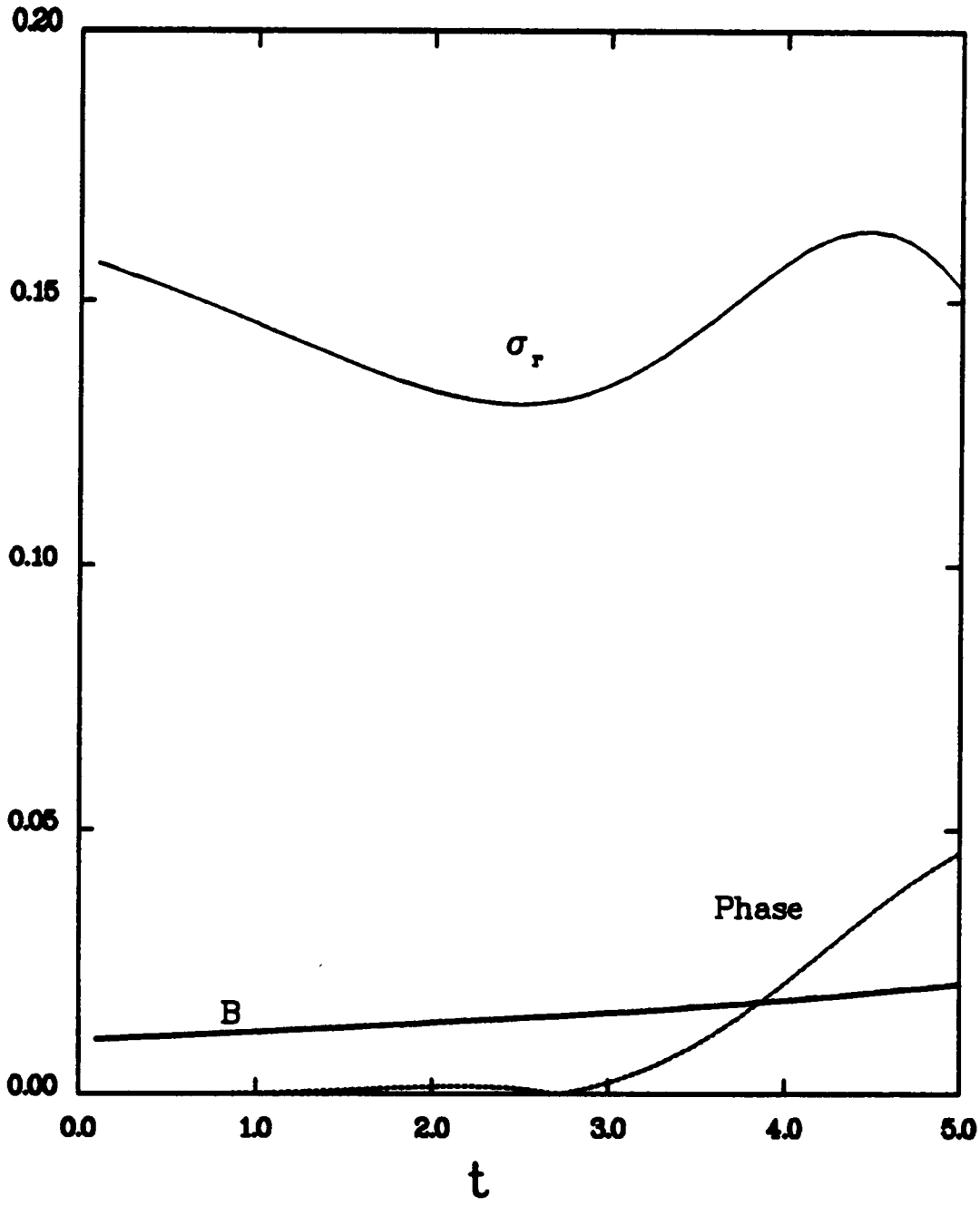

FIGURE 4.42 Temporal evolution of the subharmonic mode in presence of a growing TS wave.
A = 0.177, R = 1600, α = 0.4.

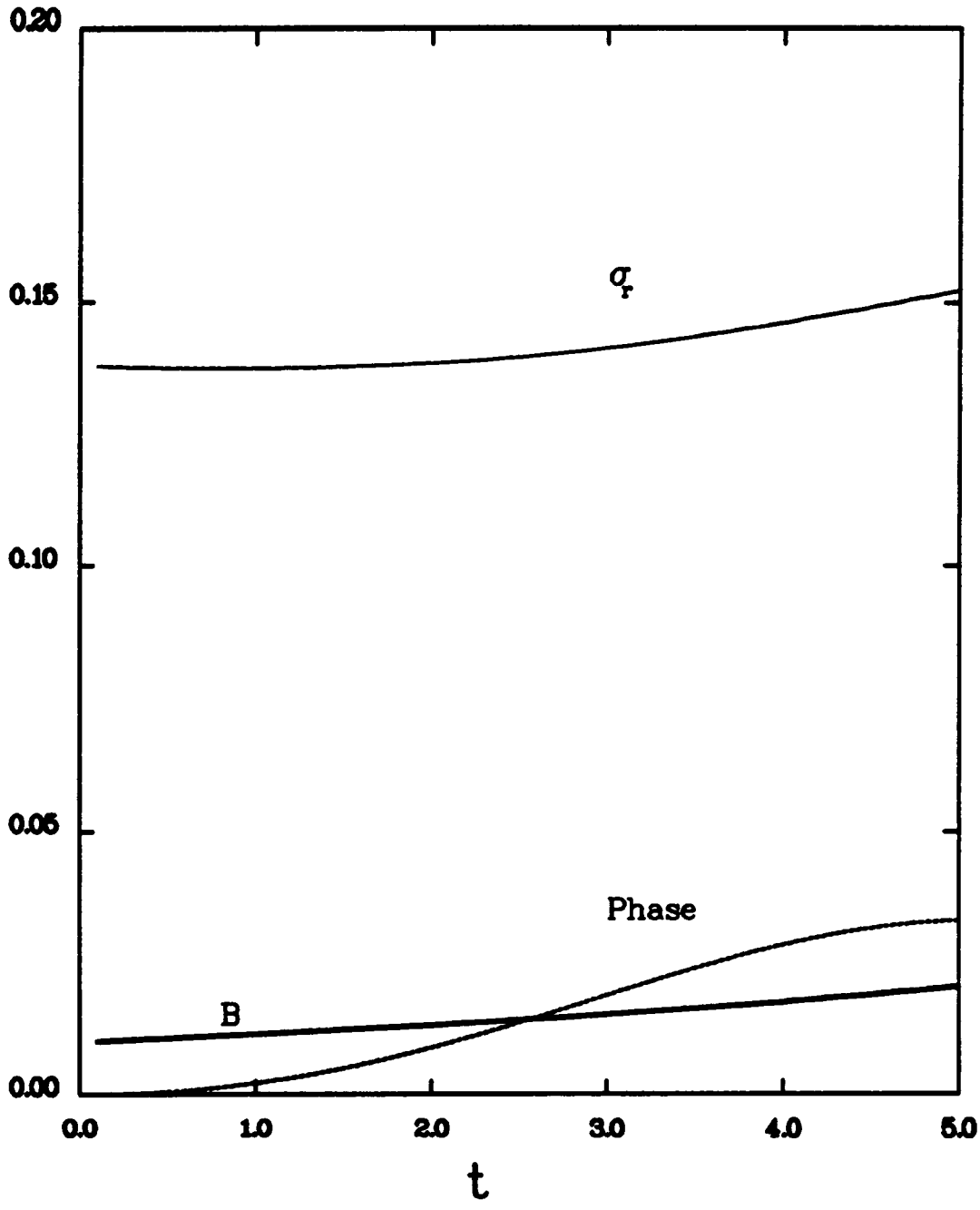

FIGURE 4.43 Temporal evolution of the fundamental mode in presence of a growing TS wave.
A = 0.177, R = 1600, α = 0.4, β = 1.0.

Table 3.1 Principal secondary instability eigenvalue.					
Detuning	Number of Fourier modes	20 collocation points		30 collocation points	
		$10^3\sigma_r$	$10^3\sigma_i$	$10^3\sigma_r$	$10^3\sigma_i$
$\epsilon = 0$	2	8.11571	0	8.11789	0
subharmonic	3	8.15454	0.07349	8.15701	0.01443
mode	4	8.19404	0	8.19611	0
	5	8.19433	0	8.19625	0
	6	8.19461	0	8.19639	0
	7	8.19461	0	8.19639	0
$\epsilon = 0.5$	2			6.18139	1.64569
detuned	3			6.40703	1.48160
mode	4			6.41874	1.47093
	5			6.42060	1.47088
	6			6.42048	1.47086
	7			6.42048	1.47087
$\epsilon = 1$	2	-1.07251	1.96292		
fundamental	3	3.63671	0	3.63993	0
mode	4	3.64732	0.01229	3.65078	0.01015
	5	3.65802	0	3.66205	0
	6	3.65840	0	3.66192	0
	7	3.65878	0	3.66179	0

Table 4.1 Eigenvalue c_i of the Orr-Sommerfeld equation for R=100. Solution using Chebyshev polynomials and hyperbolic mapping.

wavenumber	$\hat{y}_0$	17 points	33 points	65 points
$\alpha = 0.5$	0.5	0.1645878	0.2011900	0.2477387
	1.0	0.3233124	0.3327544	0.3373312
	2.0	0.3422089	0.3418226	0.3418226
	4.0	0.3175261	0.3418114	0.3418226
	6.0	0.1205250	0.3389183	0.3418226
	8.0	-0.0159951	0.3166555	0.3418086
$\alpha = 0.25$	0.5	0.1610743	0.2529422	0.3295110
	1.0	0.5258303	0.5516100	0.5675680
	2.0	0.5897691	0.5934961	0.5953940
	4.0	0.5983402	0.5972597	0.5972556
	6.0	0.5829078	0.5973822	0.5972557
	8.0	0.4296803	0.5979333	0.5972562
$\alpha = 0.75$	0.5	0.0487179	0.0727743	0.1009418
	1.0	0.1339182	0.1355239	0.1361849
	2.0	0.1366041	0.1365500	0.1365473
	4.0	0.0431687	0.1360816	0.1365470
	6.0	-0.0230763	0.1143409	0.1365441
	8.0	-0.0223925	0.0417186	0.1360335

Table 4.2 Eigenvalue c_i of the Orr-Sommerfeld equation for R=100. Solution using Chebyshev polynomials and algebraic mapping.

wavenumber	$\hat{y}_0$	17 points	33 points	65 points
$\alpha = 0.5$	0.5	0.3428199	0.3410579	0.3418684
	1.0	0.3406965	0.3418697	0.3418227
	2.0	0.3414613	0.3418228	0.3418226
	4.0	0.3187870	0.3418147	0.3418226
	6.0	0.1210583	0.3390406	0.3418226
	8.0	-0.0164775	0.3169086	0.3418095
$\alpha = 0.25$	0.5	0.7217661	0.6052207	0.5969097
	1.0	0.6056630	0.5969015	0.5972748
	2.0	0.5967672	0.5972751	0.5972557
	4.0	0.5979216	0.5972567	0.5972556
	6.0	0.5830908	0.5973797	0.5972556
	8.0	0.4279854	0.5979462	0.5972562
$\alpha = 0.75$	0.5	0.1334787	0.1368924	0.1365432
	1.0	0.1381376	0.1365433	0.1365469
	2.0	0.1367630	0.1365469	0.1365470
	4.0	0.4047953	0.1361466	0.1365470
	6.0	-0.0234859	0.1147149	0.1365445
	8.0	-0.2027577	0.0420740	0.1360489

Table 4.3 Eigenvalue c_i of the Orr-Sommerfeld equation for R=100. Solution using Fourier series and trigonometric mapping.

wavenumber	$\hat{y}_0$	17 points	33 points	65 points
$\alpha = 0.5$	0.5	0.3460102	0.3415437	0.3418168
	1.0	0.3414929	0.3418197	0.3418226
	2.0	0.3418402	0.3418227	0.3418226
	4.0	0.3176844	0.3418475	0.3418251
	6.0	0.1157120	0.3388544	0.3447559
	8.0	0.0164034	0.3165260	0.3309618
$\alpha = 0.25$	0.5	0.6158224	0.5991557	0.5971138
	1.0	0.5993364	0.5971291	0.5972533
	2.0	0.5971219	0.5972543	0.5972557
	4.0	0.5971919	0.5972405	0.5972535
	6.0	0.5822258	0.5979702	0.5966465
	8.0	0.4273223	0.5984909	0.6333201
$\alpha = 0.75$	0.5	0.1349300	0.1366115	0.1365446
	1.0	0.1367112	0.1365451	0.1365469
	2.0	0.1364017	0.1365469	0.1365469
	4.0	0.0401642	0.1360944	
	6.0	-0.0231420	0.1138914	
	8.0	0.0218664	0.0039997	

Table 4.4 Eigenvalue c_i of the Orr-Sommerfeld equation for R=100. Solution for $\alpha = 0.5$.

wavenumber	$\hat{y}_0$	17 points	33 points	65 points
Chebyshev	0.5	0.3402716	0.3418194	0.3418226
polynomials.	1.0	0.3438415	0.3418225	0.3418226
Trigonometric	2.0	0.3399443	0.3418224	0.3418226
mapping	4.0	0.0742622	0.3378922	0.3418225
	6.0	-0.0208460	0.2783279	0.3416449
	8.0	-0.0161837	0.0729221	0.3374306
Fourier	0.5	-0.1019317	-0.0449245	0.0045914
series.	1.0	0.1983538	0.2455489	0.2754669
Hyperbolic	2.0	0.3312388	0.3369637	0.3394371
mapping	4.0	0.3562554	0.3502770	0.3418228
	6.0	0.3391378	0.5124943	0.3389291
	8.0	0.2483799	0.5590763	0.3415078
Fourier	0.5	0.2188644	0.3139798	0.3430817
series.	1.0	0.3421586	0.3457980	0.3429781
algebraic	2.0	0.3432856	0.3418850	0.3418163
mapping	4.0	0.3413539	0.3418006	0.3418226
	6.0	0.3211390	0.3350988	0.3418262
	8.0	0.2424993	0.3333152	0.3369163

REFERENCES

1. Anders, J. B. and Blackwelder, R. F. 1980 "Longitudinal vortices in a transitioning boundary layer," in *Laminar-Turbulent Transition*, ed. R. Eppler and H. Fasel, pp. 110-119, Springer-Verlag.
2. Benney, D. J. and Lin, C. C. 1960 "On the secondary motion induced by oscillations in a shear flow," *Phys. Fluids*, vol. 3, pp. 656-657.
3. Bernal, L. P. and Roshko, A. 1986 "Streamwise vortex structure in plane mixing layers," *J. Fluid Mech.*, vol. 170, pp. 499-525.
4. Bertolotti, F. P. 1985 "Temporal and Spatial Growth of Subharmonic Disturbances in Falkner-Skan Flows," VPI & SU, M.S. thesis.
5. Bertolotti, F. P. and Herbert, Th. 1987 "A study on visualizations of boundary-layer transition," *Exp. Fluids.* In preparation.
6. Bertolotti, F. P., Santos, G. R., and Herbert, Th. 1986 "Early stages of boundary-layer transition - an animated theory," 16 mm movie, VPI & SU.
7. Blackwelder, R. F. 1979 "Boundary-layer transition," *Phys. Fluids*, vol. 22, pp. 583-584.
8. Breidenthal, R. 1981 "Structure in turbulent mixing layers and wakes using a chemical reaction," *J. Fluid Mech.*, vol. 109, pp. 1-24.
9. Browand, F. K. and Troutt, T. R. 1980 "A note on spanwise structure in the two-dimensional mixing layer," *J. Fluid Mech.*, vol. 97, pp. 771-81.
10. Cain, A. B., Reynolds, W. C. and Ferziger, J. H. 1981 "A three-dimensional simulation of transition and early turbulence in a time-developing mixing layer," Intern. Rep. No. TF-14, Stanford Univ., Calif..
11. Chandrsuda, C., Mehta, R. D., Weir, A.D., and Bradshaw, P. 1978 "Effect of free-stream turbulence on large structure in turbulent mixing layers," *J. Fluid Mech.*, vol. 85, pp. 693-704.
12. Canuto, C., Hussaini, M. Y., and Zang, T. A. 1987 *Spectral methods in Fluid Dynamics,* Springer-Verlag, Berlin.
13. Corcos, G. M. and Sherman, F. S. 1984 "The mixing layer: deterministic models of a turbulent flow. Part 1. Introduction and the two-

dimensional flow," *J. Fluid Mechanics*, vol. 139, pp. 29-65.

14. Corcos, G. M. and Lin, S. J. 1984 "The mixing layer: deterministic models of a turbulent flow. Part 2. the origin of the three-dimensional motion," *J. Fluid Mechanics.*

15. Corke, T. C. and Mangano, R. A. 1987 "Transition of a boundary layer: controlled fundamental-subharmonic interactions," in *Proc. IUTAM Symposium on Turbulence Management and Relaminarization*, ed. H. W. Liepmann and R. Narasimha, Bangalore, India. To appear.

16. Cornelius, K. C. 1985 "Three dimensional wave development during boundary layer transition," Lockheed Georgia Research Report LG85RR0004.

17. Craik, A. D. D. 1971 "Nonlinear resonant instability in boundary layers," *J. Fluid Mech.*, vol. 50, pp. 393-413.

18. Crighton, D. G. and Gaster, M. 1976 "Stability of slowly divergent jet flow," *J. Fluid Mech.*, vol. 77, pp. 397-413.

19. Crouch, J. D. and Herbert, Th. 1986 "Perturbation analysis of nonlinear secondary instability in boundary layers," *Bull. Am. Phys. Soc.*, vol. 31, p. 1718.

20. Drazin, P. and Reid, W. 1981 *Hydrodynamic Stability,* Cambridge University Press.

21. Feigenbaum, M. 1980 "The transition to aperiodic behavior in turbulent systems," *Commum. Math. Phys.*, vol. 77, p. 65.

22. Fielder, H. A., Dziomba, B., Mensing, P., and Rösgen, T. 1981 "Initiation, evolution and global consequences of coherent structures in turbulent shear flows," in *The Role of Coherent Structures in Modelling Turbulence and Mixing, Lecture Notes in Physics*, ed. J. Jimenez, vol. 136, pp. 219-251, Springer.

23. Freymuth, P. 1966 "On transition in a separated laminar boundary layer," *J. Fluid Mech.*, vol. 25, pp. 683-704.

24. Gaster, M. 1962 "A note on the relation between temporally-increasing and spatially-increasing disturbances in hydrodynamic stability," *J. Fluid Mech.*, vol. 14, pp. 222-224.

25. Gaster, M., Kit, E., and Wygnanski, I. 1985 "Large-scale structures in a forced turbulent mixing layer," *J. Fluid Mech.*, vol. 150, pp. 23-39.

26. Gottlieb, D. and Orszag, S. A. 1977 "Numerical analysis of spectral methods: theory and applications," CBMS-NSF Reg. Conf. Ser. in Appl. Math., SIAM.

27. Hama, F. R., Long, J. D., and Hegarty, J. C. 1957 "On transition from laminar to turbulent flow," *J. Appl. Phys.*, vol. 27, pp. 388-394, SIAM.

28. Herbert, Th. 1981 "A secondary instability mechanism in plane Poiseuille flow," *Bull. Amer. Phys. Soc.*, vol. 26, p. 1257.

29. Herbert, Th. 1981 "Numerical studies on nonlinear hydrodynamic stability by computer-extended perturbation series," in *Proc. 7th Int. Conf. Numer. Meth. Fluid Dyn., Stanford, California, 1980*, ed. W. C. Reynolds and R. W. MacCormack, Lecture Notes in Physics, vol. 141, pp. 200-205, Berlin-Heidelberg-New York: Springer-Verlag.

30. Herbert, Th. 1981 "Stability of plane Poiseuille flow - theory and experiment," VPI-E-81-35, Blacksburg, VA.

31. Herbert, Th. 1983 "Secondary instability of plane channel flow to subharmonic three-dimensional disturbances," *Phys. Fluids*, vol. 26, pp. 871-874.

32. Herbert, Th. 1983 "Subharmonic resonance in the Blasius boundary layer," *Bull. Amer. Phys. Soc.*, vol. 28, p. 1373.

33. Herbert, Th. 1984 "Analysis of the subharmonic route to transition in boundary layers," AIAA Paper No. 84-0009.

34. Herbert, Th. 1984 "Modes of secondary instability in plane Poiseuille flow," in *Turbulence and Chaotic Phenomena in Fluids*, ed. T. Tatsumi, pp. 53-58, North-Holland.

35. Herbert, Th. 1984 "On the Early Stages of K-Breakdown in the Blasius Boundary Layer," *Bull. Amer. Phys. Soc.*, vol. 29, p. 1540.

36. Herbert, Th. 1984 "Secondary Instability of Shear Flows," in *Special Course on Stability and Transition of Laminar Flow*, AGARD Report No. 709.

37. Herbert, Th. 1985 "Secondary instability of plane shear flows - theory and applications," in *Laminar-Turbulent Transition*, ed. V. V. Kozlov, pp. 9-20, Springer-Verlag.

38. Herbert, Th. 1985 "Three-dimensional phenomena in the transitional flat-plate boundary layer," AIAA Paper No. 85-0489.

39. Herbert, Th. 1986 "Vortical mechanisms in shear flow transition," in *Direct and Large Eddy Simulation of Turbulence*, ed. U. Schumann and R. Friedrich, pp. 19-36, Vieweg-Verlag.

40. Herbert, Th. 1987 "Analysis of secondary instabilities in boundary layers," in *Proc. 10th U. S. Nat. Cong. Appl. Mech., Austin, Texas*, ed. J. P. Lamb, pp. 445-456, ASME.

41. Herbert, Th. 1987 "On the mechanism of transition in boundary layers," AIAA Paper No. 87-1201.

42. Herbert, Th. and Bertolotti, F. P. 1985 "Effect of pressure gradients on the growth of subharmonic disturbances in boundary layers," in *Proc. Conf. on Low Reynolds Number Airfoil Aerodynamics*, ed. T. J. Mueller, Univ. of Notre Dame.

43. Herbert, Th. and Bertolotti, F. P. 1985 "The subharmonic route to transition - an animated theory," 16 mm Movie, Virginia Polytechnic Institute and State University.

44. Herbert, Th., Bertolotti, F. P., and Santos, G. R. 1985 "Floquet analysis of secondary instability in shear flows," in *Proc. ICASE/NASA Workshop on Stability of Time-Dependent and Spatially Varying Flows*, ed. D. L. Dwoyer and M. Y. Hussaini, pp. 43-57, Springer-Verlag.

45. Herbert, Th. and Morkovin, M. V. 1980 "Dialogue on bridging some gaps in stability and transition research," in *Laminar-Turbulent Transition*, ed. R. Eppler and H. Fasel, pp. 47-72, Springer-Verlag.

46. Hussaini, and A., Zang, T. 1987 "Spectral methods in fluid dynamics," *Ann. Rev. Fluid Mech.*, vol. 19, pp. 339-367.

47. Kachanov, Yu. S. and Levchenko, V. Ya. 1982 "Resonant interactions of disturbances in transition to turbulence in a boundary layer," Preprint No. 10-82, I.T.A.M., USSR Acad. Sci., Novosibirsk. (In Russian)

48. Kachanov, Yu. S. and Levchenko, V. Ya. 1984 "The resonant interaction of disturbances at laminar-turbulent transition in a boundary layer," *J. Fluid Mech.*, vol. 138, pp. 209-247.

49. Kelly, R. E. 1967 "On the stability of an inviscid shear layer which is periodic in space and time," *J. Fluid Mech.*, vol. 27, pp. 657-689.

50. Klebanoff, P. S. and Tidstrom, K. D. 1959 "Evaluation of amplified waves leading to transition in a boundary layer with zero pressure gradient," NASA TN D-195.

51. Klebanoff, P. S., Tidstrom, K. D., and Sargent, L. M. 1962 "The three-dimensional nature of boundary-layer instability," *J. Fluid Mech.*, vol. 12, pp. 1-34.

52. Kleiser, L. and Laurien, E. 1985 "Three-dimensional numerical simulation of laminar-turbulent transition and its control by periodic disturbances," in *Laminar-Turbulent Transition*, ed. V. V. Kozlov, pp. 29-37, Springer-Verlag, Berlin, Heidelberg.

53. Knapp, C. F. and Roache, P. J. 1968 "A combined visual and hot-wire anemometer investigation of boundary-layer transition," *AIAA J.*, vol. 6, pp. 29-36.

54. Lamb, L. 1932, *Hydrodynamics*, New York.

55. Lanczos, C. 1957, *Applied Analysis*, London.

56. Landahl, M. T. and Kaplan, R. E. 1965 "Effect of compliant walls on boundary layer stability and transition," AGARDograph 97-1-353.

57. Lasheras, J. C., Cho, J. S., and Maxworthy, T. 1986 "On the origin and evolution of streamwise vortical structures in a plane, free shear layer," *J. Fluid Mech.*, vol. 172, pp. 231-258.

58. Li, R. 1986 "Analysis for Taylor vortex flow," VPI & SU, PhD. thesis.

59. Lin, C. C. 1955 *The Theory of Hydrodynamic Instability*, Cambridge University Press, Cambridge.

60. Manneville, P. and Pomeau, Y. 1980 "Different ways to turbulence in dissipative dynamic systems," *Physica*, vol. D1, p. 167.

61. Metcalfe, R. W., Orszag, S. A., Brachet, M. E., Menon, S., and Riley, J. J. 1987 "Secondary instability of a temporarily growing mixing layer," *J.*

Fluid Mech..

62. Michalke, A. 1964 "On the inviscid instability of the hyperbolic tangent velocity profile," *J. Fluid Mech.*, vol. 19, pp. 543-556.

63. Michalke, A. 1965 "On spatially growing disturbances in an inviscid shear layer," *J. Fluid Mech.*, vol. 23, pp. 521-544.

64. Miksad, R. W. 1972 "Experiments on the non-linear stages of free shear layer transition," *J. Fluid Mech.*, vol. 56, pp. 695-719.

65. Monkewitz, P.A. and Huerre, P. 1982 "The influence of the velocity ratio on the spatial instability of mixing layers," *Phys. Fluids*, vol. 25, pp. 1137-1143.

66. Nayfeh, A. H. and Bozatli, A. N. 1979 "Secondary instability in boundary-layer flows," *Phys. Fluids*, vol. 22, pp. 805-813.

67. Nayfeh, A. H. 1985 "Three-dimensional spatial secondary instability in boundary-layer flows," AIAA Paper No. 85-1697.

68. Nayfeh, A. H. 1987 "Nonlinear stability of boundary layers," AIAA Paper No. 87-0044.

69. Orszag, S. A. and Patera, A. T. 1983 "Secondary instability of wall-bounded shear-flows," *J. Fluid Mech.*, vol. 128, pp. 347-385.

70. Pierrehumbert, R. T. and Widnall, S. E. 1982 "The two- and three-dimensional instabilities of a spatially periodic shear layer," *J. Fluid Mech.*, vol. 114, pp. 59-82.

71. Plaschko, P. 1979 "Helical instabilities of slowly divergent jets," *J. Fluid Mech.*, vol. 92, pp. 209-215.

72. Ragab, S. and Wu, J. L.. 1987 "Linear instability waves in supersonic turbulent mixing layers," AIAA paper 87-1418.

73. Ruelle, D. and Takens, F. 1971 "On the nature of turbulence," *Comm. Math. Phys.*, vol. 20. (see also Vol. 23, pp. 343-344)

74. Santos, G. R. and Herbert, Th. 1986 "Combination resonance in boundary layers," *Bull. Am. Phys. Soc.*, vol. 31, p. 1718.

75. Saric, W. S. and Reynolds, G. A. 1980 "Experiments on the stability of nonlinear waves in a boundary layer," in *Laminar-Turbulent Transition*, ed. R. Eppler & H. Fasel, pp. 125-134, Springer-Verlag.

76. Saric, W. S., Kozlov, V. V., and Levchenko, V. Ya. 1984 "Forced and unforced subharmonic resonance in boundary layer transition," AIAA Paper No. 84-0007.

77. Saric, W. S. and Thomas, A. S. W. 1984 "Experiments on the subharmonic route to turbulence in boundary layers," in *Turbulence and Chaotic Phenomena in Fluids*, ed. T. Tatsumi, pp. 117-122, North-Holland.

78. Sato, H. 1956 "Experimental investigation on the transition of laminar separated layer," *J. Phys. Soc. Jpn.*, vol. 11, pp. 702-709.

79. Sato, H. 1960 "The stability and transition of a two-dimensional jet," *J. Fluid Mech.*, vol. 7, pp. 53-80.

80. Schlichting, H. 1933 "Zur Entstehung der Turbulenz bei der Plattenströmung," *Nachr. Ges. Wiss. Göttingen*, Math.-Phys. Kl., pp. 181-208.

81. Schubauer, G. B. and Skramstad, H. K. 1948 "Laminar boundary-layer oscillations and transition on a flat plate," N.A.C.A. Rep. No. 909.

82. Spalart, P. R. 1986 "Numerical simulation of boundary layers: Part 1. Weak formulation and numerical method," NASA Technical Memorandum 88222, pp. 1-18.

83. Spalart, P. R. and Yang, K. S. 1986 "Numerical simulation of boundary layers: Part 2. Ribbon-induced transition in Blasius flow," NASA Technical Memorandum 88221, pp. 1-24.

84. Stuart, J. T. 1960 "Nonlinear effects in hydrodynamic stability," in *Proc. 10th Int. Cong. Appl. Mech., Stresa, Italy*, ed. F. Rolla and W. T. Koiter, pp. 63-67, Elsevier, Amsterdam.

85. Stuart, J. T. 1965 "The production of intense shear layers by vortex stretching and convection," AGARD Report 514.

86. Stuart, J.T. 1967 "On finite amplitude oscillations in laminar mixing layers," *J. Fluid Mech.*, vol. 29, pp. 417-440.

87. Thomas, A. S. W. and Saric, W. S. 1981 "Harmonic and subharmonic waves during boundary-layer transition," *Bull. Amer. Phys. Soc.*, vol. 26, p. 1252.

88. Tollmien, W. 1929 "Über die Entstehung der Turbulenz," *Nachr. Ges. Wiss. Göttingen*, Math.-Phys. Kl., pp. 21-44.

89. Winant, C. D. and Browand, F. K. 1974 "Vortex pairing, the mechanism of turbulent mixing layer growth at moderate Reynolds number," *J. Fluid Mech.*, vol. 63, pp. 442-447.

90. Wortmann, F. X. 1977 "The incompressible fluid motion downstream of two-dimensional Tollmien-Schlichting waves," in *Laminar-Turbulent Transition*, vol. 63, pp. 12/1-8, AGARD CP-224.

The vita has been removed from the scanned document